ALMA MATER STUDIORUM - UNIVERSITA' DI BOLOGNA

SECONDA FACOLTA' DI INGEGNERIA
CON SEDE A CESENA

CORSO DI LAUREA MAGISTRALE
IN INGEGNERIA AEROSPAZIALE

Sede di Forlì

ELABORATO FINALE DI LAUREA

In

Aerodinamica Applicata LM

Numerical and experimental investigation of turbulent dissipation

CANDIDATO

Bucciotti Andrea

RELATORE

Prof. Talamelli Alessandro

CORRELATRICE

Prof. Elisabetta De Angelis

Anno Accademico 2012/2013

Sessione III

Contents

Sommario

La dissipazione dell'energia turbolenta viene presentata nel contesto teorico della famosa teoria di Kolmogorov, formulata nel 1941. Alcune precisazioni e commenti sulla teoria aiutano il lettore nella comprensione dell'approccio allo studio della turbolenza, oltre a presentare alcune problematiche di base.

Viene fatta una chiara distinzione fra dissipazione, pseudo-dissipazione e surrogati della dissipazione. La dissipazione regola come l'energia cinetica turbolenta viene trasformata in energia interna, il che fa di questa quantità una caratteristica fondamentale da investigare per migliorare la nostra comprensione della turbolenza.

La dissertazione si concentra sull'investigazione sperimentale della pseudo-dissipazione. Difatti questa quantità è difficile da misurare dato che richiede la conoscenza completa del gradiente del campo di velocità tridimensionale. Avendo a che fare con anemometria a filo caldo per misurare la dissipazione è necessario considerare i surrogati, dato che risulta impossibile ottenere tutti i termini della pseudo-dissipazione. L'analisi dei surrogati è la parte principale di questo lavoro. In particolare due flussi, il canale ed il getto turbolenti, sono considerati. Questi flussi canonici, brevemente introdotti, sono spesso utilizzati come banco di prova per solutori numerici e strumentazioni sperimentali per la loro semplice struttura. Le osservazioni fatte in tali flussi sono spesso trasferibili a casi più complicati ed interessanti, con numerose applicazioni industriali.

Gli strumenti principali per l'investigazione sono DNS e misure sperimentali. I dati numerici sono utilizzati come riscontro per i risultati sperimentali, dato che tutte le componenti della dissipazione sono calcolabili nell'ambito della simulazione numerica. I risultati di alcune simulazioni numeriche erano già disponibile all'inizio di questa tesi, quindi il lavoro principale è stato incentrato sulla lettura ed elaborazione di questi dati. Gli esperimenti sono stati effettuati con la tecnica dell'anemometria a filo caldo, descritta nel dettaglio sia a livello teorico che pratico.

Lo studio della DNS del canale turbolento a Re=298 rivela che il surrogato tradizionale può essere migliorato. Di conseguenza due nuovi surrogati vengono proposti, basati su termini del gradiente di velocità facilmente accessibili dal punto di vista sperimentale. Riusciamo a trovare una formulazione che migliora l'accuratezza del surrogato di un ordine di grandezza.

Per il getto I risultati di una DNS a Re=1600, e i risultati del nostro apparato sperimentale a Re=70000 sono comparati per validare l'esperimento. Viene riscontrato che il rapporto fra i componenti della dissipazione considerati è diverso tra DNS ed esperimenti. Possibili errori in entrambi i set di dati vengono discussi, e vengono proposte delle soluzioni per migliorare i dati.

Abstract

Turbulent energy dissipation is presented in the theoretical context of the famous Kolmogorov theory, formulated in 1941. Some remarks and comments about this theory help the reader understand the approach to turbulence study, as well as give some basic insights to the problem.

A clear distinction is made amongst dissipation, pseudo-dissipation and dissipation surrogates. Dissipation regulates how turbulent kinetic energy in a flow gets transformed into internal energy, which makes this quantity a fundamental characteristic to investigate in order to enhance our understanding of turbulence.

The dissertation focuses on experimental investigation of the pseudo-dissipation. Indeed this quantity is difficult to measure as it requires the knowledge of all the possible derivatives of the three dimensional velocity field. Once considering an hot-wire technique to measure dissipation we need to deal with surrogates of dissipation, since not all the terms can be measured. The analysis of surrogates is the main topic of this work. In particular two flows, the turbulent channel and the turbulent jet, are considered. These canonic flows, introduced in a brief fashion, are often used as a benchmark for CFD solvers and experimental equipment due to their simple structure. Observations made in the canonic flows are often transferable to more complicated and interesting cases, with many industrial applications.

The main tools of investigation are DNS simulations and experimental measures. DNS data are used as a benchmark for the experimental results since all the components of dissipation are known within the numerical simulation. The results of some DNS were already available at the start of this thesis, so the main work consisted in reading and processing the data. Experiments were carried out by means of hot-wire anemometry, described in detail on a theoretical and practical level.

The study of DNS data of a turbulent channel at Re=298 reveals that the traditional surrogate can be improved Consequently two new surrogates are proposed and analysed, based on terms of the velocity gradient that are easy to measure experimentally. We manage to find a formulation that improves the accuracy of surrogates by an order of magnitude.

For the jet flow results from a DNS at Re=1600 of a temporal jet, and results from our experimental facility CAT at Re=70000, are compared to validate the experiment. It is found that the ratio between components of the dissipation differs between DNS and experimental data. Possible errors in both sets of data are discussed, and some ways to improve the data are proposed.

Introduction

Amongst the fields of classical physics, fluid mechanics is widely regarded as one of the most challenging and fascinating. Fluid mechanics is involved in a variety of natural phenomena or practical applications, ranging from weather forecast to the design of a race car. Every time a fluid moves, it does so by following the fundamental laws of physics (mass, momentum and energy conservation) written under the assumption of the fluid being a continuum made of infinite particles. Unfortunately the model that describes this motion, known as the Navier-Stokes equations, is rather difficult to solve analytically, aside from very simple (but important) cases.

To further increase the complexity of the problem, experiments show that flows can be divided in two categories. *Laminar flows* where the motion appears to be organized in a steady and regular fashion, and *Turbulent flows* where the motion is unsteady and seemingly random, so chaotic that any prediction on it's evolution may seem impossible. The discriminating parameter between this two regimes is the Reynolds number $\Re e \equiv U L / \nu$, which links the fluid viscosity ν to the characteristic length L and velocity U. Transition of the flow from laminar to turbulent state is a gradual process that arises for infinitesimal disturbances which get amplified and form instabilities.

The vast majority of flows encountered in nature or in practical applications are turbulent. Unlike other complicated phenomena turbulence is easily observed, but is extremely difficult to understand and explain. Due to our lack of a full comprehension of how turbulence works, research has focused on simple basic flows (like jets, channels, wakes or boundary layers) with the aim of enhancing the understanding of turbulent mechanisms.

Three main approaches have historically been followed:

• Analytical. The equations of motion are solved in an exact or approximate way, giving a mathematical description of the flow field. This approach is usually the best since it gives complete informations regarding all the quantities involved, but is seldom feasible since the equations can rarely be solved in a closed form. Also, while there are many solutions to the equations for laminar flows, this is not true in the case of turbulent flows, where even very simple cases are not solved.

• Numerical. The equations of motion are solved by means of computer. While in laminar flows the numerical solutions may be very accurate, in the turbulent regime a complete description of the flow is related to the description of the dynamics of all the turbulent scales (from the smallest

to the biggest), forcing the discretization of the flow domain to become finer and finer, saturating consequently the available computational resources. This restricts the application of numerical solutions of the Navier-Stokes equations only to low Reynolds number flows which today are still far from most industrial cases.

• Experimental. The flow is reproduced in laboratory and physical quantities are measured. With this approach it is possible to obtain results which are affected by measurement errors and by a lack of knowledge of the exact boundary conditions. On the other hand, measurements of real flows do not need almost any modelling and the errors are anyway bounded by the measurement uncertainties.

Using these tools it is possible to observe that high Reynolds number turbulence is characterised by the presence of a wide range of different coherent patterns, regarded as eddies. Large eddies are generated by the interaction between the flow and the solid surfaces inside it, and as a result turbulent kinetic energy is introduced in the flow. These big eddies are dependent on the particular flow geometry and are dominated by inertial forces. From the large eddies, energy is transferred to smaller ones in a process that is known as energy cascade; this happens until eddies reach their minimum dimension where dissipation of the turbulent kinetic energy into heat is caused by viscous forces. These small structures are called Kolmogorov scale, from the name of the mathematician that first quantified them in 1941. Unlike large scale eddies, they are believed to be independent on the flow geometry and have universal and isotropic properties.

The *turbulent kinetic energy dissipation* that takes place at Kolmogorov scales is a non reversible process, and a fundamental property of turbulence. It's determination requires the knowledge of the velocity gradient in each point of the flow field, which was impossible until in 1987. During that year Balint presented the first measurements of a velocity gradient in a boundary layer taken with a 9 sensor hot-wire probe, and Kim published the first DNS of a turbulent channel flow.

However the measurement of such quantity poses a significant challenge even today, given that some terms of the velocity gradients are of difficult experimental access. Because of this, surrogates for the dissipation have been proposed which involve only the terms easy to measure with the most common technique, i. e. hot-wire anemometry. Note that when dealing with experimental measurements one has to consider the filtering effects both in spatial and temporal resolution. These effects, generated by the inability of measuring a punctual quantity with a finite size sensor, can affect the results in a way such that real, physical phenomena will be overlooked or

on the contrary, artificially created.

The goal of the present thesis is to compare existing surrogates to the real dissipation, develop new ones, and discuss discrepancies due to the different formulations as well as the effects of filtering. In order to do so, the dissipation is evaluated with a numerical approach in a turbulent channel flow, and compared to the most common surrogates also from the same simulation. To further advance the study a numerical simulation of a turbulent jet is also considered, and the data compared to some experimental results.

Chapter 1 of this thesis is a collection of background theory in the fields of homogeneous isotropic turbulence (1.1), turbulent kinetic energy dissipation (1.2) and canonic flows involved in the study (1.3 and 1.4). Since we make large use of experimental data produced with hot-wire anemometry, the technique itself is presented (1.5) and some issues regarding filtering of the data are discussed (1.6).

Chapter 2 is a description of the experimental equipment utilised in the measurements (2.1), as well as the description of the set-up for the DNS in the temporal jet (2.2) and in the channel (2.3).

Chapter 3 presents the results obtained in the DNS of the channel flow (3.1), the experimental results in the physical jet (3.2) and the DNS data of the temporal jet (3.3). Given that we have two sets of data for the jet flow, a comparison between the two is made (3.4).

Chapter 4 is a recap of the work done and of the results obtained, with additional comments on possible ways to improve the data sets. Questions left open are also reported in this section, with the hope that further studies can continue this research.

1. Theory

1.1 The Kolmogorov 1941 theory

The Kolmogorov 1941 theory is based on a set of three hypothesis applied to the Navier - Stokes equations. Based on these hypothesis it's possible to derive some relations and make predictions about the behaviour of a turbulent flow.

HP1 In the limit of very large Reynolds number, all the possible symmetries of the N-S equations broken by the insurgence of turbulence, are restored in a statistical sense at small scales and away from boundaries.

So, if l_0 is the integral scale for the production of turbulence considered, a "small scale" is $l \ll l_0$. Defining the velocity increments as:

$$\delta \boldsymbol{u}(\boldsymbol{r},\boldsymbol{l}) \equiv \boldsymbol{u}(\boldsymbol{r}+\boldsymbol{l}) - \boldsymbol{u}(\boldsymbol{l}) \tag{1.1.1}$$

we assume that these velocity increments are homogeneous in the domain for all displacements **ρ** and small increments $\boldsymbol{l}$:

$$\delta \boldsymbol{u}(\boldsymbol{r}+\rho,\boldsymbol{l}) \overset{law}{=} \delta \boldsymbol{u}(\boldsymbol{r},\boldsymbol{l}) \tag{1.1.2}$$

HP2 Under the same assumptions of HP1, turbulent flow is self similar at small scales, with a unique scaling exponent $h \in \mathbb{R}$ such that:

$$\delta \boldsymbol{u}(\boldsymbol{r},\lambda \boldsymbol{l}) \overset{law}{=} \lambda^h \delta \boldsymbol{u}(\boldsymbol{r},\boldsymbol{l}), \quad \forall \lambda \in \mathbb{R}^+ \tag{1.1.3}$$

HP3 Under the same assumptions of HP1, turbulent flow has a finite non vanishing mean rate of dissipation ε per unit mass.

Under the hypothesis of homogeneity, isotropy and **HP3** it's possible to write an exact and non trivial relation for the third order longitudinal structure function for the velocity increment:

$$S_3(\boldsymbol{l}) = \langle (\delta \boldsymbol{u}_{||}(\boldsymbol{r},\boldsymbol{l}))^3 \rangle = -\frac{4}{5}\varepsilon l \ , \tag{1.1.4}$$

where $\boldsymbol{u}_{||}(\boldsymbol{r},\boldsymbol{l})$ stands for the velocity increment (as in 1.1.1) in the longitudinal direction $\boldsymbol{l}$.

This is the four – fifths law that Kolmogorov derived from the N-S equations. A proof of the law is given in details in the appendix, while here we focus on the main consequences of the theory.

One remark that can be done about this law is that it's invariant under Galilean transformations. We know that in absence of boundaries and forcing the N-S equations are invariant, so for any solution **u**(t, **r**) and for any vector **U**, **u'**(t, **r**) is still a solution. Isotropy is not conserved because **U** introduces a preferred direction, but homogeneity and stationarity are preserved. If **U** is taken random and isotropically distributed, all the structure functions (including S_3) are invariant.

The presence of a driving force breaks the invariances of the N-S equations but doesn't affect the four fifths law, which is then invariant under Galilean transformations.

Note that dropping the assumption of isotropy , for $\nu \to 0$ and small $\boldsymbol{l}$ it's still possible to derive a relation between velocity changes and dissipation rate:

$$-\frac{1}{4}\nabla_{\boldsymbol{l}} \cdot \langle |\delta \boldsymbol{u}(\boldsymbol{l})|^2 \delta \boldsymbol{u}(\boldsymbol{l}) \rangle = \varepsilon \tag{1.1.5}$$

This equation is equivalent to (1.1.4) when the flow is homogeneous and isotropic at all scales.

The exponent h = 1/3 of **HP2** can be directly inferred from (1.1.4).

Assuming that all the moments of arbitrary positive order p > 0 are finite, and defining the (longitudinal) structure function of order p as:

$$S_p(l) \equiv \langle (\delta \boldsymbol{u}_{||}(\boldsymbol{l}))^p \rangle \tag{1.1.6}$$

we can infer from the self – similarity hypothesis **HP2** and from h=1/3:

$$S_p(l) = C_p \varepsilon^{p/3} l^{p/3} \tag{1.1.7}$$

where the C_p are dimensionless and independent of Re (since $\mathrm{Re} \to \infty$). $C_3 = -4/5$ is clearly universal from (4/5 law), but nothing requires the other C_p to be so, as is instead postulated by Kolmogorov.

Note that $S_p(l)$ doesn't involve the integral scale since $l_0 \to \infty$. For finite integral scales there is a non dimensional correction function $\tilde{S}_p(l/l_0)$ to ensure an explicit dependence from the integral scale.

Moreover, the fact that the second order structure function follows an $l^{2/3}$ law implies that the dissipation rate also goes as $\varepsilon^{2/3}$. From probability theory we know that the energy spectrum is a power law

$$E(k) \approx k^{-n}, \quad 1 < n < 3 \quad , \tag{1.1.8}$$

and the second order spatial structure function is also a power law

$$\langle |\boldsymbol{u}(\boldsymbol{r}') - \boldsymbol{u}(\boldsymbol{r})|^2 \rangle \approx |\boldsymbol{r}' - \boldsymbol{r}|^{n-1} \quad , \tag{1.1.9}$$

meaning that the energy spectrum is

$$E(k) \approx \varepsilon^{2/3} k^{-5/3} \quad . \tag{1.1.10}$$

The dissipation range

In the derivation of the four – fifths law (see appendix) we assumed

$$K \gg K_c \approx l_0^{-1} \quad \text{And} \quad |2\nu\Omega_K| \ll \varepsilon \quad , \tag{1.1.11}$$

where K is a wave number much greater than the inverse of the integral scale, and Ω is the cumulative enstrophy up to that wave number.

The range of wave numbers for which this is true is defined as inertial range, because the dynamic of the N-S equations in this range is dominated by inertial terms. The upper limit of this range can be actually inferred from the energy flux relation (A.2.19). Assuming that we are in the inertial range, the energy injection is approximately $F_K \simeq \varepsilon$. The cumulative enstrophy

$$\Omega_K = \frac{1}{2}\langle |\omega_{\boldsymbol{K}}^{<}|^2 \rangle = \int_0^K k^2 E(k)\, dk \tag{1.1.12}$$

can be calculated using (1.1.12), giving $\Omega_K \approx (\varepsilon^2 k^4)^{1/3}$. Imposing now the condition $|2\nu\Omega_K| \ll \varepsilon$, we find the dissipation wave number up to which dissipation is negligible compared to the energy flux (constants are omitted):

$$K_d = \left(\frac{\nu^3}{\varepsilon}\right)^{-1/4} \quad . \tag{1.1.13}$$

The inverse of this number is called the Kolmogorov dissipation scale

$$\eta \equiv \left(\frac{\nu^3}{\varepsilon}\right)^{1/4} \quad , \tag{1.1.14}$$

which sets the upper limit for the so called dissipation range. In this range the energy input from non linear interactions and the energy drain from viscous dissipation are in exact balance.

1.2 Turbulent kinetic energy dissipation

The kinetic energy of the fluid (per unit mass) is

$$E(\boldsymbol{x},t)\equiv\frac{1}{2}\boldsymbol{U}(\boldsymbol{x},t)\cdot\boldsymbol{U}(\boldsymbol{x},t) \quad . \tag{1.2.1}$$

The mean of E can be decomposed in two parts

$$\langle E(\boldsymbol{x},t)\rangle=\overline{E}(\boldsymbol{x},t)+k(\boldsymbol{x},t) \tag{1.2.2}$$

where $\overline{E}(\boldsymbol{x},t)$ is the kinetic energy of the mean flow

$$\overline{E}(\boldsymbol{x},t)\equiv\frac{1}{2}\langle\boldsymbol{U}\rangle\cdot\langle\boldsymbol{U}\rangle \quad , \tag{1.2.3}$$

and k(**x**, t) is the turbulent kinetic energy

$$k(\boldsymbol{x},t)\equiv\frac{1}{2}\langle\boldsymbol{u}\cdot\boldsymbol{u}\rangle=\frac{1}{2}\langle u_i\cdot u_i\rangle \quad . \tag{1.2.4}$$

This decomposition follows from the Reynolds decomposition of the flow velocity in mean and fluctuating components as $\boldsymbol{U}=\langle\boldsymbol{U}\rangle+\boldsymbol{u}$. The turbulent kinetic energy k determines the isotropic part of the Reynolds stress tensor (which equals $\frac{2}{3}k\delta_{ij}$) but also constitutes an upper bound for the anisotropic parts.

The instantaneous kinetic energy

The equation for the evolution of E, obtained from the Navier-Stokes equations, is

$$\frac{DE}{Dt}+\nabla\cdot\boldsymbol{T}=-2\nu S_{ij}S_{ij} \quad , \tag{1.2.5}$$

where $S_{ij}\equiv\frac{1}{2}(\partial U_i/\partial x_j+\partial U_j/\partial x_i)$ is the rate of strain tensor and

$$T_i\equiv U_i\frac{p}{\rho}-2\nu U_j S_{ij} \quad , \tag{1.2.6}$$

is the flux of energy. The integral of equation (1.2.5) over a fixed control volume is

$$\frac{d}{dt}\int\int\int_V E\,dV+\int\int_A(\boldsymbol{U}E+\boldsymbol{T})\cdot\boldsymbol{n}\,dA=-\int\int\int_V 2\nu S_{ij}S_{ij}\,dV \quad . \tag{1.2.7}$$

As usual the surface integral accounts for inflow, outflow and work done over the surface of the control volume, modelling the transport of energy. The right hand side is a non-negative term that acts as a sink of energy, transforming it from mechanical into internal energy, modelling dissipation. Note that there is no source of energy within the flow.

The mean kinetic energy

The equation for the mean kinetic energy $\langle E \rangle$ is simply obtained by taking the mean of equation (1.2.5):

$$\frac{\overline{D}\langle E\rangle}{\overline{D}t}+\nabla\cdot\left(\langle \boldsymbol{u}\, E\rangle+\langle \boldsymbol{T}\rangle\right)=-\bar{\varepsilon}-\varepsilon \quad . \tag{1.2.8}$$

The two terms on the right hand side are

$$\bar{\varepsilon}\equiv 2\nu\,\overline{S_{ij}}\,\overline{S_{ij}} \quad , \tag{1.2.9}$$

$$\varepsilon\equiv 2\nu\langle s_{ij}s_{ij}\rangle \quad , \tag{1.2.10}$$

where $\overline{S_{ij}}$ and s_{ij} are the mean and fluctuating rate of strain tensor

$$\overline{S_{ij}}=\langle S_{ij}\rangle\equiv\frac{1}{2}\left(\frac{\partial\langle U_i\rangle}{\partial x_j}+\frac{\partial\langle U_j\rangle}{\partial x_i}\right) \quad , \tag{1.2.11}$$

$$s_{ij}=S_{ij}-\langle S_{ij}\rangle\equiv\frac{1}{2}\left(\frac{\partial u_i}{\partial x_j}+\frac{\partial u_j}{\partial x_i}\right) \quad . \tag{1.2.12}$$

The first contribution, $\bar{\varepsilon}$, is the dissipation due to the mean flow which generally is of order Re^{-1} compared with other terms, and therefore negligible.

The mean flow and turbulent kinetic energy

The equations (1.2.3) and (1.2.4) can be rewritten as

$$\frac{\overline{D}\,\overline{E}}{\overline{D}\,t}+\nabla\cdot\overline{\boldsymbol{T}}=-P-\bar{\varepsilon} \quad , \tag{1.2.13}$$

$$\frac{\overline{D}\,k}{\overline{D}t}+\nabla\cdot\boldsymbol{T}'=P-\varepsilon \quad . \tag{1.2.14}$$

The quantity

$$P\equiv-\langle u_i u_j\rangle\frac{\partial\langle U_i\rangle}{\partial x_j} \quad , \tag{1.2.15}$$

is generally positive and acts as a source in equation (1.2.14). Because of this it's referred to as the turbulent energy production, or simply production.

Equations (1.2.13) and (1.2.14) show the important role played by production. The action of the mean velocity gradient working against the Reynolds stresses removes kinetic energy from the mean flow and transfers it to the fluctuating velocity field.

Dissipation

In equation (1.2.14) the sink term is the turbulent kinetic energy dissipation, or simply dissipation. The fluctuating velocity gradients $(\partial u_i/\partial x_j)$ working against the fluctuating deviation stresses $(2\nu s_{ij})$ transform the kinetic energy into internal energy. This results in a raise of temperature that is almost always negligible.

The local instantaneous energy dissipation rate is defined as the limit of $\varepsilon_r, r\to 0$,

$$\begin{aligned}\varepsilon_0 &\equiv 2\nu\, s_{ij}\, s_{ij} \\ &= \frac{\nu}{2}\left(\frac{\partial u_i}{\partial x_j}+\frac{\partial u_j}{\partial x_i}\right)^2\end{aligned} \tag{1.2.16}$$

so as can be seen by the definition, the dissipation is always non-negative.

Note that just as the mean velocity profiles, with proper scaling also the production and dissipation become self similar (i.e. independent of Re and x, for large enough Re and x/D. See chapter 1.4 for a more rigorous definition of self-similarity in jet flows).

This is experimentally confirmed (Hussein 1994) and will be used as an assumption in the measurements done in this thesis. Consequently, the scaling used in the jet flow is

$$\hat{P} \equiv P/\left(U_o^3/r_{1/2}\right) \quad , \tag{1.2.17}$$

$$\hat{\varepsilon} \equiv \varepsilon/\left(U_o^3/r_{1/2}\right) \quad . \tag{1.2.18}$$

The *pseudo-dissipation* $\tilde{\varepsilon}$ is defined by

$$\tilde{\varepsilon} \equiv \nu\left\langle \frac{\partial u_i}{\partial x_j}\frac{\partial u_i}{\partial x_j}\right\rangle \quad , \tag{1.2.19}$$

and is related to the true dissipation ε by

$$\tilde{\varepsilon} = \varepsilon - \nu\frac{\partial^2\langle u_i u_j\rangle}{\partial x_i \partial x_j} \quad . \tag{1.2.20}$$

In virtually all circumstances, the final term in equation 1.2.16 is small (at most a few percent of ε) and consequently the distinction between ε and $\tilde{\varepsilon}$ is seldom important.

Measuring ε_0 requires the simultaneous acquisition of nine velocity derivatives resolved in space such that r is less than any dynamically relevant length scale in the flow, and temporally resolved at a correspondingly small time scale. The challenge of making such measurements encourages the consideration of surrogates for ε_0 based on a subset of the nine components of the strain rate. Traditionally the surrogate of choice is (Laufer, 1952)

$$\varepsilon = 15\nu\left\langle\left(\frac{\partial u}{\partial x}\right)^2\right\rangle \quad , \tag{1.2.21}$$

which, as we shall see in section 4, often gives poor results and is theoretically valid only for homogeneous and isotropic turbulence.

The budget of the turbulent kinetic energy

For the self-similar round jet the turbulent kinetic energy budget is shown in Figure 1. The quantities plotted are the four terms in equation (1.2.14) normalized by $U_0^3/r_{1/2}$. The contributions are production, P; dissipation, ε; mean flow convection, $-\overline{D}k/\overline{D}t$; turbulent trasport $-\nabla\cdot\boldsymbol{T}'$. While production and mean flow convection are historically measured with uncertainties within 20%, the error on dissipation and turbulent transport can be as big a a factor of two or more.

Along the jet, dissipation is a dominant term. Production peaks at $r/r_{1/2}\approx 0.6$, where the ratio $P/\varepsilon\approx 0.8$. At the edge of the jet production goes to zero, and dissipation is balanced by the transport.

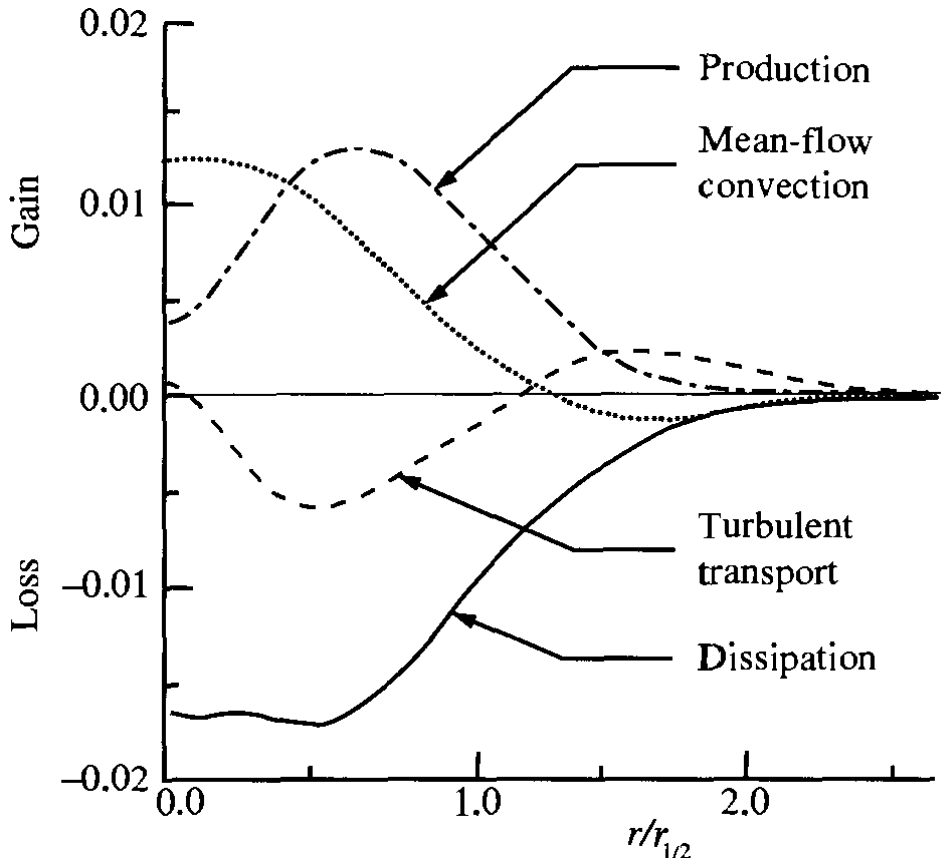

Figure 1: The turbulent kinetic energy budget in the self-similar round jet. Quantities are normalized by U_0 and $r_{1/2}$. (Panchapachesan & Lumely 1993)

1.3 Wall bounded flows

The vast majority of turbulent flows are bounded by one or more surfaces. Examples of internal flows are channel and pipe flows, while external flows are encountered when dealing with boundary layers. In this thesis it will be presented a simulation of a channel flow, so it's appropriate to give some background theory of his fundamental flow. Central issues are the mean velocity profiles, the friction laws and the turbulent energy balance, that will now be discussed.

Channel flow

Consider the flow along a rectangular duct $\left(\frac{L}{\delta}\gg 1\right)$ of large aspect ratio $\left(\frac{b}{\delta}\gg 1\right)$.

The resulting mean flow is predominantly in the longitudinal (or x) direction, while the mean velocity varies mostly in the transversal (or y) direction. All the flow statistics are independent of the spanwise (or z) position.

Focusing the study on the fully developed region (so large values of x) the flow results statistically stationary and one-dimensional (varies only along y).

For the channel flow we define two velocities, and their respective Reynolds numbers:

- centreline velocity $U_0 \equiv \langle U \rangle_{y=\delta}$, $\Re e_0 \equiv \frac{\delta U_0}{\nu}$
- bulk velocity $\bar{U} \equiv \frac{1}{\delta}\int_0^{\delta} \langle U \rangle dy$, $\Re e \equiv \frac{(2\delta)\bar{U}}{\nu}$.

Balance of mean forces

Since $\langle W \rangle = 0$ and $\frac{d\langle U \rangle}{dx} = 0$, from the continuity equation involving the mean velocities components we can say that:

$$\frac{d\langle V \rangle}{dy} = 0 \tag{1.3.1}$$

and considering the impermeability condition at the wall we conclude that $\langle V \rangle = 0$ for all y.

The mean momentum balance in y direction is then:

$$0 = -\frac{d}{dy}\langle v^2 \rangle - \frac{1}{\rho}\frac{\partial \langle p \rangle}{\partial y} \tag{1.3.2}$$

which using the boundary condition $\langle v^2 \rangle_{y=0} = 0$ integrates to:

$$\langle v^2\rangle+\langle p\rangle/\rho=p_w(x)/\rho \quad \text{,where} \quad p_w=\langle p(x,0,0)\rangle \quad . \tag{1.3.3}$$

This is useful to deduce that the mean axial pressure gradient is uniform across the flow:

$$\frac{\partial\langle p\rangle}{\partial x}=\frac{d\,p_w}{d\,x} \quad . \tag{1.3.4}$$

The mean momentum balance in x direction is:

$$0=\nu\frac{d^2\langle U\rangle}{dy^2}-\frac{d}{dy}\langle u\,v\rangle-\frac{1}{\rho}\frac{\partial\langle p\rangle}{\partial x} \tag{1.3.5}$$

and can be rewritten as:

$$\frac{d\,\tau}{dy}=\frac{d\,p_w}{dx} \tag{1.3.6}$$

where the total shear stress is defined as:

$$\tau(y)\equiv\rho\nu\frac{d\langle U\rangle}{dy}-\rho\langle u\,v\rangle \tag{1.3.7}$$

Since τ is a function of only y, and p_w is a function of only x, it's clear from (1.3.6) that both $d\,\tau/dy$ and $d\,p_w/dx$ are constant. Taking the boundary conditions into consideration:

$$\tau(y)=\tau_w\left(1-\frac{y}{\delta}\right) \quad \text{, where} \quad \tau_w\equiv\tau(0) \quad . \tag{1.3.8}$$

The normalization of the wall shear stress is referred to as skin friction coefficient, based on the centreline or on the bulk velocity:

$$c_f\equiv\frac{\tau_w}{\frac{1}{2}\rho U_0^2} \quad , \quad C_F\equiv\frac{\tau_w}{\frac{1}{2}\rho\bar{U}^2} \quad . \tag{1.3.9}$$

The flow is driven by the drop in pressure between entrance and exit. In the fully developed flow region there is a constant negative mean pressure gradient $\frac{\partial\langle p\rangle}{\partial x}=\frac{d\,p_w}{dx}$ balanced by the shear stress gradient $\frac{d\,\tau}{dy}=-\frac{\tau_w}{\delta}$.

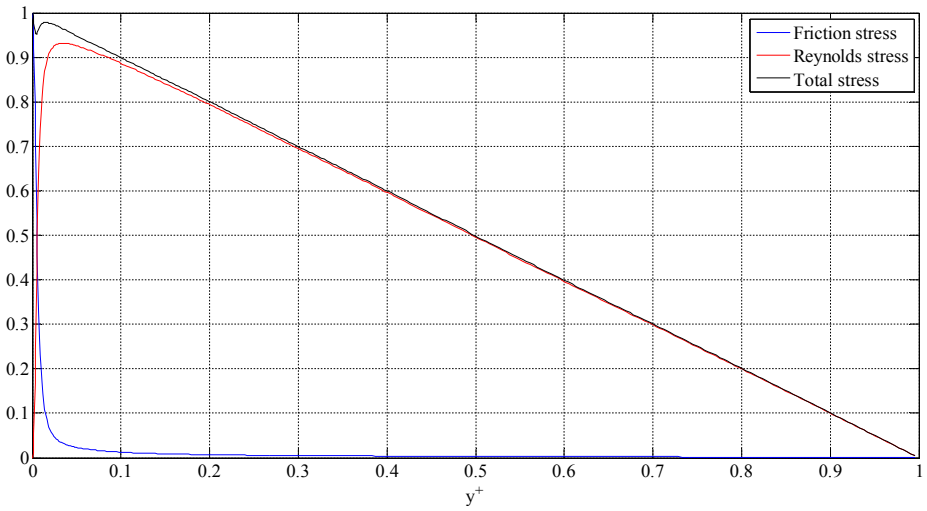

Figure 2: Profiles of the viscous shear stress, and the Reynolds shear stress in turbulent channel flow. DNS data from Jimenez (2008), Re=2000.

Near wall shear stress

The total shear stress is the sum of viscous stress and Reynolds stress. At the wall the no slip condition $\boldsymbol{U}(\boldsymbol{x},t)=0$ makes it so that the Reynolds stress is zero. So at the wall the shear stress is entirely of viscous origin:

$$\tau_w = \rho\nu\left(\frac{d\langle U\rangle}{dy}\right)_{y=0} . \tag{1.3.10}$$

Profiles of the viscous and Reynolds shear stresses obtained with a DNS are shown in Figure 2.

It's clear that close to the wall the viscosity ν and the wall shear stress τ_w are important parameters. From these quantities (and ρ) we define some viscous scales to be used near the wall:

- friction velocity $u_\tau \equiv \sqrt{\frac{\tau_w}{\rho}}$
- viscous lengthscale $\delta_\nu \equiv \nu\sqrt{\frac{\rho}{\tau_w}} = \frac{\nu}{u_\tau}$
- friction Reynolds number $\Re e_\tau \equiv \frac{u_\tau \delta}{\nu} = \frac{\delta}{\delta_\nu}$
- wall units $y^+ \equiv \frac{y}{\delta_\nu} = \frac{u_\tau y}{\nu}$

Different regions in the near wall flow are defined based on y^+ . The viscous wall region

$(y^+<50)$ is directly affected by molecular viscosity, while the outer region $(y^+>50)$ can neglect viscous effects. Within the viscous region there's the viscous sub-layer $(y^+<5)$ where the Reynolds shear stress is negligible compared to the viscous stress.

Mean velocity profiles

Channel flow is completely specified by ρ, ν, δ, u_τ. With no assumptions and adopting a non dimensional function Φ (to be determined) we can write:

$$\frac{d\langle U\rangle}{dy}=\frac{u_\tau}{y}\Phi\left(\frac{y}{\delta_\nu},\frac{y}{\delta}\right) \tag{1.3.11}$$

keeping in mind that δ_ν is the appropriate lengthscale in the near wall region, while δ is suitable for the outer region.

The law of the wall

Following Prandtl hypothesis, close to the wall the mean velocity profile is determined by the viscous scales. Mathematically Φ asymptotically tends to a function of only y/δ_ν as $y/\delta\to 0$:

$$\frac{d\langle U\rangle}{dy}=\frac{u_\tau}{y}\Phi_1\left(\frac{y}{\delta_\nu}\right) \text{ , for } \frac{y}{\delta}\ll 1 \tag{1.3.12}$$

where

$$\Phi_1\left(\frac{y}{\delta_\nu}\right)=\lim_{y/\delta\to 0}\Phi\left(\frac{y}{\delta_\nu},\frac{y}{\delta}\right) \text{ .} \tag{1.3.13}$$

Defining $u^+(y^+)$ as

$$u^+\equiv\frac{\langle U\rangle}{u_\tau} \tag{1.3.14}$$

we can rewrite the previous relation as:

$$\frac{du^+}{dy^+}=\frac{1}{y^+}\Phi_1(y^+) \tag{1.3.15}$$

which after integration is the law of the wall:

$$u^+=f_w(y^+)=\int_0^{y^+}\frac{1}{y'}\Phi_1(y')dy' \text{ .} \tag{1.3.16}$$

Note that, for $\frac{y}{\delta}\ll 1$, u^+ is a function of solely y^+ . For Reynolds numbers away

from transition there is experimental proof that the function $f_w(y^+)$ is universal for channel, pipe and boundary layers. The form of the function $f_w(y^+)$ can be determined for small and large values of y^+ .

Viscous sub-layer

At the wall the no slip condition imposes $f_w(0)=0$, $f_w'(0)=1$. Using a Taylor expansion:

$$f_w(y^+)=y^+ +\mathrm{O}(y^{+2}) \tag{1.3.17}$$

As shown in Figure 3 the linear relation holds well for the viscous sub-layer $(y^+<5)$.

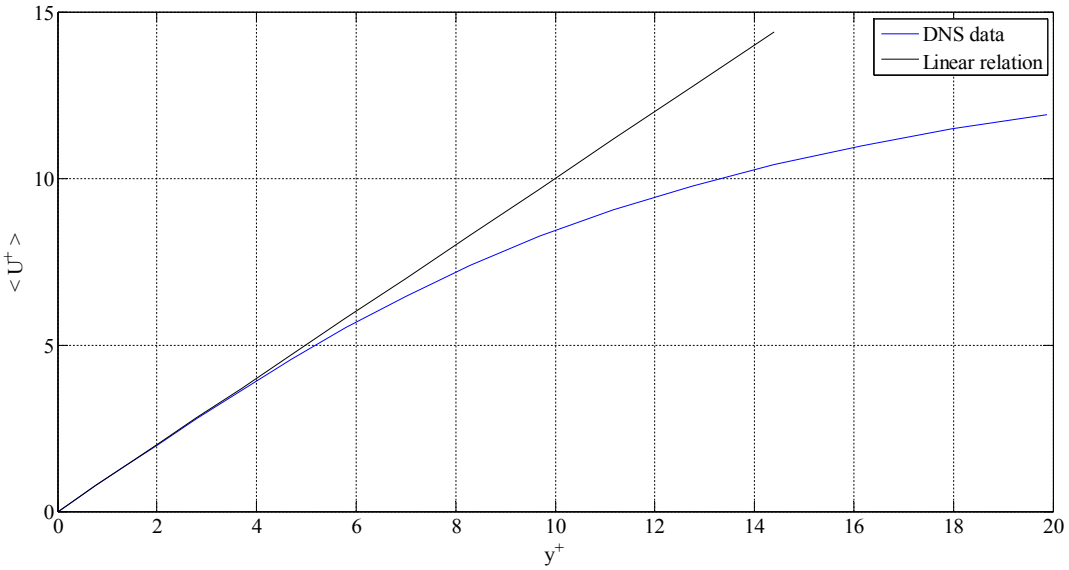

Figure 3: Near wall profiles of mean velocity from the DNS of Jimenez (2008), Re=2000.

The log law

For larger y^+ we suppose that viscosity has little effect, so that Φ_1 assumes a constant value:

$$\Phi_1(y^+)=\frac{1}{k} \quad \text{for} \quad \frac{y}{\delta}\ll 1 \quad , \quad y^+\gg 1 \tag{1.3.18}$$

where k is the Von Kármán constant. So in this region the mean velocity gradient is given by:

$$\frac{du^+}{dy^+}=\frac{1}{k\,y^+} \tag{1.3.19}$$

which easily integrates to give the log law:

$$u^+ = \frac{1}{k}\ln(y^+) + B \quad . \tag{1.3.20}$$

The values of the constants are determined experimentally and are taken to be within 5% of

$$k = 0.41 \quad , \quad B = 5.2 \quad . \tag{1.3.21}$$

As shown in Figure 4 the law holds very well for $y^+ > 30$ and $\frac{y}{\delta} < 0.3$. The region between the viscous sub-layer and the log-law region is called buffer layer, where transition form viscosity dominated to turbulence dominated flow occurs.

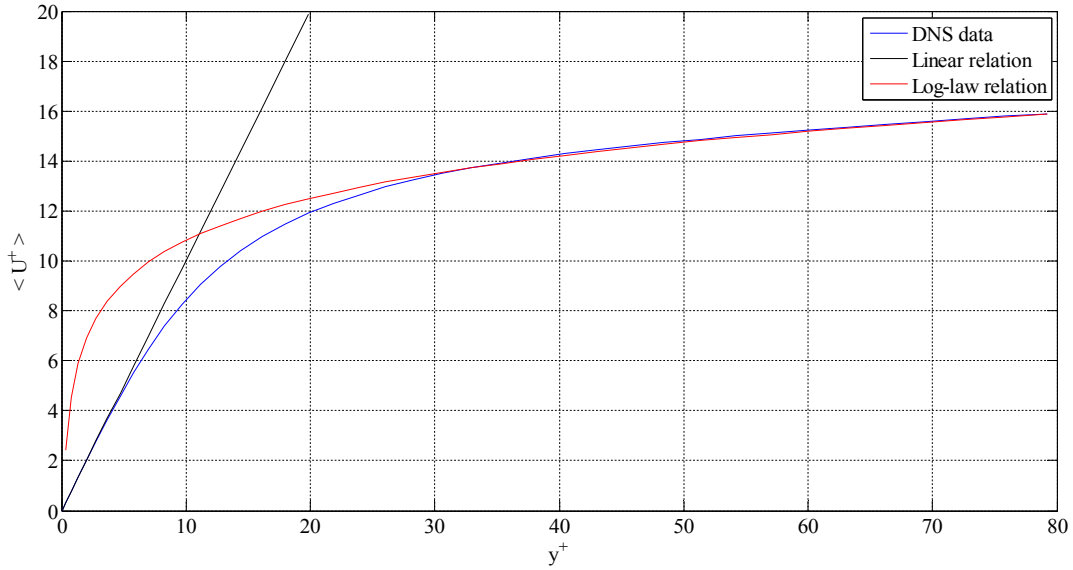

Figure 4: Near wall profiles of mean velocity, DNS data from Jimenez (2008), Re=2000.

The velocity defect law

In the outer layer $(y^+ > 50)$ we assume that Φ becomes independent of the viscosity

$$\Phi_0\left(\frac{y}{\delta}\right) = \lim_{y/\delta_\nu \to \infty} \Phi\left(\frac{y}{\delta_\nu}, \frac{y}{\delta}\right) \tag{1.3.22}$$

leading to:

$$\frac{d\langle U\rangle}{dy} = \Phi_0\left(\frac{y}{\delta}\right) \quad . \tag{1.3.23}$$

Integrating from a generic y/δ to the centre of the channel we obtain the velocity defect law:

$$\frac{U_0 - \langle U\rangle}{u_\tau} = F_D\left(\frac{y}{\delta}\right) = \int_{y/\delta}^{1} \frac{1}{y'}\Phi_0(y')\,dy' \quad . \tag{1.3.24}$$

The velocity defect is the difference between the centreline velocity and the mean velocity.

The law states that this difference, normalized by the friction velocity, depends on y/δ only. There is no suggestion that F_D is universal, because it generally varies in different flows.

At high enough Reynolds number (generally Re > 10^4) there is an overlap region between the inner layer $(y/\delta < 0.1)$ and the outer layer $(y/\delta_\nu > 50)$. In this region both equations (1.3.18) and (1.3.22) must be true, implying that

$$\frac{y}{u_\tau}\frac{d\langle U\rangle}{dy} = \Phi_1\left(\frac{y}{\delta_\nu}\right) = \Phi_0\left(\frac{y}{\delta}\right) \quad \text{, for} \quad \delta_\nu \ll y \ll \delta \quad . \tag{1.3.25}$$

This equation is satisfied in the overlap region only by Φ_1 and Φ_0 assuming a constant value:

$$\frac{y}{u_\tau}\frac{d\langle U\rangle}{dy} = \frac{1}{k} \quad \text{, for} \quad \delta_\nu \ll y \ll \delta \quad . \tag{1.3.26}$$

We can now determine the form of the velocity defect law for small y/δ to be:

$$\frac{U_0 - \langle U\rangle}{u_\tau} = F_D\left(\frac{y}{\delta}\right) = -\frac{1}{k}\ln\left(\frac{y}{\delta}\right) + B_1 \quad \text{, for} \quad \frac{y}{\delta} \ll 1 \tag{1.3.27}$$

where B_1 is a flow dependent constant. To determine it's value, note that as shown in Figure 4 the log law is reasonably close to the DNS value even in the central part of the channel $(0.3 < y/\delta < 1)$ where no arguments support it. Extrapolating the centreline velocity from the log law we obtain a way to determine B_1 :

$$\frac{U_0 - U_{0,\log}}{u_\tau} = B_1 \tag{1.3.28}$$

which results in a very small value since $U_0 - U_{0,\log}$ is within 1% of U_0 . DNS data lead to $B_1 \approx 0.2$, while experimental results indicate $B_1 \approx 0.7$.

Wall regions recap

Region	Location	Property
Inner layer	$y/\delta<0.1$	$\langle U\rangle$ determined by u_τ and y^+, independent of U_0 and δ
Viscous wall region	$y^+<50$	Significant contribution to the shear stress due to viscosity
Viscous sub-layer	$y^+<5$	Reynolds shear stress is negligible compared to viscous
Outer layer	$y^+>50$	Negligible effect of viscosity on $\langle U\rangle$
Overlap region	$y^+>50,\ y/\delta<0.1$	Present only at high Reynolds
Log law region	$y^+>30,\ y/\delta<0.3$	Log law holds
Buffer layer	$5<y^+<30$	Transitional region between viscous and turbulent dominated flow

The friction law

The aim is now to determine the Reynolds number dependence of the skin friction coefficient an other relevant quantities.

A good estimate of the bulk velocity come from the application of the log law to the whole channel. As stated before there are small deviations near the centreline, while the substantial deviations in the near wall region can be overlooked since they have a negligible contribution to the integral.

With this approximation:

$$\frac{U_0-\bar{U}}{u_\tau}=\frac{1}{\delta}\int_0^\delta \frac{U_0-\langle U\rangle}{u_\tau}dy\simeq\frac{1}{\delta}\int_0^\delta -\frac{1}{k}\ln\left(\frac{y}{\delta}\right)dy=\frac{1}{k}\approx 2.4 \qquad (1.3.29)$$

having taken $B_1=0$ for consistency at $y=\delta$.

Consider the log law in the inner layer

$$\frac{\langle U \rangle}{u_\tau} = \frac{1}{k} \ln\left(\frac{y}{\delta_\nu}\right) + B \tag{1.3.30}$$

and in the outer layer

$$\frac{U_0 - \langle U \rangle}{u_\tau} = -\frac{1}{k} \ln\left(\frac{y}{\delta}\right) + B_1 \tag{1.3.31}$$

combining them leads to:

$$\frac{U_0}{u_\tau} = \frac{1}{k} \ln\left(\frac{\delta}{\delta_\nu}\right) + B + B_1 = \frac{1}{k} \ln\left[\Re\, e_0 \left(\frac{U_0}{u_\tau}\right)^{-1}\right] + B + B_1 \tag{1.3.32}$$

which is independent of y. Solving this for U_o/u_τ we can calculate (for each given $\Re\, e_0$) the skin friction coefficient, using:

$$c_f \equiv \frac{\tau_w}{\frac{1}{2}\rho U_0^2} = 2\left(\frac{u_\tau}{U_0}\right)^2 \tag{1.3.33}$$

and with approximation (1.3.29) also

$$C_F \equiv \frac{\tau_w}{\frac{1}{2}\rho \bar{U}^2} \quad . \tag{1.3.34}$$

Reynolds stresses

Consider the DNS data at Re = 13'750 shown in Figure 5, Figure 6 and Figure 7. The flow is divided into three regions:

- viscous wall region for $y^+ < 50$
- log law region for $y^+ > 50,\ y/\delta < 0.3$ or equivalently $50 < y^+ < 120$
- core region for $y/\delta > 0.3$ or equivalently $y^+ > 120$

In the log law region there is approximate self-similarity. The normalized Reynolds stresses $\frac{\langle u_i u_j \rangle}{k}$ are almost uniform, as is the production to dissipation ratio $\frac{P}{\varepsilon}$ and the normalized mean shear rate $\frac{S\,k}{\varepsilon}$. Moreover, production and dissipation are in balance, meaning $\frac{P}{\varepsilon} \approx 1$.

In the core region the mean velocity gradient and the shear stress vanish, leading to P → 0.

In the viscous wall region, production, dissipation, turbulent kinetic energy and anisotropy achieve their peaks. Consider the fluctuation velocity components near the wall (small y) at a fixed point in space and time, expressed through a Taylor expansion:

$$\begin{aligned} u &= a_1 + b_1 y + c_1 y^2 + \dots \\ v &= a_2 + b_2 y + c_2 y^2 + \dots \\ w &= a_3 + b_3 y + c_3 y^2 + \dots \end{aligned} \tag{1.3.35}$$

for the no slip condition and the impermeability at the wall $a_1 = a_2 = a_3 = 0$. Since u and w are zero at the wall for every x and z, we can state that

$$\left(\frac{\partial u}{\partial x}\right)_{y=0} = 0 \quad \text{and} \quad \left(\frac{\partial w}{\partial z}\right)_{y=0} = 0 \tag{1.3.36}$$

so for the continuity equation:

$$\left(\frac{\partial v}{\partial y}\right)_{y=0} = 0 = b_2 \quad . \tag{1.3.37}$$

This means that close to the wall the flow has only two components, i.e. the motion occurs in planes parallel to the wall.

Taking the mean of the series products gives the Reynolds stresses:

$$\begin{aligned} \langle u^2 \rangle &= \langle b_1^2 \rangle y^2 + \dots \\ \langle v^2 \rangle &= \langle c_2^2 \rangle y^4 + \dots \\ \langle w^2 \rangle &= \langle b_3^2 \rangle y^2 + \dots \\ \langle u v \rangle &= \langle b_1 c_2 \rangle y^3 + \dots \end{aligned} \tag{1.3.38}$$

For fully developed channel flow, the turbulent kinetic energy balance equation is:

$$P - \tilde{\varepsilon} + \nu \frac{d^2 k}{dy^2} - \frac{d}{dy}\langle \frac{1}{2} \nu \bar{\boldsymbol{u}} \cdot \bar{\boldsymbol{u}} \rangle - \frac{1}{\rho} \frac{d}{dy} \langle \nu p' \rangle = 0 \tag{1.3.39}$$

where the terms are respectively production, pseudo-dissipation, viscous diffusion, turbulent convection and pressure transport.

Peak production occurs in the buffer layer at $y^+ \approx 12$. Here $\frac{P}{\varepsilon} \approx 1.8$ so the excess energy is transported away. Pressure transport is very small. Turbulent convection transports both in the log wall region and in the near wall region. Viscous diffusion transports energy all the way towards the wall. The dissipation at the wall is balanced by the viscous transport,

$$\varepsilon = \tilde{\varepsilon} = \nu \frac{d^2 k}{dy^2} \quad \text{, for y =2.} \tag{1.3.40}$$

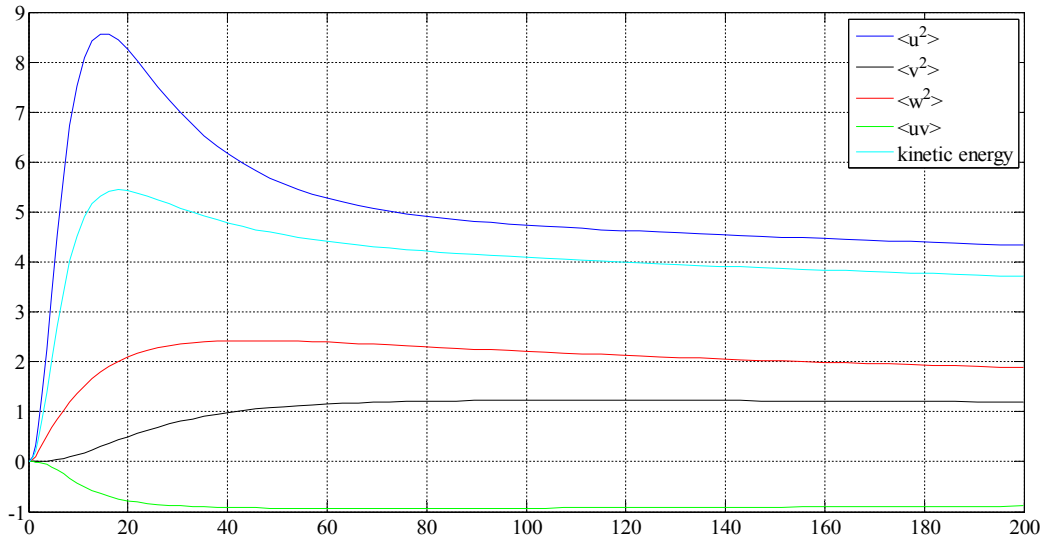

Figure 5: Reynolds stresses and kinetic energy normalized by the friction velocity against y^+ from DNS of channel flow at Re=2000 (Jimenez 2008).

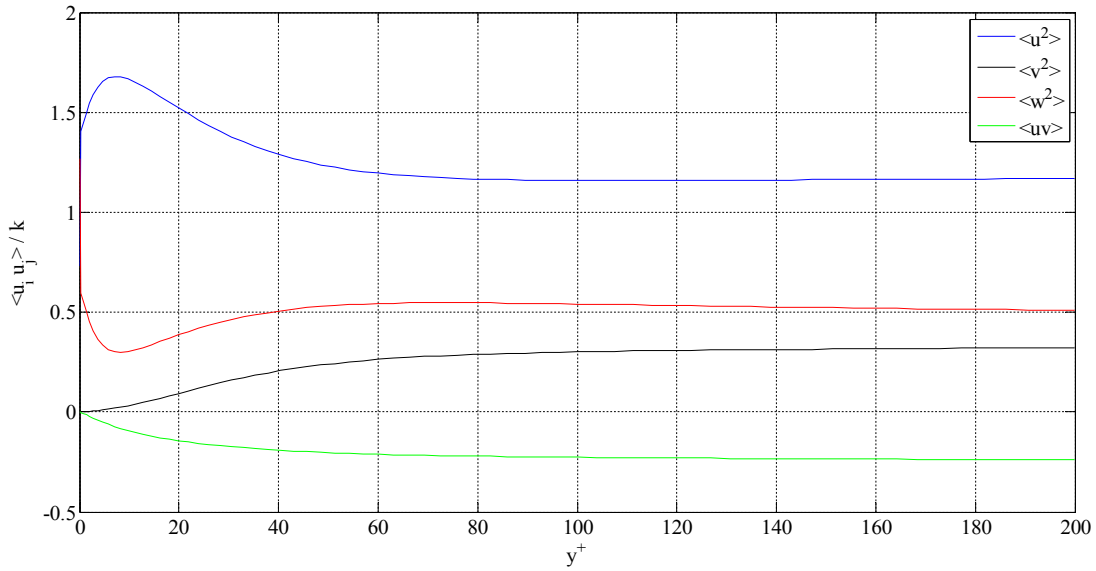

Figure 6: Profiles of Reynolds stresses normalized by the turbulent kinetic energy from DNS of channel flow at Re=2000 (Jimenez 2008).

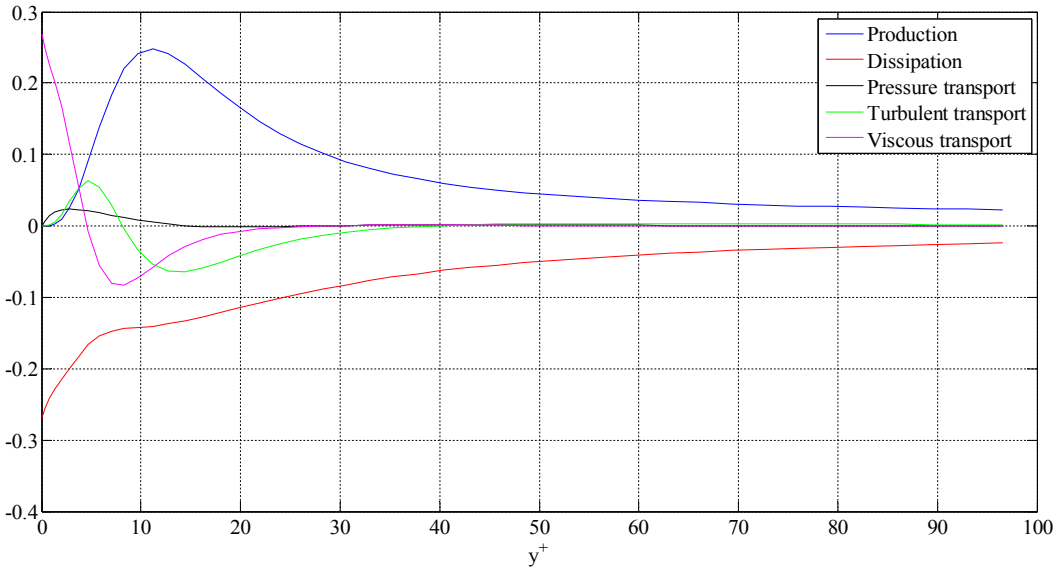

Figure 7: Profiles of the energy balance components from DNS of channel flow at Re=2000 (Jimenez 2008).

1.4 Free shear flows

The most commonly free shear flows are jets, wakes and mixing layers. The main characteristic of these flows is that they are away from walls so that the turbulence in the flow is caused only by differences in the mean velocity. Most of the experimental and numerical work in this thesis is about round jets, so the well known theory for this flow is now reminded here.

Round Jet flow

A round jet consist ideally of a Newtonian fluid, flowing steadily through a round nozzle of diameter d, which produces a flat top-hat velocity profile U_J. The jet flow enters an ambient filled with the same fluid, which is at rest at infinity. The flow is also statistically stationary and axisymmetric, hence all statistics are independent of the time and the azimuthal coordinate ϑ. The velocity components along the cylindrical coordinate system (x, r, θ) are respectively (U, U_r, U_θ) .

The flow is completely defined by U_j, d and ν so the only non-dimensional parameter defining it is $\Re e = U_J d/\nu$, even if in practice there is some dependence on details of the nozzle and the surroundings (Schneider 1985; Hussein 1994).

The mean velocity field

As expected the mean velocity is predominantly in the axial direction, with the mean azimuthal velocity being zero and the mean radial velocity being one order of magnitude smaller.

Defining the centreline velocity as

$$U_0(x) \equiv \langle U(x,0,0) \rangle \quad , \tag{1.4.1}$$

and the jet's half width, $r_{1/2}$, as

$$\langle U(x, r_{1/2}(x), 0) \rangle = \frac{1}{2} U_0(x) \quad , \tag{1.4.2}$$

one can observe that after an initial development region (say $0 \le x/d \le 25$) the axial mean velocity profile becomes self-similar. This means that as the jet decays and spreads, the mean velocity profile changes, but with proper scaling the shape of the profile is preserved.

To further investigate the jet self-similarity, it is necessary to determine the variation of $U_0(x)$ and $r_{1/2}(x)$. In Figure 9 the data for (the inverse of) $U_0(x)$ is plotted against x/d, resulting in a linear behaviour. The intercept of this line with the abscissa defines the so called "virtual origin", denoted by x_0 . The mathematical relation describing this trend is

$$\frac{U_0(x)}{U_j} = \frac{B}{(x - x_0)/d} \quad , \tag{1.4.3}$$

where B is an empirical constant called velocity decay. Note that equation (1.4.3) does not formally hold in the development region, and is artificially prolonged there with the only purpose of calculating the virtual origin.

The empirical law for the jet's half width is

$$r_{1/2}(x) = S(x - x_0) \quad , \tag{1.4.4}$$

where S is the (constant) spreading rate. The law again holds only in the fully developed region.

Since $U_0(x) \approx x^{-1}$ and $r_{1/2}(x) \approx x$ the local Reynolds number $\Re e_0(x) = U_0(x) r_{1/2}(x)/\nu$ is independent of x. The constants B and S where object of several experiments, summarized in the following table:

	Panchapakesan & Lumley (1993)	Hussein (1994) hot-wire data	Hussein (1994) laser doppler data
Re	11'000	95'500	95'500
S	0,096	0,102	0,094
B	6,06	5,90	5,80

From the table it appears that the spreading rate and the decay velocity are independent of Re for a turbulent and fully developed jet, the only differences being due to experimental uncertainties.

However, even if the flow shows no dependence of Re in the mean axial velocity profile and in the spreading rate after proper scaling, the Reynolds number still influences the absolute size of the small scale structures, making them smaller for larger Reynolds.

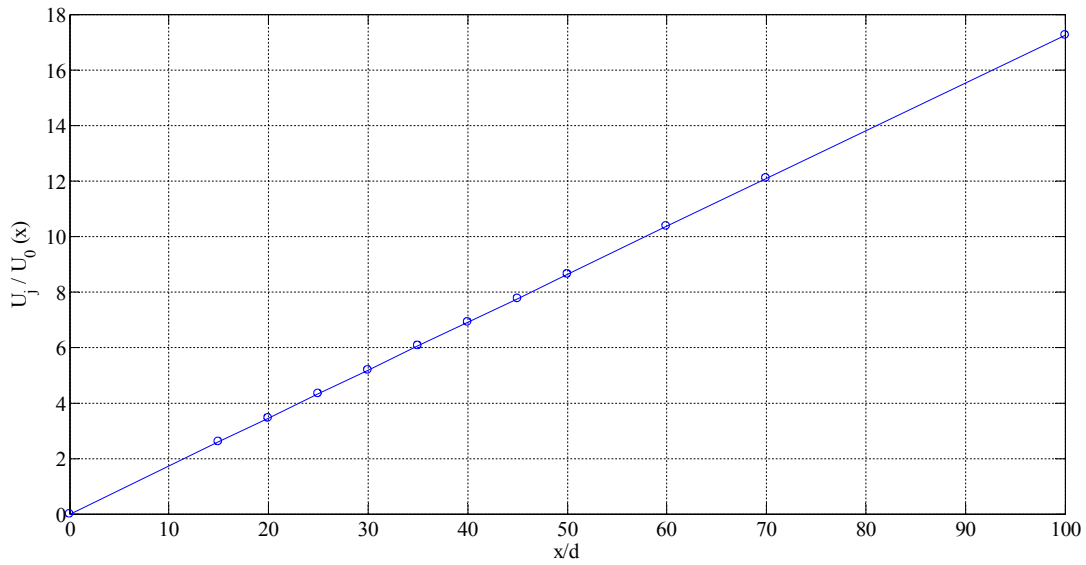

Figure 8: The variation with axial distance of the mean velocity along the centreline in a turbulent round jet, Re=95500. Symbols, experimental data from Hussein (1994); line, equation (1.4.3).

The cross stream similarity variable can be taken to be either

$$\xi \equiv r / r_{1/2} \quad , \tag{1.4.5}$$

or

$$\eta \equiv r / (x - x_0) \quad , \tag{1.4.6}$$

the two being related by $\eta = S\xi$. The self-similar mean velocity profile is defined as

$$f(\eta) = \overline{f}(\xi) = \langle U(x, r, 0) \rangle / U_0(x) \quad , \tag{1.4.7}$$

and shown in Figure 9 for the axial component.

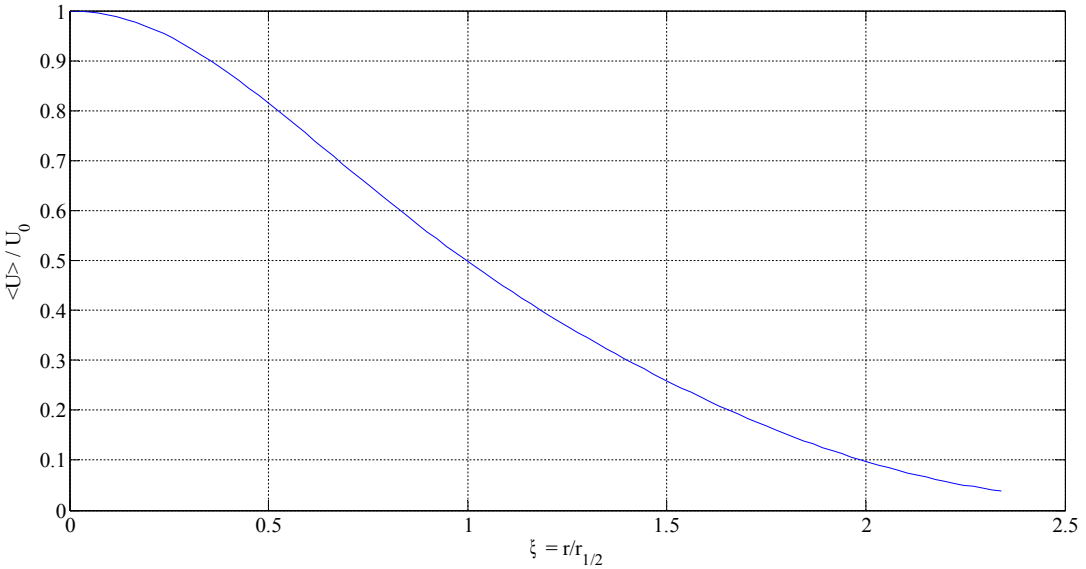

Figure 9: Self-similar profile for the mean axial velocity in the self-similar round jet. (Hussein 1994)

The mean radial component can be calculated from the continuity equation, resulting smaller by a factor of 40 compared with the axial component. The radial velocity becomes negative at the jet far ends, meaning that flow is actually being entrained form the ambient into the jet.

Reynolds stresses

The fluctuating velocity components in the cylindrical coordinate system are (u_x, u_r, u_θ) so it follows that in the turbulent round jet the Reynolds-stress tensor is

$$\begin{bmatrix} \langle u_x^2 \rangle & \langle u_x u_r \rangle & 0 \\ \langle u_x u_r \rangle & \langle u_r^2 \rangle & 0 \\ 0 & 0 & \langle u_\theta^2 \rangle \end{bmatrix}, \tag{1.4.8}$$

because $\langle u_x u_\theta \rangle$ and $\langle u_r u_\theta \rangle$ are zero for axial symmetry.

The Reynolds stresses are also self-similar, i.e. the profiles of $\langle u_i u_j \rangle / U_0(x)^2$ plotted against the radial coordinates $\xi = r/r_{1/2}$ or $\eta = r/(x - x_0)$ collapse for all x beyond the development region as in Figure 10.

The local turbulence intensity is defined as $u'/\langle U \rangle$ where u' is the root mean square (rms) velocity fluctuation $u' \equiv \sqrt{(\langle u^2 \rangle)}$. At the edge of the jet, although the Reynolds stress decays, the ratio increases without bounds, as in Figure 11, starting from a centreline value of 0,25.

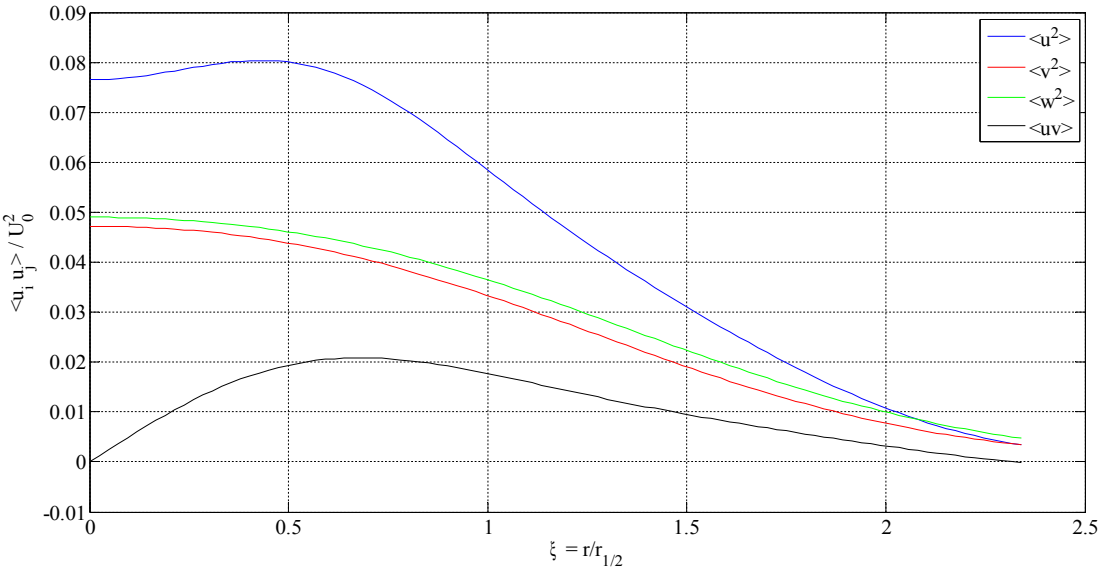

Figure 10: Profiles of Reynolds stresses in the self-similar round jet. (Hussein 1994)

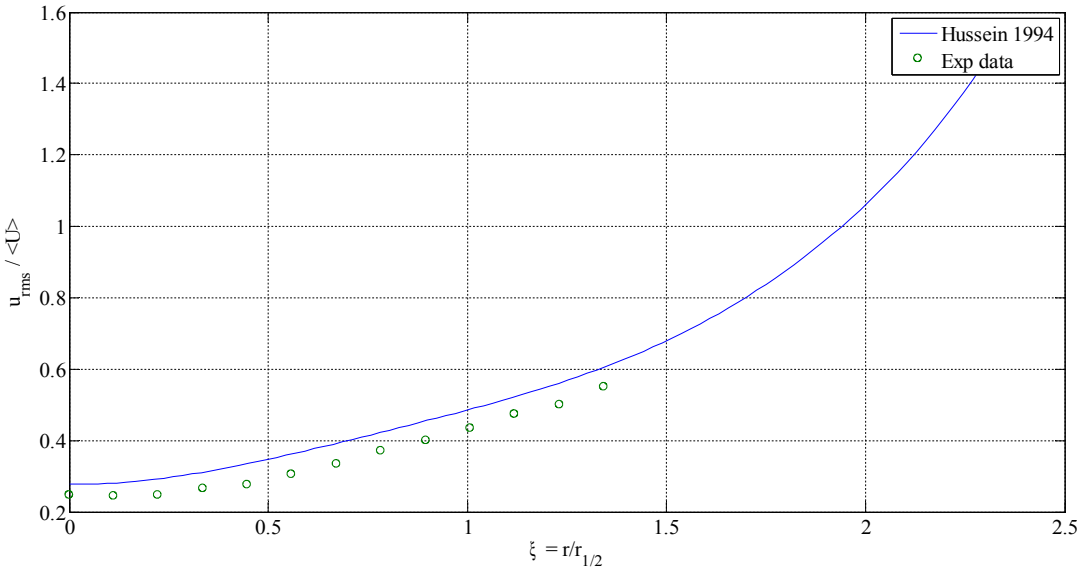

Figure 11: The profile of local turbulence intensity in the self similar round jet. Blue line, data from Hussein 1994; green symbols, data from our facility.

1.5 Hot wire anemometry

Nowadays there are several techniques to estimate the velocity field in an experimental set-up. The main candidates are usually hot-wire anemometry (HWA), laser Doppler velocimetry (LDV) and particle image velocimetry (PIV). For the present experiments we choose HWA, mainly because of it's excellent temporal resolution. Spatial resolution is however a different problem, which is analysed in section (1.6), that can greatly affect the accuracy of measurements.

In HWA, a small wire heated by an electric current is placed in the flow. An electronic circuit connected to the wire measures the heat transferred to the flow that invests the wire, which is proportional to the flow velocity. We operate the wire in Constant Temperature Anemometry (CTA) mode, since the wire is maintained at a constant temperature with a feedback circuit as in Figure 12. The hot wire, shown between C and D, it is part of a Wheatstone bridge, such that the wire resistance is kept constant over the bandwidth of the feedback loop. Since the hot wire voltage is a simple potential division of the output voltage, the output voltage is normally measured for convenience.

Since the circuit response is heavily dependent upon the individual hot wire, the feedback circuit must be tuned for each hot wire (Dantec 1986). Although strictly it is necessary to test the hot wire with velocity perturbations to optimise the frequency response, a much simpler electronic test has been developed that injects a small voltage square wave into the Wheatstone bridge. It has been shown (Freymuth 1977), that the optimum circuit performance is found when the output response is approximately that shown in Figure 13. The square wave test allows a quick estimation of the frequency response, although it has been shown (Moss 1992) that any contamination of the wire reduces the frequency response without any apparent effect on the pulse response.

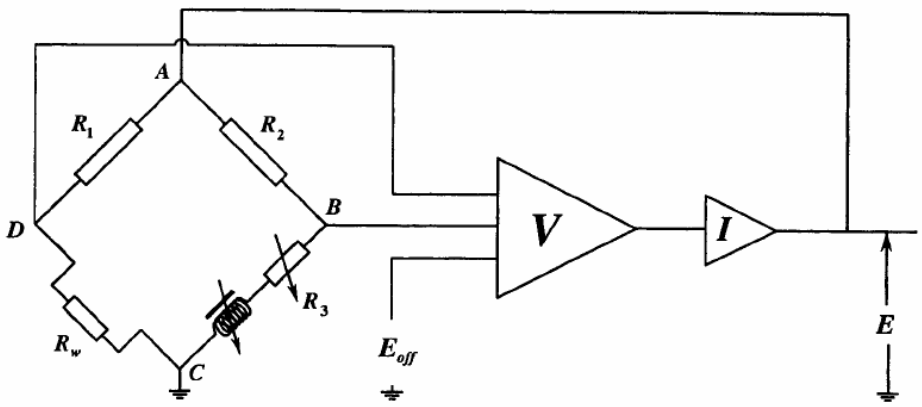

Figure 12: Schematic of constant temperature anemometer. (Sheldrake 1995)

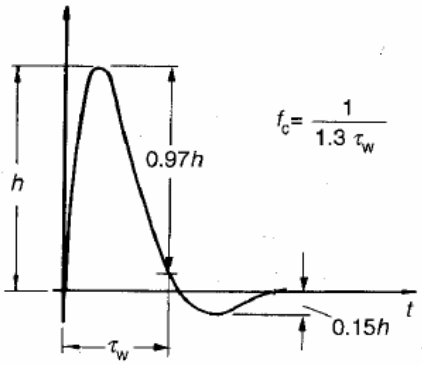

Figure 13: Optimum square-wave test response. (Bruun 1995)

General hot-wire equation

To examine the behaviour of the hot wire, the general hot wire equation must first be derived. This equation will be used to examine both the steady state response of the hot wire, discussed here, and its frequency response, discussed later. By considering a small circular element of the hot wire, as in Figure 14, a power balance can be performed, assuming a uniform temperature over its cross-section:

$$\begin{aligned} I^2 R_w \delta x = \rho_w c_w \frac{\partial T_w}{\partial t} A \delta x + k_w A \frac{\partial T_w}{\partial x} \\ + h \pi d (T_w - T_a) \delta x - k_w A \left(\frac{\partial T_w}{\partial x} + \frac{\partial^2 T_w}{\partial x^2} \delta x \right) + \sigma \varepsilon (T_w^4 - T_a^4) \pi d \, \delta x \end{aligned} \tag{1.5.1}$$

where on the left hand side there is the power produced by Joule effect. In the right hand side we find the power accumulated in the wire, the incoming power due to conduction, the power loss to convection, the outgoing power due to conduction and the irradiated power respectively.

The quantities in equation (1.5.1) are: I current intensity in the wire, R_w wire resistance, ρ_w wire density, c_w wire specific heat, T_w heated wire temperature, k_w wire thermal conductivity, h convective heat transfer coefficient, T_a fluid ambient temperature, σ Stephan-Boltzmann constant and ε emissivity of the wire.

This can be simplified neglecting radiation (Højstrup 1976), to give the general hot-wire equation:

$$K_1 \frac{\partial T_w}{\partial t} = \frac{\partial^2 T_w}{\partial x^2} - \beta_1 T_w + K_2 T_a - K_3 \quad . \tag{1.5.2}$$

The constants are given by:

$$K_1 = \frac{\rho_w c_w}{k_w} \tag{1.5.3}$$

$$\beta_1 = \frac{h \pi d}{k_w A} - \frac{\alpha I^2 \rho_w}{k_w A^2} \tag{1.5.4}$$

$$K_2 = \frac{h \pi d}{k_w A} \tag{1.5.5}$$

$$K_3 = \frac{I^2 \rho_w}{k_w A^2}(\alpha T_a - 1) \tag{1.5.6}$$

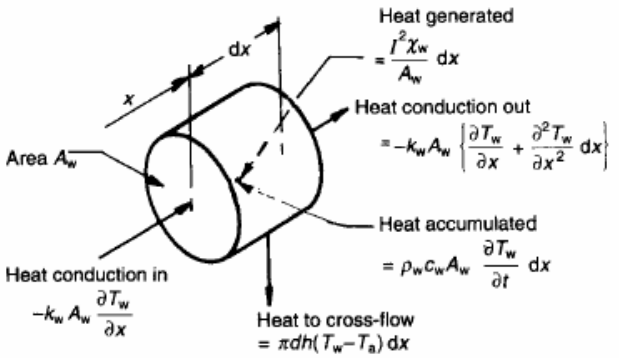

Figure 14: Heat balance for an infinitesimal element. (Bruun 1995)

The two main assumptions made in deriving equation (1.5.2) are that the radial variations in wire temperature and the radiation heat transfer are negligible: both of these will be justified briefly. The radiation term in equation (1.5.1) can be compared with any other term to assess its relative importance: the term chosen here is the convective heat loss term in equation (1.5.1), giving a ratio:

$$Ratio = \frac{\sigma \varepsilon}{h T_a}(T_w^4 - T_a^4) \quad . \tag{1.5.7}$$

Typical flow conditions over a typical hot wire give a ratio of 0.048 %.

The effects of radial variations are slightly more complex, but a simple case can be developed whereby the temperature is assumed to vary only in the radial direction. Performing a heat balance on the wire gives:

$$\frac{-I^2 \rho_w}{k_w A^2} = \frac{1}{r} \frac{\partial}{\partial r} \left(\frac{\partial T}{\partial r} \right) \tag{1.5.8}$$

If the change in resistivity with temperature is neglected, this yields the solution:

$$T_w(r) = const - \frac{I^2 \rho_w}{k_w A^2} \frac{r^2}{4} \quad , \tag{1.5.9}$$

where the constant is found from an energy balance at the surface. The maximum change across the wire as a ratio of the difference in temperature driving the heat transfer is then:

$$Ratio = \frac{1}{4} \frac{k}{k_w} Nu \quad , \tag{1.5.10}$$

where Nu is the Nusselt number, defined as $Nu = h d_w / k_w$, which is a non-dimensional parameter for the ratio between convectional and conductive heat exchange.

For typical conditions at stage exit, the ratio is 0.022 %. Since these two effects are clearly negligible, equation (1.5.2) can be used as the general hot wire equation.

Steady state solution

The general steady state solution to equation (1.5.2), assuming that $\bar{\beta}_1 > 0$, is found by applying the boundary condition and defining the mean wire temperature, denoted with an upper bar, along the axial coordinate of the wire x (see also Figure 14):

$$\bar{T}_w = \bar{T}_a \quad \text{at} \quad x = \pm 1 \quad , \tag{1.5.11}$$

$$T_m = \frac{1}{2l} \int_{-l}^{+l} \bar{T}_w \, dx \quad . \tag{1.5.12}$$

The non-dimensional steady state wire temperature distribution is then:

$$\frac{\bar{T}_w - \bar{T}_a}{T_m - \bar{T}_a} = \frac{\left[1 - \frac{\cosh\left(\sqrt{\bar{\beta}_1} x\right)}{\cosh\left(\sqrt{\bar{\beta}_1} l\right)} \right]}{\left[1 - \frac{1}{\left(\sqrt{\bar{\beta}_1} l\right)} \tanh\left(\sqrt{\bar{\beta}_1} l\right) \right]} \quad , \tag{1.5.13}$$

which is only a function of the Biot number $\sqrt{\bar{\beta}_1} l$ as seen in Figure 15.

A heat balance can then be performed over the whole wire, assuming that the flow conditions are uniform over the wire:

$$\bar{I}^2 R_w = \bar{H}_{cond} + \bar{H}_{conv} \quad . \tag{1.5.14}$$

The two heat transfer components can be found from the flow conditions and the wire temperature distribution:

$$\bar{H}_{conv} = 2 l \pi d \, \bar{h} \left(T_m - \bar{T}_a \right) \tag{1.5.15}$$

$$\bar{H}_{cond} = 2 k_w A \left| \frac{\partial \bar{T}_w}{\partial x} \right|_{x=l} \quad , \tag{1.5.16}$$

to give a steady state heat transfer equation:

$$\bar{I}^2 R_w = 2\pi \bar{h}_c d l (T_m - \bar{T}_a) \quad , \tag{1.5.17}$$

where the corrected heat transfer coefficient is given by:

$$\bar{h}_c = \bar{h} + \frac{d k_w}{4 l} \left(\frac{\sqrt{\bar{\beta}_1} \tanh(\sqrt{\bar{\beta}_1} l)}{1 - \dfrac{\tanh(\sqrt{\bar{\beta}_1} l)}{\sqrt{\bar{\beta}_1} l}} \right) \quad . \tag{1.5.18}$$

If the Biot number is larger than approximately 3, as is usually the case, in terms of Nusselt number this approximates to (Bradshaw 1971):

$$Nu_c = Nu + \frac{d}{2l} \sqrt{\frac{k_w}{k}} \sqrt{Nu} \tag{1.5.19}$$

giving the steady state calibration equation:

$$\bar{E}_w^2 = 2\pi k l R_w Nu_c (T_m - \bar{T}_a) \quad , \tag{1.5.20}$$

where the temperature dependent wire resistance is set by adjusting the current flow in the Wheatstone bridge. To reduce the proportion of heat transfer by conduction for given flow conditions the wire length to diameter ratio must thus be increased. Although the conduction end effect can be compensated out using equation (1.5.19), this is normally done automatically in the calibration. Equation (1.5.20) shows that the variations in the wire voltage are only dependent upon fluctuations in the Nusselt number and the temperature difference between the hot wire and the flow: both of these will now be examined.

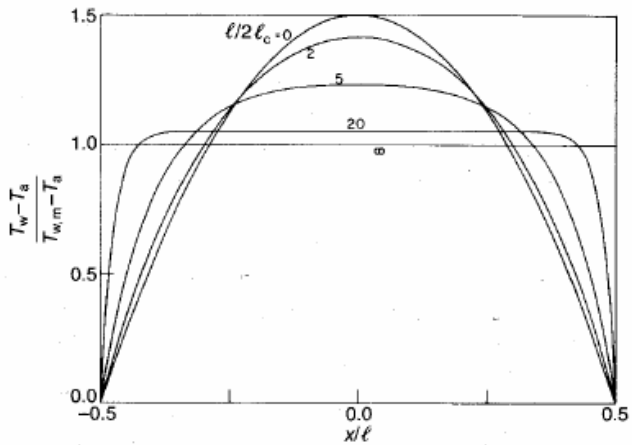

Figure 15: Steady state temperature distribution. (Freymuth 1979)

Nusselt number dependence

Due to the general engineering importance of heat transfer from a heated cylinder, the dependence of the Nusselt number on the flow conditions has been the subject of much research. The Nusselt number, as stated before, is a non-dimensional heat transfer coefficient, $Nu = h\,d\,/\,k$ which is the ratio of of the convective to the conductive heat transfer. The most general relationship states the dependence of Nu from several parameters (Bruun 1995):

$$Nu = Nu\left(\Re e\,,\, Pr\,,\, Kn\,,\, M\,,\, l/d\,,\, \Delta T\,/\,T_a\right) \quad , \tag{1.5.21}$$

where the Reynolds number $\Re e = Ud\,/\,\nu$, Mach number $M = U\,/\,a$ and Prandtl number $Pr = \nu/\alpha$ are defined using the kinematic viscosity of the fluid ν , the velocity of sound a, and the thermal diffusivity α . The Knudsen number $Kn = \lambda / d$ represents the ratio between the gas mean free path λ and the wire diameter. The influence of the wire length/diameter ratio is due to the conduction end effects. In principle it would be possible for a given hot-wire probe to find an expression for the Nusselt number in terms of the non-dimensional quantities in equation (1.5.21).

In practice, however, (keeping in mind that hot-wire probes are miniature devices) such a general relation would give large errors for small deviations. It is however possible to further simplify the above relation with some assumptions:

- incompressible flow (eliminates the Mach number dependence)
- standard density flow (eliminates the Knudsen number dependence)
- infinitely long wire (eliminates both l/d and $\Delta T\,/\,T_a$ dependence).

This idealised problem was solved by King (1914), resulting in King's law:

$$Nu = Nu\left(\Re e\,,\, Pr\right) = 1 + \sqrt{2}\,\pi\left(Pr\,\Re e\right)^{\frac{1}{2}} \quad . \tag{1.5.22}$$

For HWA applications this translates into:

$$E^2 = A + B\,U_{eff}^{n} \tag{1.5.23}$$

where A, B and n are variables dependent on several quantities listed in relation (1.5.21), and the effective cooling velocity U_{eff} is given by Jorgensen's equation:

$$U_{eff}^2 = U_n^2 + k_t^2 U_t^2 + k_s^2 U_s^2 \quad , \tag{1.5.24}$$

where in the reference system of a single wire U_n, U_t, U_s are respectively the normal, tangential and bi-normal velocity components; k_t, k_s are the yaw and pitch factors equal to ≈ 0.2 and ≈ 1 respectively.

For a given probe operated in a low Mach number flow the fluid properties are fairly constant and if additionally the temperature difference between the wire and the flow temperature is kept constant (this is known as constant temperature anemometry (CTA)) the variables A, B and n in equation (1.5.23) will loose their dependency on the mentioned dimensionless quantities.

Figure 16 shows a typically observed $Nu \approx \Re e^{0,5}$ (equivalent to $E^2 \approx U_{eff}^{0,5}$) functionality, which shows a fairly good constancy of the variables in equation (1.5.23) over a quite large Reynolds number range. The constants A, B and n are usually determined by means of a calibration against a known flow field.

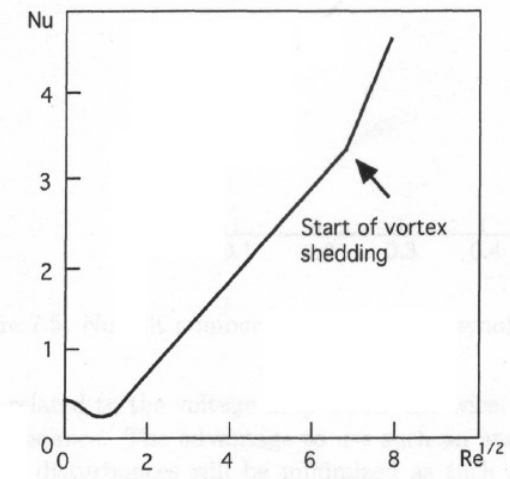

Figure 16: Nu as a function of Re for hot wire in air. (Alfredsson 2005)

Temperature dependence

The measured wire voltage is also dependent upon the temperature difference between the wire and the flow (1.5.21). Unless this temperature difference is measured or already known a measurement error will result, although this error can be minimised for small temperature fluctuations by operating the wire at a high temperature and calibrating the wire at the mean flow temperature. A means of compensation will otherwise be required: there are two main practical ways (Bruun 1995):

1. *Automatic compensation*: Use a temperature sensor in the Wheatstone bridge.

2. *Analytical correction*: Measure the flow temperature separately and compensate using the heat transfer equation.

Since automatic compensation has a bandwidth of approximately 100 Hz, analytical correction is the only means of compensation at most experimental frequencies, provided the possibility of having time-resolved temperature measurements.

Technique limitations

The features of hot-wire anemometry were already mentioned, namely its continuous signal and its ability to detect very fast fluctuations. If several hot-wires are placed close to each other or on the same probe two or three velocity components as well as velocity gradients can be measured instantaneously and simultaneously. But there are limitations to what can be measured. Most of the limitations can directly be derived from the assumptions made within this chapter. These assumptions begin to fail in very low velocity regions (where natural convection becomes important), separation regions (i.e. backflow, since hot-wires cannot distinguish between upward or downward cooling) or in very close vicinity of solid surfaces (since the heat sink represented by the surface is not taken into account by the calibration) .

1.6 Resolution effects in hot wire measurements

Accurate measurement of the statistics in a turbulent flow is important to further advance the fundamental knowledge in the field. To this day the study of resolution effects was mainly focused on turbulent boundary layers, where the small scale structures are small enough to appreciate the issue. Hot-wire anemometry (HWA) is the most popular experimental technique for turbulent boundary layer research, given its unsurpassed temporal and spatial resolution. A growing number of discrepancies reported in the literature by different groups of researchers led to the investigation on how the lack of resolution can affect measurements. The staple work in this field is the experimental investigation on spatial resolution by Ligrami & Bradshaw (1987), referred to from now on as LB87.

Even if in the present work turbulent boundary layers are not directly considered, similar effects to the ones reported in this chapter can potentially occur in other turbulent flows, such as the jet or the channel. It was deemed appropriate to report the latest results in resolution effects, but the actual impact on jet and channel flow measurements should be far less, because the turbulent structures are bigger than in the boundary layer.

Methodology

The spatial attenuation (filtering) caused by an idealized spanwise sensor is a function of the integral of the velocity fluctuations across the element. In turbulent flows these fluctuations are time dependent, and composed of multiple overlapping and interacting scales. The degree of attenuation on the single spanwise element is highly dependent on the spectral composition of turbulent fluctuations. Specifically one must consider the width of the energetic fluctuations compared to the spanwise length of the sensor element. This requires spectral information in the spanwise direction, which are today available only from direct numerical simulations (DNS).

In recent literature two different approaches to the problem are found. One is to collect many experimental data from previous works, involving different probe lengths, l/d ratios and Reynolds number, and extrapolate the filtering effect caused by these factors. The other is to consider a DNS of the flow and, from these “exact” data, investigate the effects of resolution by filtering the data according to different probe length.

Both approaches seem to lead to the same conclusions (Hutchins 2009), but the debate is still open on some issues. As an example of the effects of spatial resolution effects, we report the *near wall peak attenuation* and the *outer hump generation*.

Near wall peak attenuation

While a peak in the inner-scaled streamwise broadband turbulent energy $\langle u^{+2}\rangle \equiv \frac{\langle u^2\rangle}{u_\tau^2}$ is widely reported at a wall normal location $z^+ \equiv \frac{z\,u_\tau}{\nu} \approx 15 \pm 1$, the measured magnitude shows great dependence on non-dimensional wire length $l^+ \equiv \frac{l\,u_\tau}{\nu}$ and the friction Reynolds number.

A surface fit of the experimental data (see Figure 17), given by a non-linear least squares regression in the form of

$$\langle u^{+2}\rangle|_{peak} = A\log_{10} Re_\tau - Bl^+ - C\left(\frac{l^+}{Re_\tau}\right) + D \tag{1.6.1}$$

$$\begin{vmatrix} A & 1.0747 & B & 0.0352 \\ C & 23.0833 & D & 4.8371 \end{vmatrix}$$

shows the tendency of the magnitude of the peak to increase for increasing Reynolds number, and to decrease for increasing l^+. A separate study based on DNS confirms the tendency of magnitude attenuation due to increasing l^+ at a fixed Reynolds number (see Figure 18).

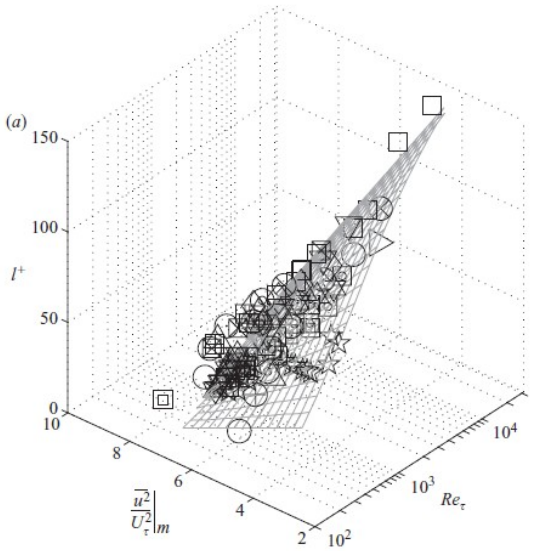

Figure 17: Variation of the peak value of the inner-scaled turbulence intensity with Re and l^+ for various experiments. Symbols refer to experiment considered. (Hutchins 2009)

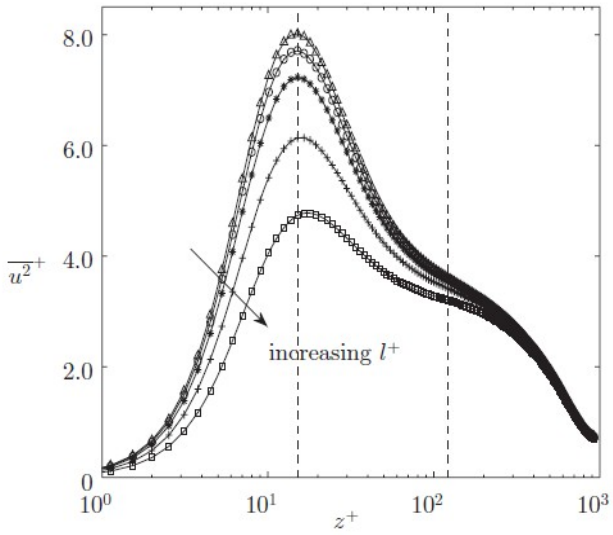

Figure 18: Comparison of streamwise turbulence intensity profiles for different filter lengths, $l^+ \approx 3.8$ (Δ), 11.5 (○), 19.1 (*), 34.3 (+) and 57.3 (□); arrow indicates increasing filter length (l^+), and the dashed lines are at $z^+ \approx 15$ and 120 ($z/\delta \approx 0.12$). (Hutchins 2009)

Relation (1.6.1) can be also used to validate one of the guidelines provided by LB87, which recommends to use wires of length $l^+ \leq 20$, asserting that "the turbulence intensity, flatness factor

and skewness factor of the longitudinal velocity fluctuations are nearly independent of wire length when the latter is less than 20-25 wall units". The percentage error predicted from (1.6.1) for a wire length $l^+ = 20$ compared to an ideal wire $(l^+ \to 0)$ is given by

$$|\%error|_{l^+=20} = 100 \times \frac{20(B + C/Re_\tau)}{A\log_{10} Re_\tau + D} \quad . \tag{1.6.2}$$

The absolute error given by the numerator of equation (1.6.2) tends to a constant value as Re increases, but the percentage error will fall indefinitely. This leads to the conclusion that the smaller l^+ can be, the better.

Outer hump generation

Consider profiles of streamwise turbulent intensity for several viscous scaled wire lengths and a fixed Reynolds number $Re_\tau \approx 14\,000$. As the wire length is increased we observe the fall in magnitude for the near wall peak (as described earlier), but also the rise of a secondary peak in the log region. If l^+ is further increased the near wall peak disappears, and the secondary peak begins to decrease it's magnitude as well (see Figure 19a). Note that the mean velocity profiles show no dependence on wire length (see Figure 19b).

One can decompose the fluctuating velocity signal in small scale $(\lambda_x^+ < 7000)$ an large scale $(\lambda_x^+ > 7000)$ contributions, where λ_x^+ is the streamwise wave length of Fourier decomposed fluctuations defined as $\lambda_x^+ \equiv 2\pi/k_x$ (k_x is the streamwise wave number) (Hutchins & Marusic, 2007). Looking at the decomposed broadband turbulence intensity (see Figure 20), one can note that the small scale contribution is located near the wall and decreases with increasing wire length, while the large scale contribution is located mainly in the log region and is not affected by wire length. Thus as the wire length increases we are increasingly measuring only the large scale contribution to the broadband intensity.

Further studies reveal that up to friction Re = 18830 there is no outer hump for spatially well resolved measurements, so this phenomena is due to resolution issues only (at least up to that Re).

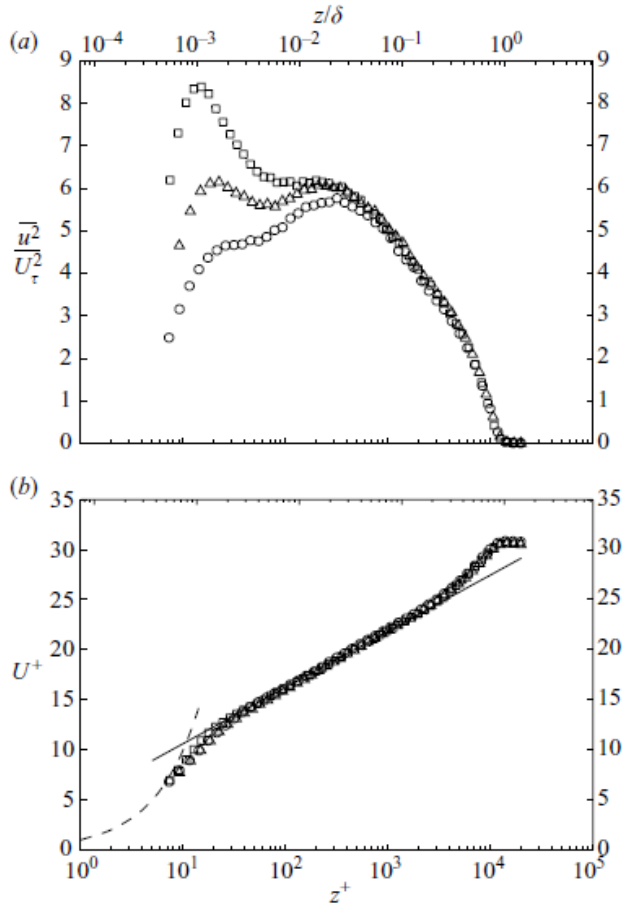

Figure 19: (a) Broadband turbulence intensity profiles at Re=14000 using three wire lengths. (b) Associated mean velocity profiles:□, l^+=22; Δ, l^+=79; ○, l^+=153. (Hutchins 2009)

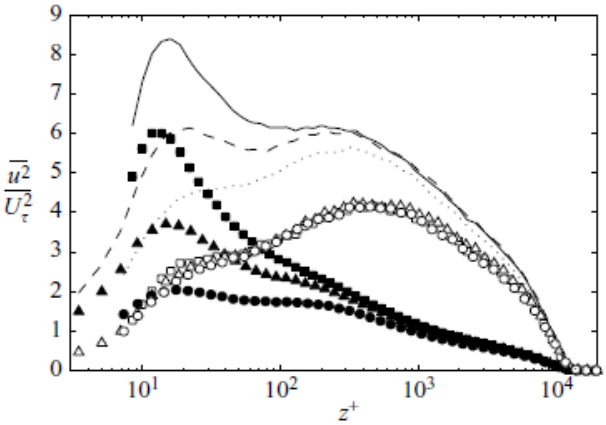

Figure 20: Turbulence intensity profiles decomposed into small scale (solid symbols) and large scale (open symbols) contributions. The symbols are as in figure 3. The lines show the broadband turbulence intensity for l^+=22 (solid line), l^+=79 (dashed line), l^+=153 (dotted line). (Hutchins 2009)

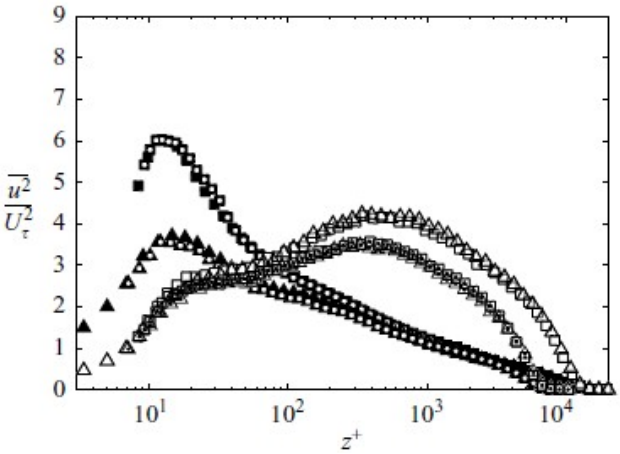

Figure 21: Turbulence intensity profiles decomposed into small scale (solid symbols) and large scale (open symbols) for two different friction Reynolds numbers. Re=7300 (dotted symbols), Re=14000 (plain symbols). Triangular symbols for l^+=79, squared symbols for l^+=22. (Hutchins 2009)

A more in depth look at the decomposed turbulence intensity profiles (see Figure 21), reveals that small scales are affected by wire length only, while large scales are affected by Reynolds number only.

Temporal resolution

Temporal and spatial resolution requirements are related through Taylor's hypothesis. To avoid attenuation the overall temporal resolution of the measurement system must be fast enough to resolve a structure of a given streamwise length as it travels past the sensor. This means that in fast, high Reynolds number flows, the temporal resolution has to be increased, as the convection velocity increases and the size of the smallest structures decreases.

After defining a viscous time scale as

$$t^+ \equiv \frac{t\,u_\tau^2}{\nu} = \frac{\lambda_x^+}{u^+} \tag{1.6.3}$$

it can be shown (Hutchins 2009) that turbulent fluctuations are well resolved for $t^+ \approx 3$, thus establishing a maximum flow frequency for boundary layer measurements in the form of

$$f_c \geq \frac{u_\tau^2}{3\nu} \quad . \tag{1.6.4}$$

This clearly poses a limit to the reachable Reynolds number using commercial systems that usually can provide measurements in the range $30 < f_a < 100$ kHz.

Guidelines for hot wire measurements

To isolate as much as possible the effects of spatial and temporal filtering, as well as heat loss to the supports, we can define three guidelines for “accurate” measurements:

1. l^+ should be as small as possible. When comparing data at different l^+ some attempts at compensation for the error should be made. Provided $l^+ < 20$, the error on turbulence intensity peak should be less that 10% at friction Re > 3000.

2. $t^+ < 3$. The highest frequency information will increase as u_τ^2 . It's necessary to ensure that all experimental apparatus can resolve these time scales.

3. l/d > 200. The errors due to heat loss to the supports are not related to lack of spatial resolution, but can be severe. These specification follows the one in LB87, and seems to be still valid according to more recent studies.

2. Numerical and Experimental set-up

2.1 Experimental Set-up for the turbulent jet flow

The experiments were carried out in the *Coaxial Aerodynamic Tunnel* facility (CAT) located in the laboratory of the *Second Faculty of Engineering,* Forlì. This facility was designed by Buresti (2000) and further developed by Burattini (2002) at the department of Aerospace Engineering of the University of Pisa (DIA), and was sent to the University of Bologna as part of a cooperation between the two departments. The CAT can be used for mixing layers studies as it consists of two coaxial top-hat jets. However for the purposes of the current study on a simple round jet, only the inner jet was used.

The facility, schematically presented in Figure 22, is composed of two independent centrifugal blowers driven by three phase electrical motors (A & B) whose speed is controlled by two electrical inverters. To reduce disturbances from the fans there are two pre-settling chambers (C & D) just downstream from the blowers. Further downstream are located the settling chambers (D & E) for the inner and outer jet respectively. Flow conditioning is performed by three screens and a honeycomb in the inner jet, as well as five screens and a honeycomb in the outer jet (H). The contraction rates are 11:1 and 16,5:1 for the inner and outer jet respectively. Both nozzles (D_o = 100 mm, D_i = 50 mm) end with a 100 mm straight pipe.

The experimental facility is placed in a large laboratory and the exit of the jets located as far as possible from any kind of obstacle, with the goal of resembling a jet in an infinite environment.

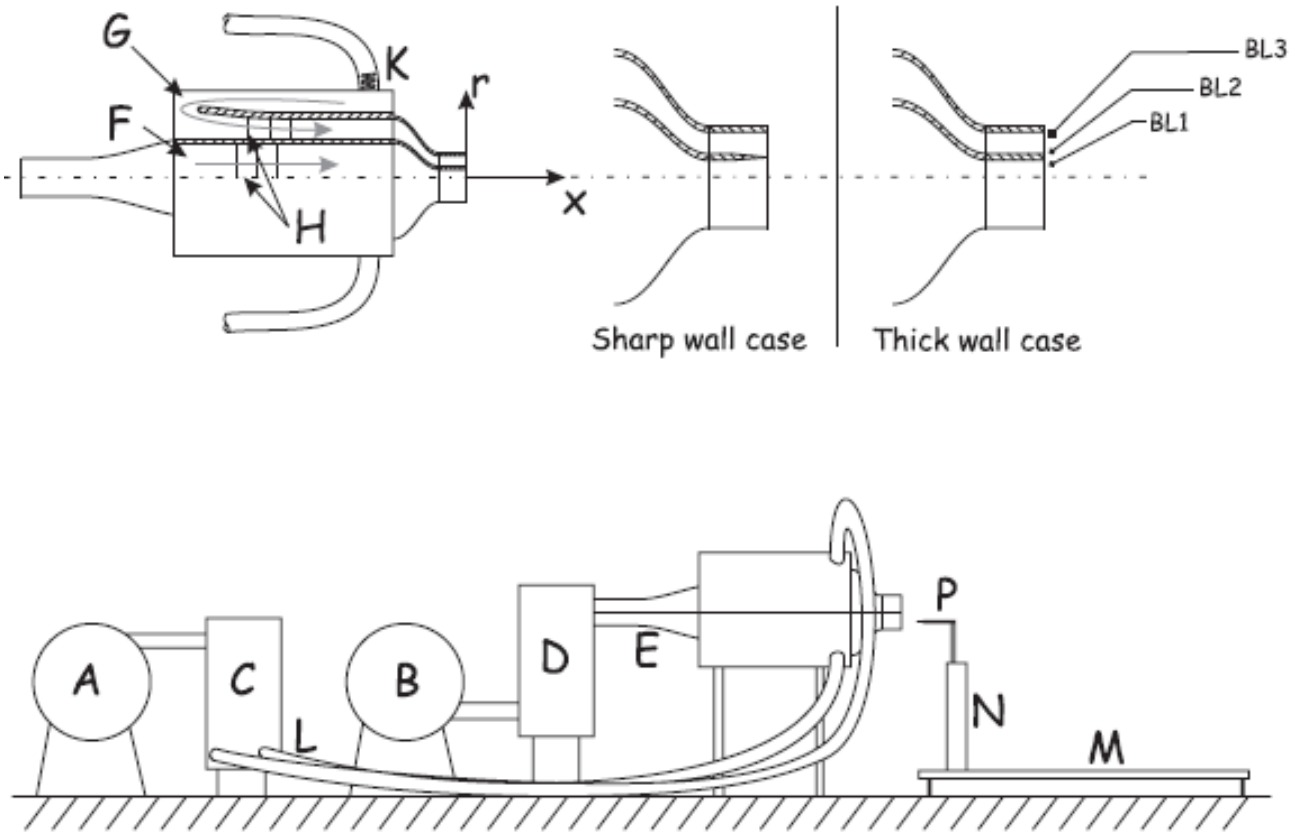

Figure 22: Schematic of the Coaxial Air Tunnel (CAT) facility: A) outer jet blower, B)inner jet blower, C) outer jet pre-settling chamber, D) inner jet pre-settling chamber, E) inner jet diffuser, F) outer jet settling chamber, G) inner jet settling chamber, H) screens and honeycombs, J) outer jet hoses, K) close-up of the jet exit with the thick separating wall, L) axial traversing, M) heat gun, and N) radial traversing.

Due to the axial symmetry of this set-up, a cylindrical set of coordinates (x, r, θ) was selected, with the corresponding velocity being (u, v, w) to indicate axial, radial and azimuthal components. The azimuthal velocity at the exit was characterised by Burattini (2002) and found to be negligible.

The hot-wire probes (P) are positioned in the flow by means of a motorized traversing system, capable of moving the probe in the axial (M) and radial (N) directions. The traversing system is digitally operated through a PC using a NI BCN 6221 board, while the jet speed is manually adjusted with the inverter.

Before any measurement could be carried out, the CAT had to be aligned with the traversing system. This alignment, achieved with the aid of a laser light, is however geometrical only. The real jet axis is in general influenced by the surroundings and, given the degrees of freedom of the traversing, can be isolated only in the radial direction.

Measurement techniques

As previously explained in section (1.6), hot-wire anemometry was the technique of choice to carry out the measurements. For the present set of results, two different probes were specifically produced in-house. The data was then acquired by means of a DANTEC *StreamLine* 90N10 Frame with two 90C10 *Constant Temperature Anemometers* (CTA) modules connected to a NI BCN 6221 acquisition card.

The probes

Commercial hot-wire probes are usually made out of tungsten and have at least a length of 1 mm and a diameter of 5 μm, assuring relatively good mechanical strength to the product. The size of this probes however becomes a problem when investigating small scale turbulence, since the filtering effects greatly interfere with the measurement.

Both the probes used in the experiment were hand-made in our laboratory following the procedure described in Fiorini (2012), to better fit the requirements imposed by filtering and heat loss toward the prongs (see). In order to maintain a l/d ratio of ≈ 200, the wires mounted are ≈ 500 μm long and have a ≈ 1,25 μm diameter. Since tungsten wires are not available in those sizes, platinum wires made with the Wollastone process were used instead. Those wires are secured in position between the prongs via *soft-soldering*, the solder material being a Sn60Pb40 alloy.

The types of probe produced are a *Double-Wire* (DW) and an *X-Wire* (XW), as in Figure 23. The first allows the estimate of partial spatial derivatives in r and θ for the axial velocity, the latter allows the estimate of the radial and azimuthal velocities.

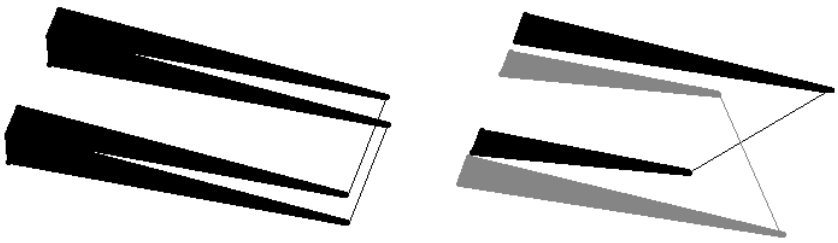

Figure 23: Schematic example of Double-Wire (left) and X-Wire (right).

Sampling frequency and time

All hot-wire measurements (aside from calibration) are carried out with a sampling frequency of 20kHz and a low pass filter (LPF) set at 10kHz to ensure good resolution and avoid aliasing problems. The sampling time was selected to be 120 seconds, high enough to resolve statistical moments with satisfactory accuracy, but not too long in order to retain calibration until the end of the measurement (each radial sweep takes about 45 minutes). The estimated error for the mean is given by

$$\varepsilon=\sqrt{\left(\frac{2\Lambda}{T}\right)}\frac{u_{rms}}{\overline{u}}\approx 0{,}01 \quad , \tag{2.1.1}$$

while the error on the variance is

$$\varepsilon=\sqrt{\left(\frac{2\Lambda}{T}(F-1)\right)}\approx 0{,}06 \quad . \tag{2.1.2}$$

Both the integral time scale $\Lambda\equiv(x-x_0)/U_{cl}$ and the flatness $F\equiv(\overline{u^4})/(\overline{u^2})^2$ were calculated from preliminary results.

Calibration

In order to relate the voltages acquired with the hot-wire to real velocities, calibration is necessary before each sets of measurements. The procedure for the DW and the XW are rather different, hence described in different paragraphs. In both instances the mean flow velocity is determined with a Prandtl tube (external diameter = 2 mm, internal diameter = 1 mm) connected to a differential pressure transducer SETRA239 0-5 water inches.

Double wire calibration

A fourth order polynomial relation for each wire has been used to convert the voltage into the velocity:

$$\begin{aligned} U_{wire\,1}&=a_{01}+a_{11}E_1+a_{21}E_1^2+a_{31}E_1^3+a_{41}E_1^4 \\ U_{wire\,2}&=a_{02}+a_{12}E_2+a_{22}E_2^2+a_{32}E_2^3+a_{42}E_2^4 \end{aligned} \tag{2.1.3}$$

This method does not take into account any thermal corrections like King's Law, but gives a better fit while retaining a simple implementation (Bruun 1995). On the other hand this method is far from the cooling laws of the wire and cannot reliably extrapolate data outside the calibration range.

For each calibration a velocity sweep was performed after having positioned both the Prandtl tube and the DW in the potential core of the jet. A sample output of this procedure is given in Figure 24.

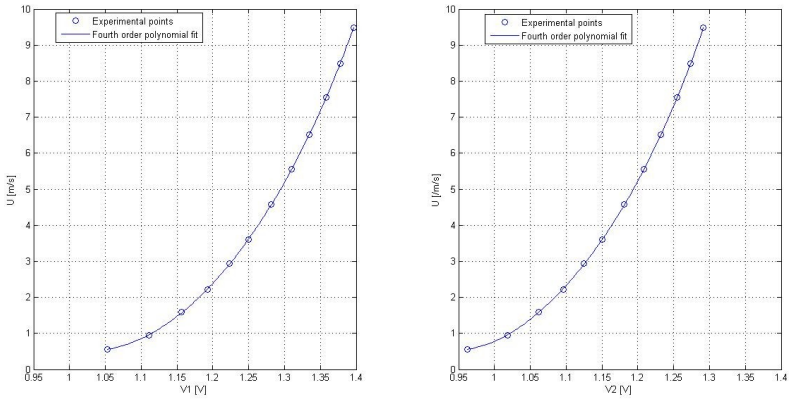

Figure 24: Example calibration curves for a Double-Wire. Wire 1 (left) and Wire 2 (right) have a different response.

X wire calibration

To calibrate the XW one has to install on the jet nozzle a graduated device capable of exposing the probe at different angles with respect to the flow (Errore: sorgente del riferimento non trovata). Ideally one would like to position the Prandtl tube alongside the XW, like in the DW case. Unfortunately this is not possible because the device mounted at the nozzle takes up too much space already.

The flow velocity is instead determined from a fourth order polynomial fit obtained with another calibration, which this time relates the engine frequency to the output velocity in the jet's potential core. This relation was found to be very stable and accurate, with errors under 1% (Figure 25).

For each XW calibration a map of points for various velocities and angles was obtained (Figure 26), and a polynomial fit of fifth order was calculated separately for the velocities and the angles. The fitting error in the velocity map was found to be small (around 1%), while the fitting error in the angle map was sometimes very high.

This prompted the removal of measured voltages outside of the calibration map during the acquisition of data, in order to avoid false readings on the velocity and angle. The percentage of samples removed from a time series is shown in Figure 27.

The amount of samples removed is negligible on the centreline, but becomes high when approaching the outskirts of the jet. Note that the removal of a single point here causes the inability to calculate two derivatives (since we use a simple finite difference scheme of first order for that). It was however noticed that while this filtering helps in obtaining smoother statistics, it does not alter significantly their qualitative behaviour.

Reynolds number and distance from the nozzle

As previously stated, the turbulent jet becomes self-similar for large enough Re and downstream position. Since we want to measure a turbulent flow in the self-similar region, a $\Re e = U_J D / \nu = 70'000$ was selected, along with a downstream position of x/D=30. The downstream position is measured starting from the virtual origin of the jet, which for our facility stands 125mm inside the nozzle.

Each of the 4 total experiments involves a sweep of the jet radius, starting from the centreline and moving upwards in steps of 15mm, to collect a total of 18 measure points.

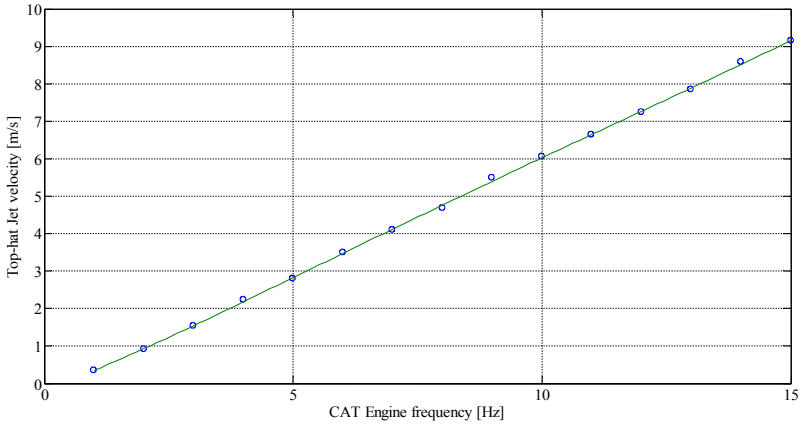

Figure 25: Relation between engine frequency and top-hat velocity at the nozzle for the CAT.

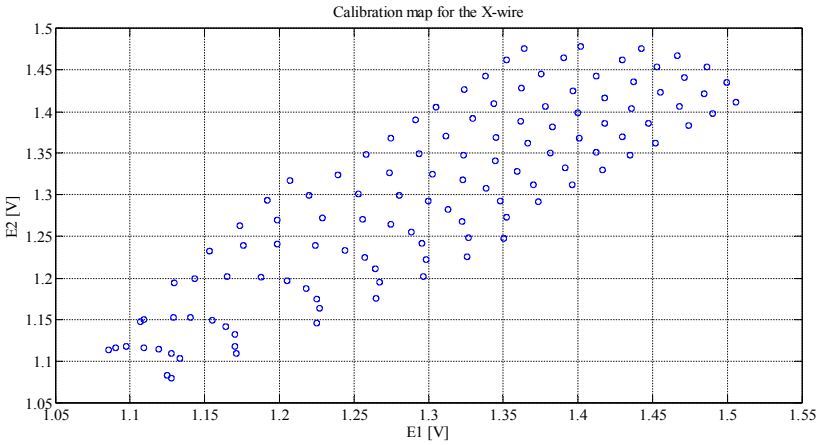

Figure 26: Calibration map for the X-Wire.

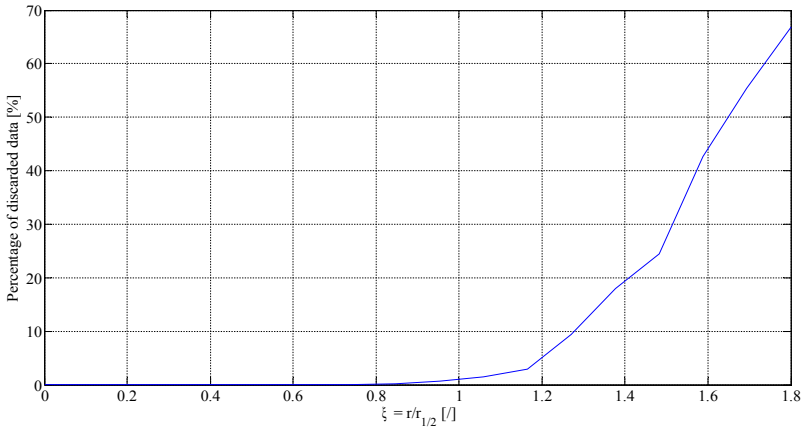

Figure 27: Percentage of points out of the calibration map during an acquisition with an X-Wire.

2.2 Numerical Set-up for the turbulent jet flow

The laboratory experiments mentioned above involve an actual spatial development of a turbulent jet issuing from a nozzle into an ideally infinite environment filled with the same fluid. Computing such flow accurately, so that all the relevant length and time scales are captured, can be extremely demanding on both computer time and memory. Therefore it was decided to compute a temporal analogue of the problem, where one studies the time evolution of a cylindrical mixing layer inside a computational domain which is periodic in all three spatial dimensions.

The advantage of using a periodic domain is that spectral methods based on the Fast Fourier Transform (FFT) can be used to compute the flow reasonably fast and with high accuracy. It's important, however, to note that the periodic boundary conditions produce a flow that, while not identical to the spatially evolving jet, closely resembles it. Thus, although we capture three dimensional structures of the kind known to occur in a laboratory jet, such events as ring formation and pairing now occur over the temporal evolution of the flow, and not in a particular region of the space. The calculations are therefore not strictly representative of the evolution of either an axisymmetrical jet or a wake but of a cylindrical (or tubular) mixing layer.

The simulation set-up was taken from Basu & Narashima (1999), since it was not in the goals of this thesis. All the post-processing of the results was however independently carried out given the very specific nature of the quantities to study.

Governing equations

The flow is considered to be nearly incompressible, since the Mach number of the simulation is extremely small and therefore all density changes are neglected. Equations (2.2.1) and (2.2.2) respectively express the conservation of mass and momentum, where **u** is the velocity vector, ρ the density of the fluid, p the pressure, ν the kinematic viscosity.

$$\nabla \cdot \boldsymbol{u} = 0 \tag{2.2.1}$$

$$\frac{\partial \boldsymbol{u}}{\partial t} + (\boldsymbol{u} \cdot \nabla)\boldsymbol{u} = -\frac{1}{\rho}\nabla p + \nu \nabla^2 \boldsymbol{u} \tag{2.2.2}$$

These equations are rewritten in a non-dimensional way before solving, using as a scale the initial diameter d_0, the initial centreline velocity U_0 and a reference temperature T_0.

Denoting the now non-dimensional variables with an asterisk, we get:

$$\nabla \cdot \boldsymbol{u}^* = 0 \tag{2.2.3}$$

$$\frac{\partial \boldsymbol{u}^*}{\partial t^*} + (\boldsymbol{u}^* \cdot \nabla^*)\boldsymbol{u}^* = -\nabla^* p^* + \frac{1}{\Re e}\nabla^{*2}\boldsymbol{u}^* \tag{2.2.4}$$

Initial and boundary conditions

The equations (2.2.3), (2.2.4) and (2.2.8) are solved in a Cartesian coordinate system $\boldsymbol{x} = (x, y, z) = (x_1, x_2, x_3)$. However in order to facilitate the description of initial conditions relevant to the (temporally evolving) jet, we shall also use a cylindrical coordinate system (x, r, θ) such that

$$\begin{aligned} x &= x \\ y &= r \cos(\theta) \\ z &= r \sin(\theta) \end{aligned} \quad . \tag{2.2.5}$$

The corresponding velocity components are (u, v, w) and (u, u_r, u_θ) in the Cartesian and cylindrical coordinate system respectively.

The initial conditions are chose to simulate a flow that is similar (in temporal sense) to a jet issuing from a round nozzle. Thus we have a tubular shear layer along the x direction at time t = 0. The streamwise x velocity has a top-hat profile with a tan hyperbolic shear layer:

$$\begin{aligned} u &= 1, && \forall\, r \le r_0 - \delta/2 \\ &= 0, && \forall\, r \ge r_0 + \delta/2 \\ &= \frac{1}{2}\left(1 - \tanh\left(\frac{r - r_0}{2\theta_0}\right)\right), && \forall\, r_0 - \delta/2 < r < r_0 + \delta/2 \end{aligned} \tag{2.2.6}$$

where δ is the characteristic width of the shear layer. Here r_0 is the initial radius of the shear layer, θ_0 is the initial momentum thickness and u_0 and u_r are assumed to be zero everywhere. A small random perturbation is imposed on the shear layer corresponding to an increment in u_r.

Even though our focus in this study is primarily on the late times after the jet has developed self-similarity, we nevertheless compute through the instability and transition phases of the jet; this approach has been taken here because it is difficult to prescribe an `initial' far-field condition that contains the representative vortical structures which are so essential to the points being made here. The boundary conditions are taken to be periodic in each space direction for all primary variables (this facilitates the use of Fourier spectral schemes, and hence FFTs). The computational domain is a periodic cubical box of dimension 4 x 4 x 4, resolved with 192 Fourier modes for each side. The size of the radius of the tubular shear layer is initially 1.

Method of solution

Equation (2.2.4) is solved along with the continuity equation (2.2.3) in a Cartesian coordinate system using the Fourier Galerkin (spectral) technique. The basic philosophy of the scheme is similar to that of Orszag (1971) for direct solution of the incompressible Navier Stokes equations.

The periodic boundary conditions are automatically satisfied by choosing a Fourier spectral representation. For integrating in time, we use a third-order-accurate Runge Kutta scheme for the non-linear terms, coupled with a third-order-accurate Adams Bashforth scheme for the linear terms.

The programming language of choice is Fortran, operated on a Unix based system, to give the maximum performance possible to the calculation. However the short amount of time available forced us to evolve only 2 configurations with different initial disturbs. As a consequence the statistical convergence is not complete.

Numerical Post-processing

The result of the simulation is the complete velocity field in the computational box for all the times in the temporal evolution. In order to make a comparison with the experimental results, we are interested in calculating the total dissipation and some of it's components in a cylindrical system of reference. We start by calculating the velocity gradient in the Fourier space, starting from the velocity field (which is also in the Fourier space). At this point the velocity field and the velocity gradient are taken into the physical space with an inverse FFT, obtaining these quantities in the Cartesian coordinates. A polynomial interpolation is performed to obtain the fields in a cylindrical grid, starting from the Cartesian grid.

At this point we use the velocity gradient in Cartesian formulation (but on the cylindrical grid) to obtain it's corresponding version in cylindrical coordinates as follows.

Consider a vector quantity **F** in a three dimensional space (which in our case represents the velocity vector). This quantity can be written in Cartesian coordinates as

$$\boldsymbol{F} = \begin{pmatrix} F_1 \\ F_2 \\ F_3 \end{pmatrix} (x, y, z) \quad , \tag{2.2.7}$$

and in the cylindrical coordinate system as

$$\tilde{\boldsymbol{F}} = \begin{pmatrix} F_x \\ F_r \\ F_\theta \end{pmatrix} (x, r, \theta) \quad . \tag{2.2.8}$$

Beside the obvious relation (2.2.5), one can state the relation between the vector components in the two different coordinate systems:

$$\begin{aligned} F_x &= F_1 \\ F_r &= F_2\cos(\theta)+F_3\sin(\theta) \\ F_\theta &= -F_2\sin(\theta)+F_3\cos(\theta) \end{aligned} \quad . \tag{2.2.9}$$

The partial derivatives in the cylindrical coordinate system can be generally expressed as a function of the derivatives in the Cartesian coordinate system using the chain rule of derivation:

$$\begin{aligned} \frac{\partial}{\partial x}(\tilde{\boldsymbol{F}}) &= \frac{\partial}{\partial x}(\boldsymbol{F}) \\ \frac{\partial}{\partial r}(\tilde{\boldsymbol{F}}) &= \frac{\partial y}{\partial r}\frac{\partial}{\partial y}(\boldsymbol{F})+\frac{\partial z}{\partial r}\frac{\partial}{\partial z}(\boldsymbol{F}) \\ \frac{\partial}{\partial \theta}(\tilde{\boldsymbol{F}}) &= \frac{\partial y}{\partial \theta}\frac{\partial}{\partial y}(\boldsymbol{F})+\frac{\partial z}{\partial \theta}\frac{\partial}{\partial z}(\boldsymbol{F}) \end{aligned} \quad , \tag{2.2.10}$$

which, using relation (2.2.5), leads to

$$\begin{aligned} \frac{\partial}{\partial x}(\tilde{\boldsymbol{F}}) &= \frac{\partial}{\partial x}(\boldsymbol{F}) \\ \frac{\partial}{\partial r}(\tilde{\boldsymbol{F}}) &= \frac{\partial}{\partial y}(\boldsymbol{F})\cos(\theta)+\frac{\partial}{\partial z}(\boldsymbol{F})\sin(\theta) \\ \frac{\partial}{\partial \theta}(\tilde{\boldsymbol{F}}) &= -\frac{\partial}{\partial y}(\boldsymbol{F})r\sin(\theta)+\frac{\partial}{\partial z}(\boldsymbol{F})r\cos(\theta) \end{aligned} \quad . \tag{2.2.11}$$

To obtain the full velocity gradient tensor in cylindrical coordinates one must apply relation (2.2.11) to each component of $\tilde{\boldsymbol{F}}$ in combination with (2.2.9):

$$\begin{aligned} \frac{\partial F_x}{\partial x} &= \frac{\partial F_1}{\partial x} \\ \frac{\partial F_x}{\partial r} &= \cos(\theta)\frac{\partial F_x}{\partial y}+\sin(\theta)\frac{\partial F_x}{\partial z} \\ &= \cos(\theta)\frac{\partial F_1}{\partial y}+\sin(\theta)\frac{\partial F_1}{\partial z} \\ \frac{1}{r}\frac{\partial F_x}{\partial \theta} &= -\sin(\theta)\frac{\partial F_x}{\partial y}+\cos(\theta)\frac{\partial F_x}{\partial z} \\ &= -\sin(\theta)\frac{\partial F_1}{\partial y}+\cos(\theta)\frac{\partial F_1}{\partial z} \end{aligned} \tag{2.2.12}$$

$$
\begin{aligned}
\frac{\partial F_r}{\partial x} &= \cos(\theta)\frac{\partial F_2}{\partial x}+\sin(\theta)\frac{\partial F_3}{\partial x} \\
\frac{\partial F_r}{\partial r} &= \cos(\theta)\frac{\partial F_r}{\partial y}+\sin(\theta)\frac{\partial F_r}{\partial z} \\
&= \cos^2(\theta)\frac{\partial F_2}{\partial y}+\sin^2(\theta)\frac{\partial F_3}{\partial z}+\cos(\theta)\sin(\theta)\left[\frac{\partial F_3}{\partial y}+\frac{\partial F_2}{\partial z}\right] \\
\frac{1}{r}\frac{\partial F_r}{\partial \theta} &= -\sin(\theta)\frac{\partial F_r}{\partial y}+\cos(\theta)\frac{\partial F_r}{\partial z} \\
&= \cos^2(\theta)\frac{\partial F_2}{\partial z}-\sin^2(\theta)\frac{\partial F_3}{\partial y}+\cos(\theta)\sin(\theta)\left[\frac{\partial F_3}{\partial z}-\frac{\partial F_2}{\partial y}\right]
\end{aligned}
\tag{2.2.13}
$$

$$
\begin{aligned}
\frac{\partial F_\theta}{\partial x} &= -\sin(\theta)\frac{\partial F_2}{\partial x}+\cos(\theta)\frac{\partial F_3}{\partial x} \\
\frac{\partial F_\theta}{\partial r} &= \cos(\theta)\frac{\partial F_\theta}{\partial y}+\sin(\theta)\frac{\partial F_\theta}{\partial z} \\
&= \cos^2(\theta)\frac{\partial F_3}{\partial y}-\sin^2(\theta)\frac{\partial F_2}{\partial z}+\cos(\theta)\sin(\theta)\left[\frac{\partial F_3}{\partial z}-\frac{\partial F_2}{\partial y}\right] \\
\frac{1}{r}\frac{\partial F_\theta}{\partial \theta} &= -\sin(\theta)\frac{\partial F_\theta}{\partial y}+\cos(\theta)\frac{\partial F_\theta}{\partial z} \\
&= \cos^2(\theta)\frac{\partial F_3}{\partial z}+\sin^2(\theta)\frac{\partial F_2}{\partial y}-\cos(\theta)\sin(\theta)\left[\frac{\partial F_3}{\partial y}+\frac{\partial F_2}{\partial z}\right]
\end{aligned}
\tag{2.2.14}
$$

Relations (2.2.12), (2.2.13) and (2.2.14) make up the entire velocity gradient in cylindrical coordinates as a function of the velocity gradient in Cartesian coordinates. Simply substitute the velocity vector **u** to the generic vector field **F** and the result is obtained:

$$
\left[\begin{array}{ccc}
\frac{\partial u}{\partial x} & \frac{\partial u_r}{\partial x} & \frac{\partial u_\theta}{\partial x} \\
\frac{\partial u}{\partial r} & \frac{\partial u_r}{\partial r} & \frac{\partial u_\theta}{\partial r} \\
\frac{1}{r}\frac{\partial u}{\partial \theta} & \frac{1}{r}\frac{\partial u_r}{\partial \theta} & \frac{1}{r}\frac{\partial u_\theta}{\partial \theta}
\end{array}\right](x, r, \theta)
\tag{2.2.15}
$$

Having all the terms in (2.2.15) at disposal, it's possible to calculate the dissipation using for example relation (1.2.19).

Keep in mind that to resemble a spatial average with a temporal jet we have to run several simulations with a slightly different initial disturb, and evolve them to a big enough time so that the corresponding space is in the self-similar region (usually t > 20).

2.3 Numerical Set-up for the turbulent channel flow

The dataset considered is the result of a direct numerical simulation of a turbulent channel flow (see Figure 28) by Cimarelli &De Angelis (2011) at a friction Reynolds number $\Re e_\tau = u_\tau h/\nu = 298$ where, u_τ is the friction velocity, ν the kinematic viscosity and h the half channel height.

The computation, carried out with a pseudo-spectral code, was cut after 500 large eddy turnover times, defined as $T = h/U_c$ where U_c is the centreline velocity. To be relevant, the statistics have been evaluated averaging over 100 different initial configurations.

Further details about the numerical scheme adopted are far beyond the purposes of the present work, and can be found in Lundblah, Henningson & Johansson (1992).

The computational domain is $2\pi h \cdot 2h \cdot \pi h$ with 512x193x265 grid points respectively, corresponding in a resolution, in non-dimensional wall units along the homogeneous directions, of $\Delta x^+ = \Delta z^+ = 3{,}64$. This resolution, higher than usual for a turbulent channel flow, was adopted at the expense of the achievable Reynolds number to appreciate the phenomena and the dynamics of the velocity field up to the dissipative scale. For more details about the single point statistics in this dataset, see Saikrishnan (2011).

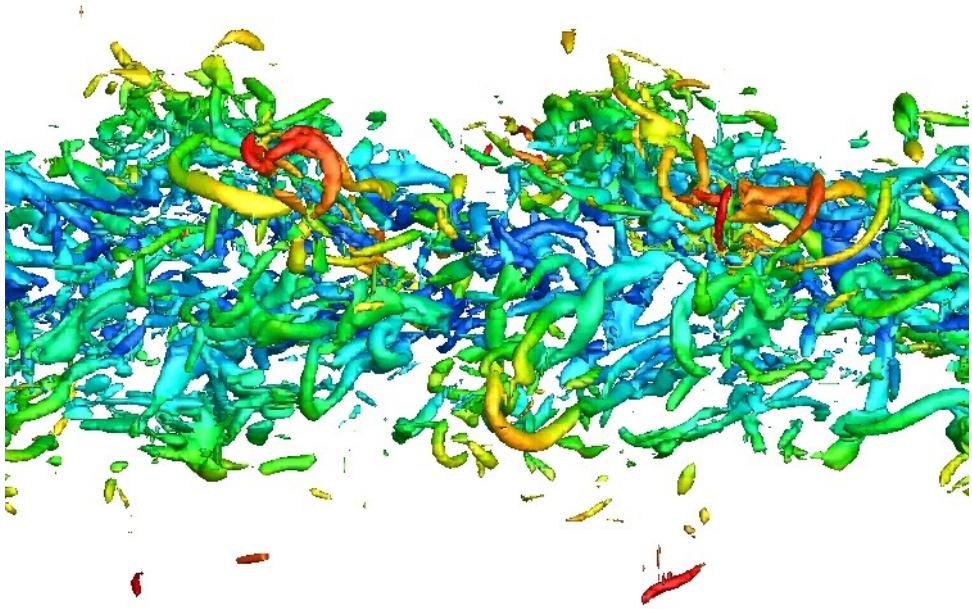

Figure 28: Turbulent structures in a channel flow, DNS at Re=298 (Cimarelli & De Angelis, 2011).

3. Results

Here the results, both numerical and experimental, are presented for the channel and the jet flow respectively. The results are then commented upon, and an attempt at explaining the discrepancies with the expected results is made.

3.1 Numerical results for the turbulent channel flow

Since in the case of a turbulent channel flow we do not have access to any experimental data, only the DNS data will be presented. As previously stated, the main investigation of this work is devoted to turbulent kinetic energy dissipation, which can be computed from DNS data in it's complete formulation (also referred to as *true dissipation*) as in (1.2.16). Here, for comparison purposes only, we report the curve for the classic surrogate of dissipation in channel flows, which is (1.2.21).

To better approximate the true dissipation along the channel height two new surrogates are proposed, based on the terms eventually measurable with a Double-wire and an X-wire. They are respectively the *short* and *long* surrogates, formulated as

$$\varepsilon_{short} \equiv A\left\langle\left(\frac{\partial u}{\partial x}\right)^2\right\rangle + B\left\langle\left(\frac{\partial u}{\partial y}\right)^2\right\rangle \quad , \tag{3.1.1}$$

$$\varepsilon_{long} \equiv C\left\langle\left(\frac{\partial u}{\partial x}\right)^2\right\rangle + D\left\langle\left(\frac{\partial u}{\partial y}\right)^2\right\rangle + E\left\langle\left(\frac{\partial v}{\partial x}\right)^2\right\rangle + F\left\langle\left(\frac{\partial w}{\partial x}\right)^2\right\rangle \quad . \tag{3.1.2}$$

The constant coefficients are obtained from the true dissipation values with a least squares method, resulting in the following table:

Short surrogate (3.1.1)		Long surrogate (3.1.2)			
A	B	C	D	E	F
9,1975	0,6440	14,1818	0,6351	3,7345	-7,9463

From the DNS data we compute the dissipation as a function of the channel height position only, taking the mean along xz planes and in time.

In Figure 29 the curves for true dissipation, traditional surrogate and proposed surrogates are reported. In Figure 30 the error for each dissipation surrogate, compared to the true dissipation, is plotted along the channel height.

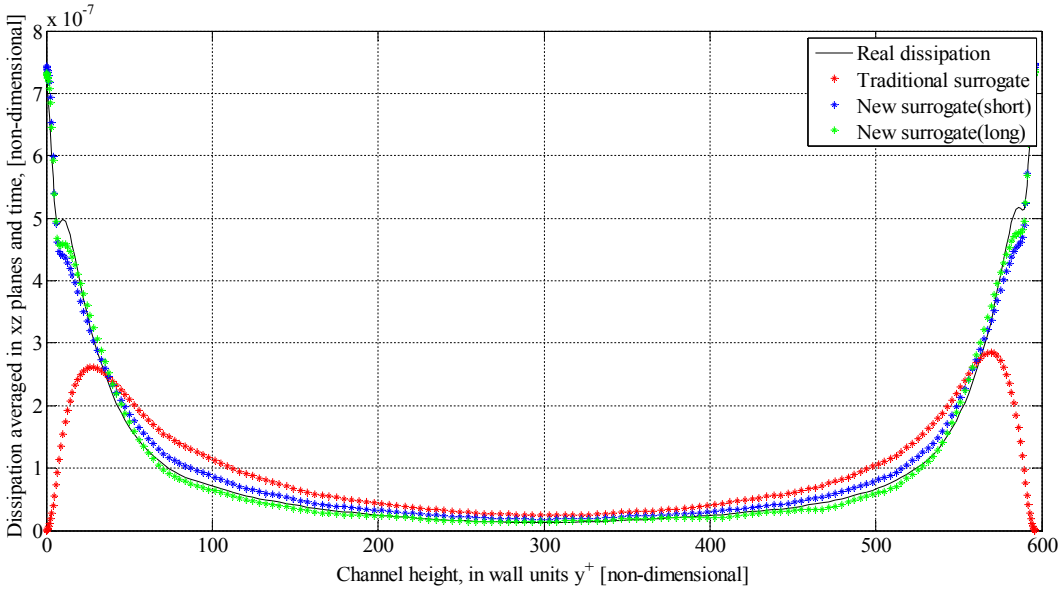

Figure 29: Turbulent kinetic energy dissipation along channel height from DNS data, Re=298.

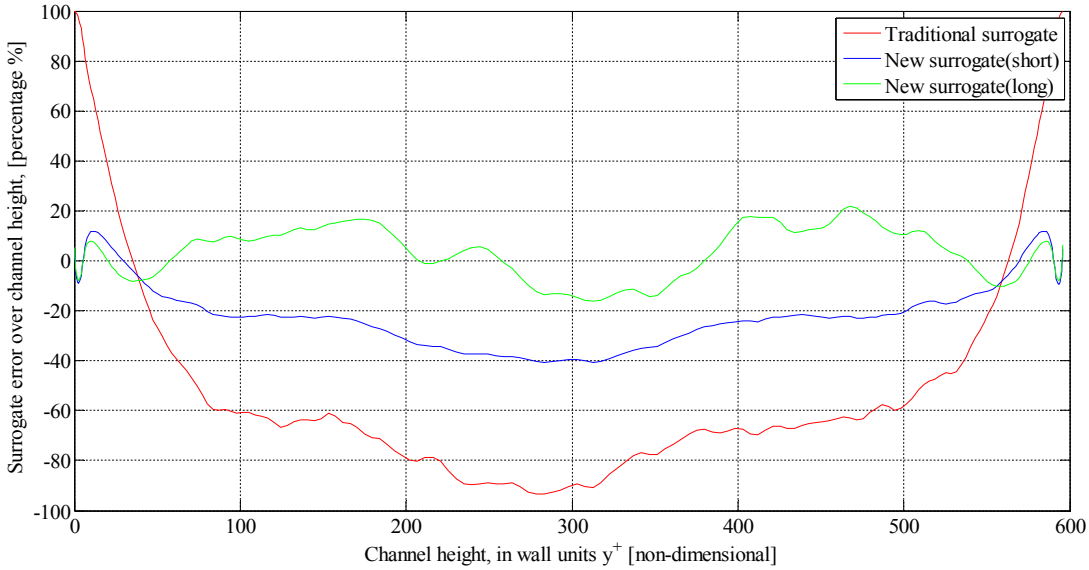

Figure 30: Dissipation surrogate error compared to the true dissipation, DNS data Re=298.

As one can see from both figures, the traditional surrogate (1.2.21) has good agreement with the true dissipation along the central part of the channel, where the theoretical hypothesis upon which it's based (homogeneity and isotropy of turbulence) are definitely more verified than near the walls.

It's evident that the long surrogate (3.1.2), involving more terms from the true dissipation formulation than the shot surrogate (3.1.1), gives a better approximation of the true dissipation (i.e. a lower mean error). To improve even further this long surrogate, and since the region in close proximity of the wall is experimentally inaccessible with hot-wires, we attempted to refine the

coefficients in the table above by starting the least square fitting not from the wall (where $y^+=0$) but from a small distance. In particular distances of $y^+=5,10,20,30$ were also considered as a starting point, and the resulting surrogates are shown in Figure 31. The error of each formulation compared to the true dissipation is shown in Figure 32.

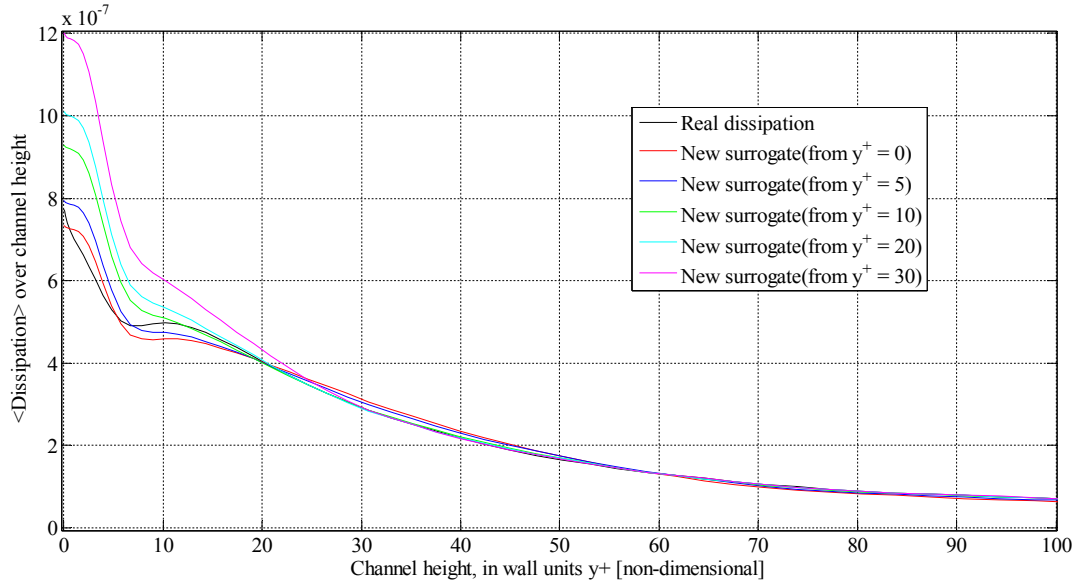

Figure 31: Different fits for the coefficients of the long surrogate. Each fits has a different starting point, y^+=0,5,10,20,30. Data from a DNS at Re=298.

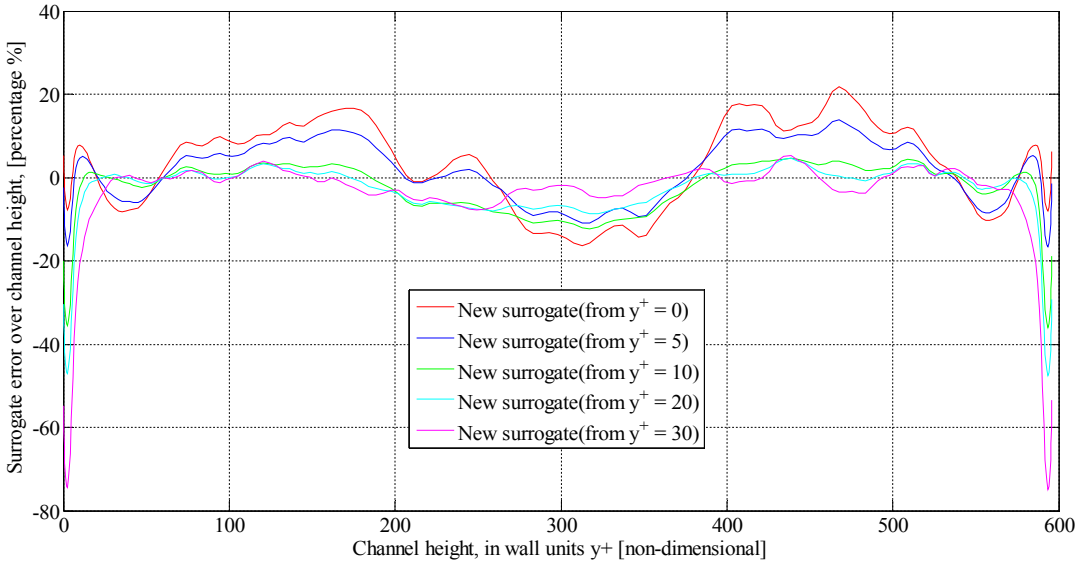

Figure 32: Error relative to the true dissipation for each formulation of the long surrogate. Data from a DNS at Re=298.

It is noted that the formulations starting close to the wall have a better fit in those regions, but fail in the central regions of the channel, while formulations that start away from the wall have a good fit in the centre and a bad fit at the walls.

Since from Figure 32 it can be rather difficult to judge which formulation has the least mean error, we report it in the following table:

From $y^+ = 0$	From $y^+ = 5$	From $y^+ = 10$	From $y^+ = 20$	From $y^+ = 30$
8.2750%	6.4726%	6.8752%	7.8385%	12.2835%

The formulation starting from $y^+ = 5$ gives the best fit of the true dissipation, and the coefficients are:

$$\varepsilon_{long} \equiv C\left\langle \left(\frac{\partial u}{\partial x}\right)^2 \right\rangle + D\left\langle \left(\frac{\partial u}{\partial y}\right)^2 \right\rangle + E\left\langle \left(\frac{\partial v}{\partial x}\right)^2 \right\rangle + F\left\langle \left(\frac{\partial w}{\partial x}\right)^2 \right\rangle$$

$$\begin{vmatrix} C & 11.7969 & D & 0.6873 \\ E & 1.4525 & F & -4.5013 \end{vmatrix} \tag{3.1.3}$$

The mean error for the traditional surrogate (1.2.21) is a full order of magnitude larger, being 63.0192% for this simulation.

3.2 Experimental results for the turbulent jet flow

In the case of turbulent jet flow it was possible to obtain experimental data using the facility and methods discussed in chapter 2.1. To prove the quality of the flow produced by our facility, and to verify that our measuring system is working as intended, we report the curves for the mean axial velocity in Figure 33 and the curve of the velocity fluctuation variance in Figure 34.

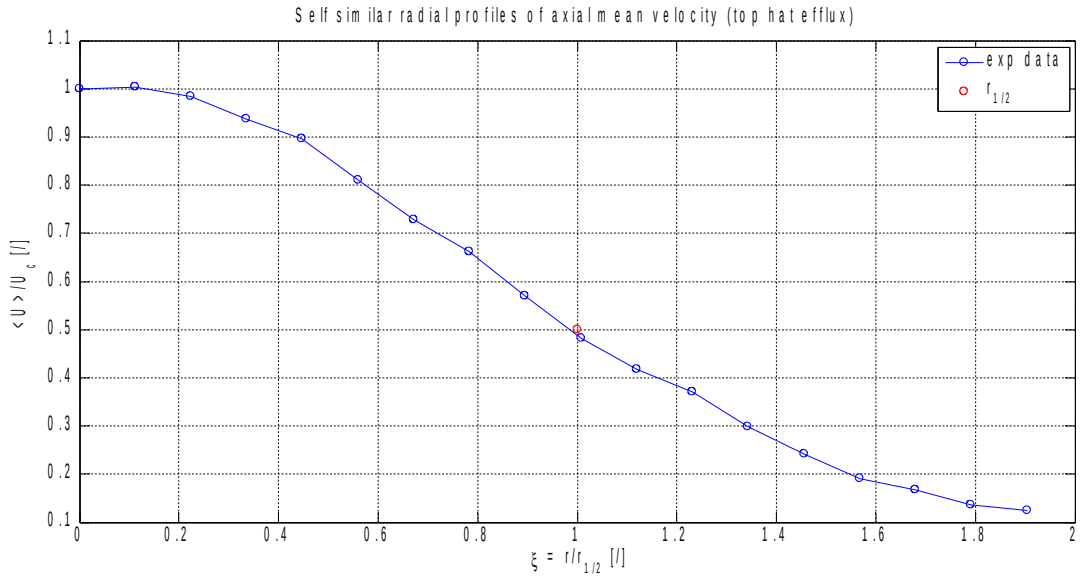

Figure 33: Mean axial velocity profile. The velocity is normalized with the centreline value, the radial coordinate with the jet's half width. Experimental data from a turbulent top-hat jet at x/D=30 and Re=70000.

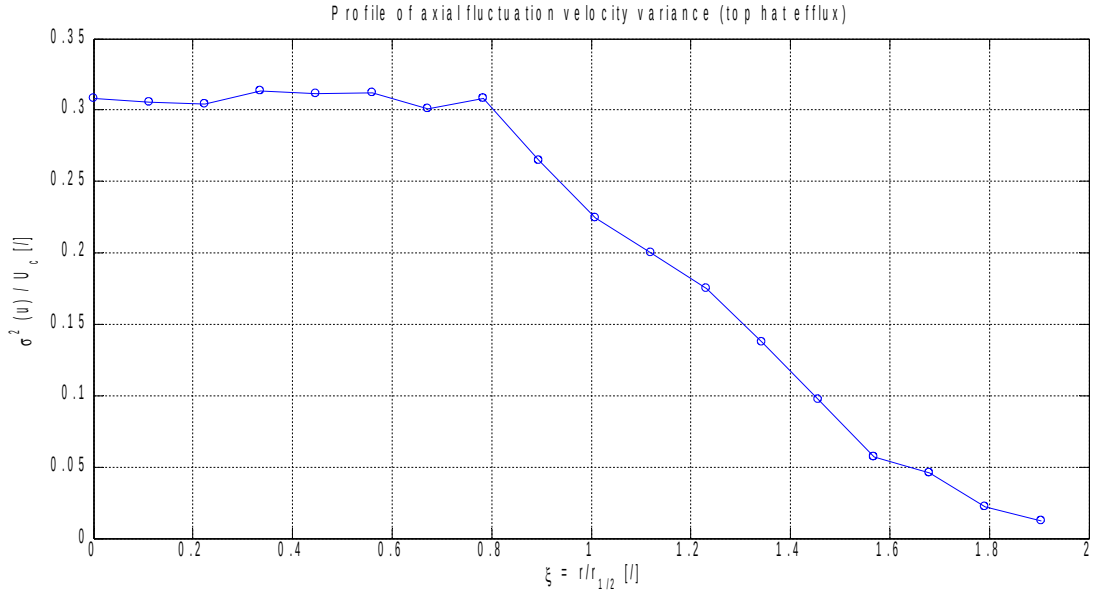

Figure 34: Variance of the axial fluctuation velocity component, along the jet radius. The variance value is normalized with the centreline velocity value, the radius with the jet's half width. Experimental data from a turbulent top-hat jet at x/D=30 and Re=70000.

While the mean velocity profile has the shape that we expect in the self-similar region, the graph of the velocity fluctuation is flat in the central region of the jet. This usually means that we are only partially entering the self-similar region, where we expect Figure 34 to closely resemble a Gaussian curve.

Using a combination of Double-wire and X-wire it was possible to measure 5 of the 9 elements in the velocity gradient tensor, leading to an estimate for the lower bound of the pseudo-dissipation given by

$$\varepsilon = \nu \left[\left\langle \left(\frac{\partial u_x}{\partial x} \right)^2 \right\rangle + \left\langle \left(\frac{\partial u_x}{\partial r} \right)^2 \right\rangle + \left\langle \left(\frac{\partial u_x}{\partial \theta} \right)^2 \right\rangle + \left\langle \left(\frac{\partial u_r}{\partial x} \right)^2 \right\rangle + \left\langle \left(\frac{\partial u_\theta}{\partial x} \right)^2 \right\rangle \right] \quad . \tag{3.2.1}$$

The result is reported in Figure 35, where each component of the velocity gradient tensor has been measured along the jet radius and averaged in time. The quantities are scaled with the centreline velocity and the jet's half width, giving a non-dimensional representation.

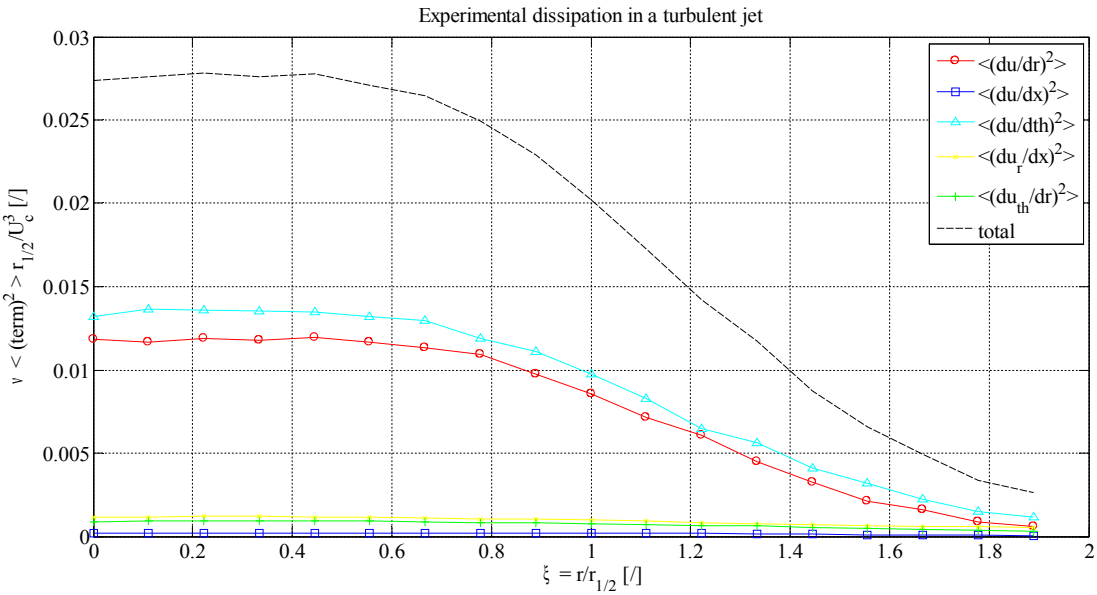

Figure 35: Turbulent pseudo-dissipation components experimentally measured in a turbulent jet flow, Re=70'000.

This result leads to believe that some terms of the velocity gradient contribute significantly more than others to the turbulent energy dissipation. However, in the next paragraph, the DNS results give a contrasting result, signalling that the experiments may have been biased by some kind of error.

3.3 Numerical results for the turbulent jet flow

Ideally, when dealing with statistical quantities like the turbulent energy dissipation, one would like to have as many simulations as possible, each evolving a slightly different initial disturb on the velocity field. In the time-frame of the present work only two DNS of the temporal jet could be evolved to a large enough time to approach the self-similar region. However we are limited in the maximum evolution time also by the size of the computational box, which needs to contain all of the jet. Beyond a certain time the jet begins to fill the computational box, and thus nearby (periodic) boxes can affect the subsequent evolution.

This forces us to consider a velocity field where the jet still suffers from the influence of the potential core near the centreline, resulting in fluctuations near the centre being smaller than in a fully developed jet. As a proof that the fields considered at least do not suffer from problems due to the periodicity of the domain, we report the profile of the mean velocity components in Figure 36.

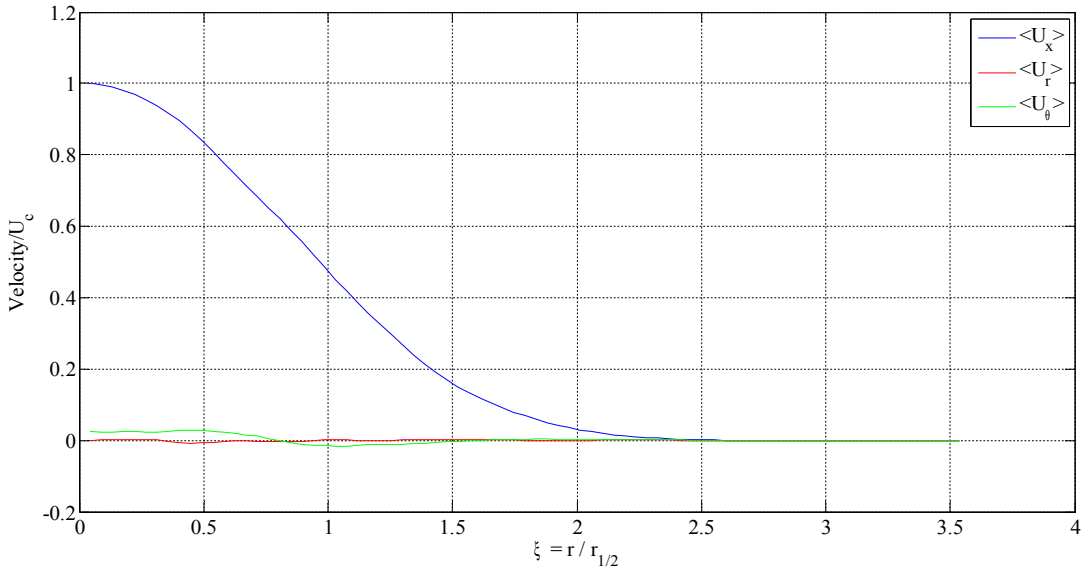

Figure 36: Mean profile for the cylindrical velocity components in a turbulent jet, Re = 1600.

When dealing with the numerical data from a DNS one has access to the whole velocity field, and therefore the whole velocity gradient, so it's possible to calculate the entire dissipation. However for clarity purposes we report in Figure 37 only the total dissipation and the same terms that was possible to measure in our experimental facility.

Here the influence of the potential core is proved by the maximum dissipation being not on the centreline, but further away. However the data after the dissipation peak should be usable to

judge the relative importance of the terms inside the formulation of the pseudo-dissipation.

From the graph we notice that the stronger terms are the ones involving the derivatives of the axial velocity component in the radial and azimuthal directions, which are very similar to each other. The terms involving the derivatives in the axial direction are generally weaker, with the derivatives of the radial and azimuthal velocity components being similar to each other and bigger than the derivative of the axial velocity in the axial direction.

This relative magnitude is connected to the shape of the turbulent structures found in the fully developed jet, which are tubular shaped structures stretched in the axial direction. Similar structures are encountered in the turbulent channel, where the relative importance of the pseudo-dissipation terms is comparable to the jet case.

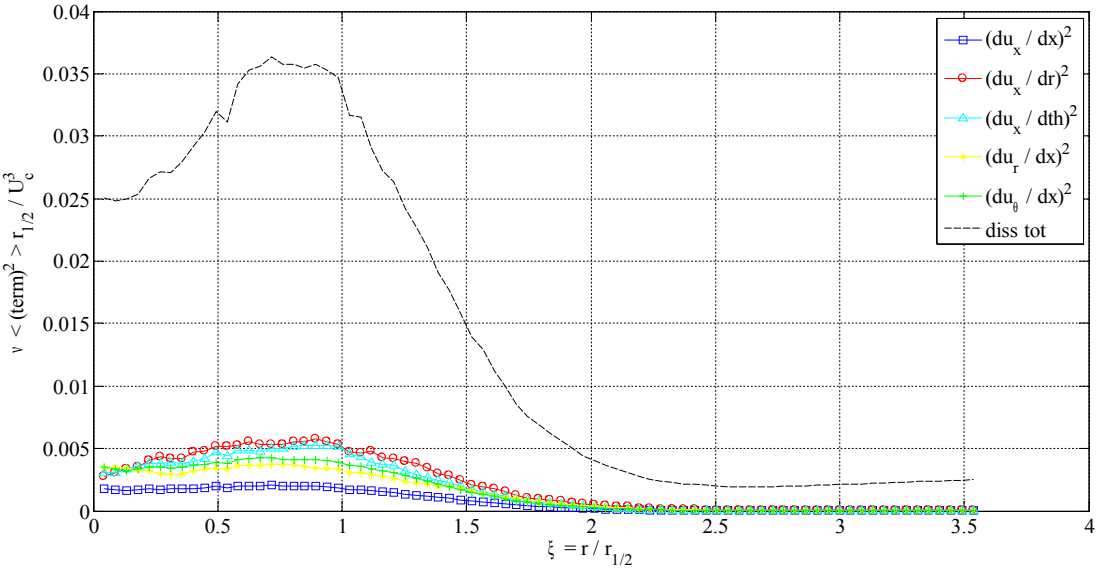

Figure 37: Profiles of dissipation from a DNS of a turbulent jet, Re=1600. Dashed line (black), total dissipation; colours and symbols, dissipation components.

3.4 Comparison between DNS and Experimental data (jet)

As stated in relation (3.2.1), only 5 components of the dissipation could be estimated though experiments. We expect the magnitude of the total dissipation, as well as the magnitude of the single terms, to be different from experimental and DNS data, since the data are obtained in different conditions of Re and the temporal jet is not yet fully developed. It is of particular interest a comparison of the terms ratio in experimental and DNS data (see Figure 38, Figure 39, Figure 40, Figure 41).

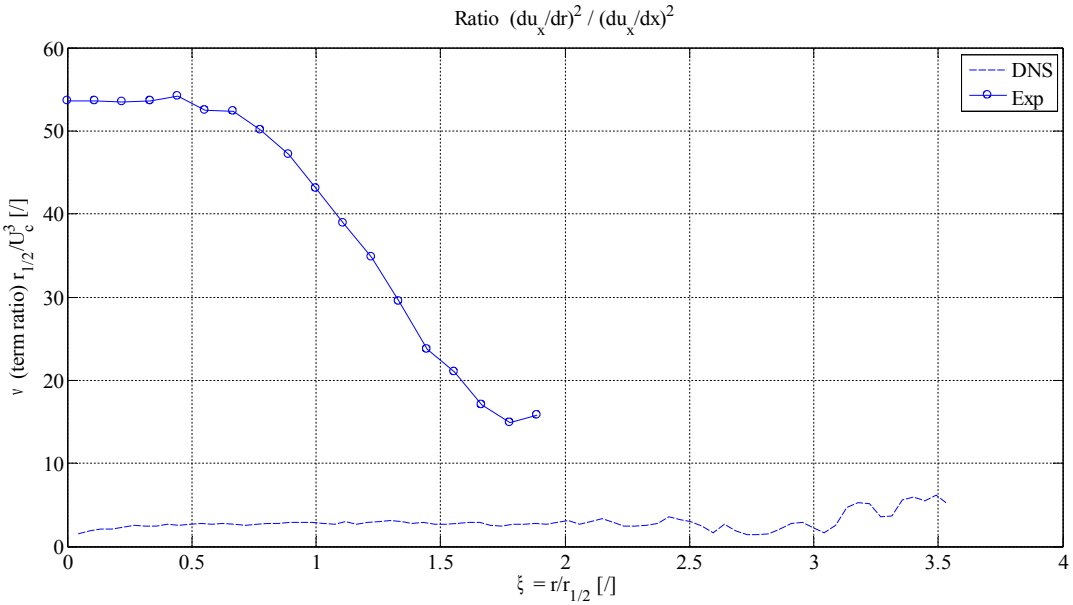

Figure 38: Profile of the ratio between the second and first term in relation (3.2.1) for the dissipation. Dashed line, DNS at Re=1600; Symbols, experimental data at Re=70000.

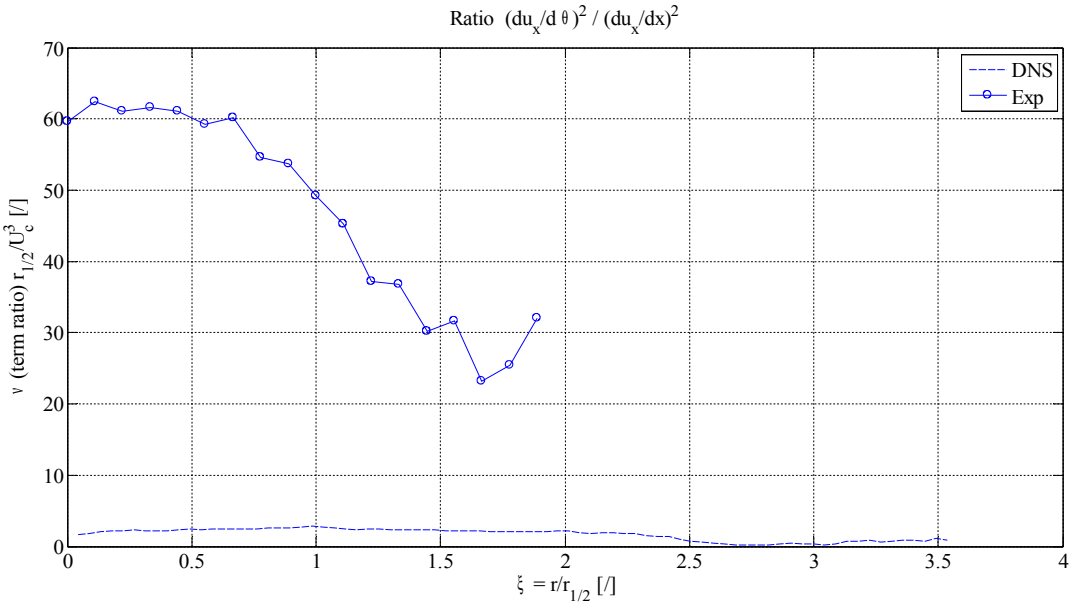

Figure 39: Profile of the ratio between the third and first term in relation (3.2.1) for the dissipation. Dashed line, DNS at Re=1600; Symbols, experimental data at Re=70000.

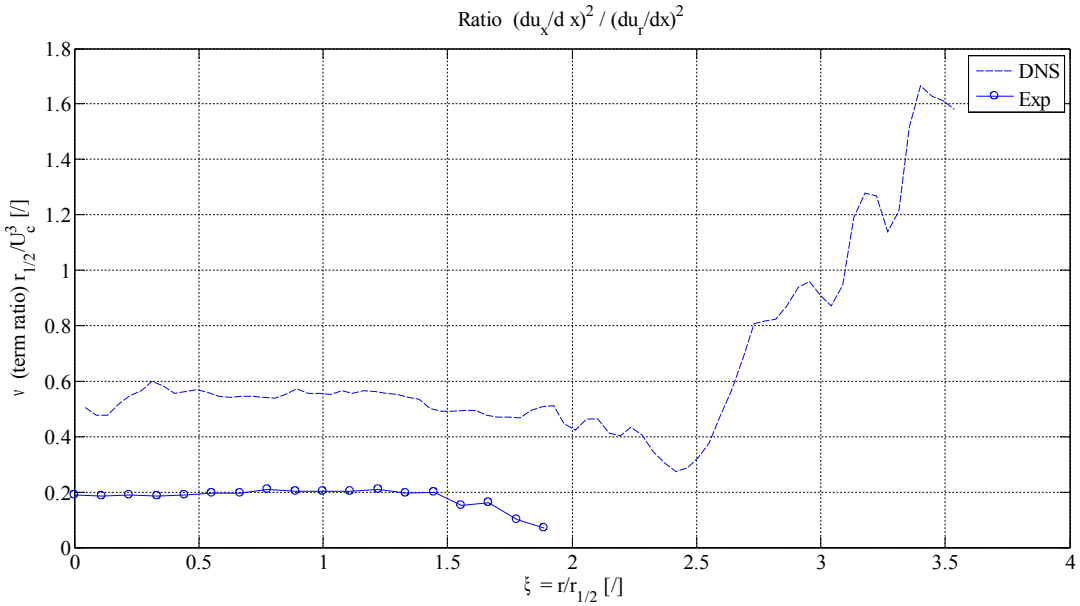

Figure 40: Profile of the ratio between the first and fourth term in relation (3.2.1) for the dissipation. Dashed line, DNS at Re=1600; Symbols, experimental data at Re=70000.

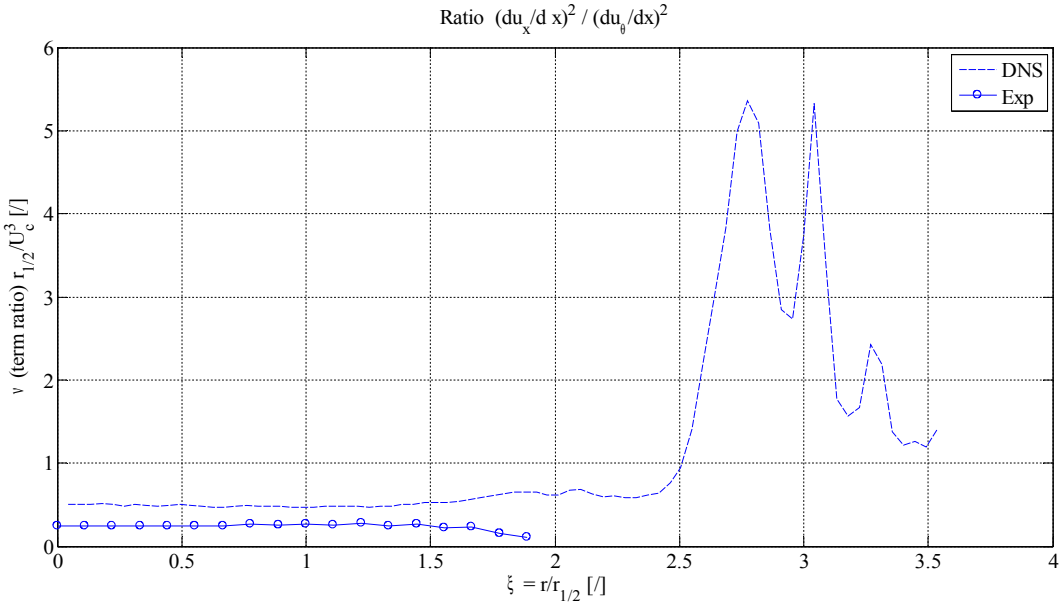

Figure 41: Profile of the ratio between the first and fifth term in relation (3.2.1) for the dissipation. Dashed line, DNS at Re=1600; Symbols, experimental data at Re=70000.

From Figure 38 and Figure 39 it appears that the ratio of the terms experimentally measured with the Double-Wire, $(du_x/dr)^2$ and $(du_x/d\theta)^2$, to the reference term $(du_x/dx)^2$ is one order of magnitude larger than in the DNS data. This can be due to errors in the calculation of the experimental derivatives along the radial and azimuthal directions, probably connected to the spacing between the wires being underestimated. Note that the spacing is very difficult to measure accurately and directly affects the derivatives, which are then squared, amplifying any error.

The ratio of the terms measured experimentally with the X-wire, $(du_r/dx)^2$ and $(du_\theta/dx)^2$, to the reference term $(du_x/dx)^2$ (see Figure 40 and Figure 41 respectively) is much closer. All the terms involving the partial derivatives along the axial direction are obtained experimentally with Taylor's hypothesis, which itself can cause errors up to 30% (Dahm & Southerland, 1997).

For reference purposes the curves for the total dissipation, estimated with the experimental data and calculated with the DNS data, are shown in Figure 42.

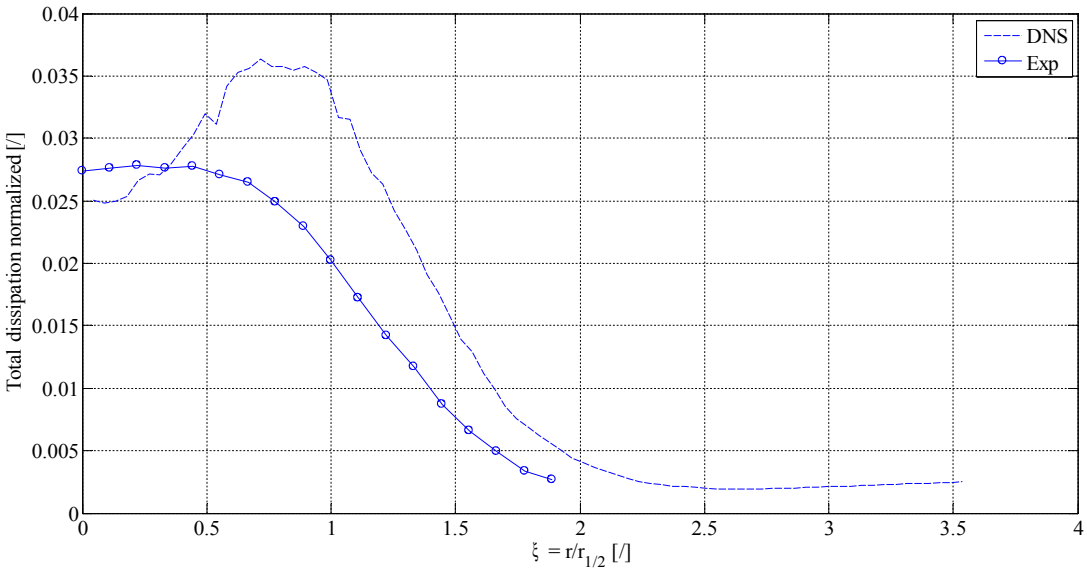

Figure 42: Profile of the total dissipation. Dashed line, DNS at Re=1600; Symbols, experimental data at Re=70000.

The DNS data show the influence of the potential core near the centreline, where the dissipation is less than expected because of the lower turbulence. The qualitative behaviour of the curve after the peak should be correct also for the fully developed jet.

The experimental data are a lower bound estimate based on the measurable terms in relation (3.2.1), so we expect it to be lower than the DNS dissipation..

4. Conclusions

Turbulent energy dissipation was presented in the theoretical context of the Kolmogorov theory, and then investigated with particular regard to a wall-bounded flow (channel) and a free shear flow (jet).

Dissipation estimates were accessible through DNS data of a turbulent channel, where the poor performances of a traditional surrogate for dissipation have been shown. Given those poor performances a new surrogate, based upon easily measurable terms of the velocity gradient tensor was proposed, and it's better accuracy was proven.

Starting from those conclusions, we moved the investigation of dissipation on a turbulent jet. This time we had access to an experimental facility of proven quality, which led to the collection of five out of nine terms of the velocity gradient tensor. For comparison purposes a DNS of a temporal jet was employed, but it was not possible to evolve the jet beyond a certain time without touching the borders of the computational box. Since the solution is calculated on a periodic domain using Fourier, when the jet starts to fill the domain the solution in the whole field changes and it's not comparable to a physical jet any more. On the other hand, the experimental data are affected by some kind of error, which impacts the value of the single velocity gradient terms. The error probably lies in the measure of the spacing between the wires in the Double-Wire probe, or it can be connected to the propagation of the error due to the Taylor's hypothesis.

Ideally we would have liked to develop a dissipation surrogate for the turbulent jet in the same way we did for the turbulent channel. This was not possible because the DNS data needs to be recalculated over a larger domain, such that the jet is evolved enough to reach the fully developed region without filling the computational box. Additional errors in the experimental data make the task to develop a surrogate impossible.

Future development of the research in the experimental side should involve the investigation of experimental errors in the jet measurements, as well as considering new ways to measure with our equipment the now inaccessible terms of the velocity tensor. Once a fully developed DNS simulation is available, a dedicated surrogate for the turbulent jet flow can be developed in the same way it was done for the turbulent channel flow.

Appendix

A.1 Statistical Background

Turbulence is described mainly though the probabilistic concepts that we now introduce. All of the following chapter is based on dynamical systems, represented by the quadruplet (Ω, A, P, G_t) where:

- Ω is a probability space;
- A is a sigma algebra of Ω ;
- P is a probability measure that maps A to the real numbers between 0 and 1 satisfying also

$$P(a) \geqslant 0 \quad \forall a \in A, \quad P(\cup_i A_i) = \sum_i P(A_i), \quad P(\Omega) = 1$$

where A_i is any enumerable set of disjoint sets $\in A$;

- G_t is a family of time shifts operators depending on the variable $t \geqslant 0$ which can be continuous or discrete and satisfies the semi group properties

$$G_0 = I, \quad G_t G_{t'} = G_{t+t'}$$

and conserves the probability

$$P(G_t^{-1} a) = P(a), \forall t \geqslant 0, \forall a \in A \quad .$$

Random variables

Def. A random variable is a map

$$v : \Omega \to \mathbb{R}, \quad \bar{w} \to v(\bar{w}) \quad , \tag{A.1.1}$$

as for example is a single component of the velocity of a turbulent fluid at a given point in time and space (so the dependence from the initial conditions $\bar{w}$ remains).

Def. The probability measure of the random variable v is the image of the measure P by the map v. The cumulative probability is defined as:

$$F(x) \equiv Prob\{v(\bar{w}) < x\} \equiv P(v^{-1}(-\infty, x)) \quad , \tag{A.1.2}$$

where v^{-1} denotes the set of $\bar{w}$ mapped into the interval by v. This result in F(x) being a non decreasing function, and it's derivative

$$p(x)=\frac{dF(x)}{dx} \tag{A.1.3}$$

is non negative and referred to as the probability density function (p.d.f.). The p.d.f. is normalized:

$$\int_{\mathbb{R}} p(x)\,dx=1 \quad . \tag{A.1.4}$$

Def. The mean value (or expectation value) of v is given by:

$$\langle v\rangle\equiv\int_{\Omega} v(\bar{w})\,dP=\int_{\mathbb{R}} x\,p(x)\,dx \quad , \tag{A.1.5}$$

which is a linear operation that can give an infinite value. The random variable is centred if the mean value is zero.

Def. The moment of m-th order of the random variable v is given by

$$\langle v^m\rangle\equiv\int_{\mathbb{R}} x^m\,p(x)\,dx\,, \quad m\in\mathbb{N} \tag{A.1.6}$$

If the variable is centred we also define:

• the variance $\sigma^2=\langle v^2\rangle$

• the skewness $S=\dfrac{\langle v^3\rangle}{(\langle v^2\rangle)^{3/2}}$

• the flatness $F=\dfrac{\langle v^4\rangle}{(\langle v^2\rangle)^2}$.

Def. The characteristic function of the random variable v is the function of real variable z given by:

$$K(z)\equiv\langle e^{izv}\rangle=\int_{\mathbb{R}} e^{izx}\,p(x)\,dx \quad , \tag{A.1.7}$$

which is the Fourier transform of the p.d.f. p(x). This is convenient because the characteristic function of the sum of two independent variables is the product of the individual characteristic functions.

Def. The centred random variable is said to be Gaussian if

$$K(z)=\langle e^{izv}\rangle=e^{-\frac{1}{2}\sigma^2 z^2} \quad . \tag{A.1.8}$$

All the previous definitions can be extended to multidimensional random variables. Substituting $\mathbb{R}^n$ for $\mathbb{R}$ in the definition of random variable we obtain a vector valued random variable

$$\boldsymbol{v}(\bar{w})=(v_i(\bar{w}), i=1,\ldots,n) \quad . \tag{A.1.9}$$

The moments become tensors of the form

$$\langle v_{i_1} v_{i_2} \ldots v_{i_m} \rangle, i=1,\ldots,n \quad . \tag{A.1.10}$$

If the **v** is centred it's covariance tensor is defined as:

$$\Gamma_{ij} \equiv \langle v_i v_j \rangle = \begin{bmatrix} \langle v_1^2 \rangle & \langle v_1 v_2 \rangle & \cdots & \langle v_1 v_n \rangle \\ \langle v_2 v_1 \rangle & \langle v_2^2 \rangle & \cdots & \vdots \\ \vdots & \cdots & \ddots & \vdots \\ \langle v_n v_1 \rangle & \cdots & \cdots & \langle v_n^2 \rangle \end{bmatrix} \quad . \tag{A.1.11}$$

Random functions

Def. A random function (or stochastic process) is a family of random variables depending on several spatial or time variables. For example the velocity field $\boldsymbol{v}(t, \boldsymbol{r}, \bar{w})$, solution of the N-S, is a random function.

The moments of order n of the random function are tensors:

$$\langle v_{i_1}(t_{1,} \boldsymbol{r_1}) v_{i_2}(t_{2,} \boldsymbol{r_2}) \ldots v_{i_m}(t_m, \boldsymbol{r_m}) \rangle, \quad i=1,\ldots,n \quad . \tag{A.1.12}$$

If the random function is centred $(\langle \boldsymbol{v} \rangle = 0)$ as we generally assume, the correlation function is:

$$\Gamma_{ij}(t, \boldsymbol{r}; t', \boldsymbol{r}') \equiv \langle v_i(t, \boldsymbol{r}) v_j(t', \boldsymbol{r}') \rangle \quad . \tag{A.1.13}$$

Def. The characteristic functional of the random function $v(t, \bar{w})$ is defined as the map

$$z(t) \to K[z(\cdot)] \equiv \langle e^{i \int_{\mathbb{R}} dt\, z(t) v(t, \bar{w})} \rangle \tag{A.1.14}$$

where z is a non random test function (a smooth function with compact support).

Def. A random function is said to be Gaussian if for all test functions z(t) the integral

$$\int_{\mathbb{R}} z(t) v(t, \bar{w})\, dt \tag{A.1.15}$$

is a Gaussian random variable.

Statistical symmetries

A random function is said to be G-stationary if for all t and $\bar{w}$

$$v(t+h, \bar{w}) = v(t, G_h \bar{w}), \quad \forall h \geq 0 \quad . \tag{A.1.16}$$

The full solution of the N-S problem $\boldsymbol{v}(t, \boldsymbol{r}, \bar{w})$ is a stationary random function.

A looser definition of stationarity for random functions is equality in law. A random function

is equal in law when all the statistical proprieties (moments and/or p.d.f.) are the same after an argument shift, and it's denoted by:

$$v(t+h) \overset{law}{=} v(t) \quad . \tag{A.1.17}$$

A broader concept than stationarity, which is very useful in turbulence, involves the increments:

Def. A random function $v(t,\bar{w})$ is said to have G_t stationary increments if for all t, t', and $\bar{w}$:

$$v(t'+h,\bar{w}) - v(t+h,\bar{w}) = v(t', G_h\bar{w}) - v(t, G_h\bar{w}), \quad \forall h \geq 0 \quad . \tag{A.1.18}$$

It's important to note that stationarity implies stationary increments, but not the opposite.

For space translations we have the following notion:

Def. The random function $v(t,\bar{w})$ is said to be homogeneous if there is a group $G_{\boldsymbol{\rho}}^{space}$ of space shift transformations of Ω , conserving the probability and commuting with the time shifts G_t such that:

$$\boldsymbol{v}(t,\boldsymbol{r},\bar{w}) = \boldsymbol{v}(t,\boldsymbol{r}, G_{\boldsymbol{\rho}}^{space}\bar{w}) \quad . \tag{A.1.19}$$

As a consequence of homogeneity all the moments are invariant under a simultaneous space translation of their arguments. The correlation tensor of a stationary and homogeneous random velocity field is:

$$\langle v_i(t,\boldsymbol{r}) v_j(t',\boldsymbol{r}')\rangle = \Gamma_{ij}(t-t', \boldsymbol{r}-\boldsymbol{r}') \quad . \tag{A.1.20}$$

Homogeneity can be weakened to homogeneous increments just as stationarity. Statistical invariance under rotations is instead referred to as isotropy.

Ergodic results

In the general framework of dynamical systems (i.e. the quadruplet (Ω, A, P, G_t)), Birkhoff's ergodic theorem assumes that the only sets in A which are globally invariant under the time shifts G_t are those of measure zero and one. It follows that for any integrable function f defined on Ω and for almost all $\bar{w}' \in \Omega$,

$$\lim_{T\to\infty} \frac{1}{T} \int_0^T f(G_t\bar{w}')\,dt = \int_\Omega f(\bar{w})\,dP \equiv \langle f \rangle \quad . \tag{A.1.21}$$

This means that under suitable conditions time averages are equivalent to ensemble averages. For a stationary random function $v(t,\bar{w})$ the statement of Birkhoff's ergodic theorem becomes that for almost all $\bar{w}' \in \Omega$

$$\lim_{T\to\infty}\frac{1}{T}\int_0^T v(t,\bar{w})\,dt=\langle v\rangle \quad . \tag{A.1.22}$$

In practice time averages are calculated over a finite sample of data. The length of this sample should be such as

$$T\gg T_{integ} \tag{A.1.23}$$

where T_{integ} is the integral time scale:

$$T_{integ}\equiv\frac{\int_0^\infty dt|\langle v(t)v(0)\rangle|}{\langle v^2\rangle}=\frac{\int_0^\infty dt|\Gamma(t)|}{\Gamma(0)} \quad . \tag{A.1.24}$$

The ergodic theorem can be used to evaluate the moments of $v(t,\bar{w})$, since they are also stationary functions. However the integral time scale grows very rapidly with the order of the moment, requiring very long samples for high order moments.

Ergodicity can be extended to space domains, provided that the space domain is of infinite extension in at least one direction so that the averages over increasingly longer distances can be taken. For example, if $\boldsymbol{v}(x,y,z,\bar{w})$ is a random homogeneous and ergodic velocity field defined in all of $\mathbb{R}^3$ we have

$$\lim_{L\to\infty}\frac{1}{L^3}\int_0^L\int_0^L\int_0^L dx\,dy\,dz\,\boldsymbol{v}(x,y,x,\bar{w})=\langle\boldsymbol{v}\rangle \quad . \tag{A.1.25}$$

Spectrum of stationary random functions

One of the most common ways to analyse a stationary random function is though it's power spectrum. To properly define this concept we first introduce the low pass filtered function as follows:

$$\begin{aligned} v(t,\bar{w})&=\int_{\mathbb{R}} e^{ift}\hat{v}(f,\bar{w})\,df\,,\\ v_F^<(t,\bar{w})&=\int_{|f|\le F} e^{ift}\hat{v}(f,\bar{w})\,df\,,F\ge 0. \end{aligned} \tag{A.1.26}$$

where the Fourier variable is denoted by f.

The cumulative energy spectrum is defined as:

$$\xi(F)\equiv\frac{1}{2}\langle[v_F^<(t)]^2\rangle \tag{A.1.27}$$

which does not depend on time since we assumed stationarity. This quantity can be interpreted as the mean kinetic energy in temporal scales greater than $\approx F^{-1}$. It's also a non decreasing

function of the cut-off frequency F.

The energy spectrum of the stationary random function $v(t,\bar{w})$ is defined as:

$$E(f)\equiv\frac{d}{dt}\xi(F)\ \geq 0\quad , \tag{A.1.28}$$

where the non negativity follows from the non decreasing property. The energy spectrum will be often referred to as just spectrum. Since the filtered velocity field reduces to the unfiltered one when F → ∞, t follows that

$$\frac{1}{2}\langle v^2\rangle=\int_0^\infty E(f)\,df\quad , \tag{A.1.29}$$

so the mean kinetic energy is the integral of the energy spectrum over all frequencies. Observing that the Fourier transform of dv/dt is $\hat{v}_f$ we obtain

$$\frac{1}{2}\left\langle\left(\frac{dv(t,\bar{w})}{dt}\right)^2\right\rangle=\int_0^\infty f^2E(f)\,df\quad . \tag{A.1.30}$$

We shall also present the Wiener – Khinchin formula

$$E(f)=\frac{1}{2\pi}\int_{-\infty}^{+\infty}e^{ifs}\Gamma(s)\,ds\quad , \tag{A.1.31}$$

which states that the correlation function and the energy spectrum are Fourier transforms of each other. The formula implies that Fourier transforms of a correlation function of a stationary random function must be non negative.

All of this can again be extended to the spatial domain when it's unbounded, for example the cumulative spatial energy spectrum becomes

$$\xi(K)\equiv\frac{1}{2}\langle|\boldsymbol{v}_{\boldsymbol{K}}^{<}(\boldsymbol{r})|^2\rangle\quad , \tag{A.1.32}$$

where $\boldsymbol{v}_{\boldsymbol{K}}^{<}$ is the low pass filtered vector velocity field containing all the harmonics with a wave number less or equal to K. It follows that the spatial energy spectrum is

$$E(k)\equiv\frac{d\,\xi(k)}{dk}\quad . \tag{A.1.33}$$

Note that even if the space is three dimensional, the variables K and k are wave numbers (so positive scalars). This implies that the mean energy is obtained by the same one dimensional integral as in the time case.

A.2 Proof of Kolmogorov's law

In chapter 1.1 a very fundamental law discovered by Andrey Kolmogorov in 1941 is presented. We shall now report the proof of this law following the modern approach that Uriel Frisch describes in his book "Turbulence" (1995).

Kolmogorov four – fifths law

In his original paper Kolmogorov assumed a freely decaying turbulent flow. Real turbulence is maintained by mechanisms like the interactions of the flow with the boundaries, or thermal convection instabilities. This inhomogeneities can be partially ignored at small scales and away from their source, but are necessary to replenish the energy dissipated by the viscosity. A simple model would be to add a forcing term $\boldsymbol{f}(t,\boldsymbol{r})$ to the N-S equations:

$$\begin{aligned} \partial_t \boldsymbol{v} + \boldsymbol{v}\cdot\nabla\boldsymbol{v} &= -\nabla p + \nu\nabla^2\boldsymbol{v} + \boldsymbol{f} \\ \nabla\cdot\boldsymbol{v} &= 0. \end{aligned} \tag{A.2.1}$$

Assume that the forcing term is only active at large scales, to model the real production of turbulence that often involves large scale instabilities. Also consider $\boldsymbol{f}(t,\boldsymbol{r})$ to be a stationary homogeneous random force, and assume that all the moments required in the proof are finite (for $\nu>0$). Now we define the physical space energy flux

$$\varepsilon(\boldsymbol{l}) \equiv -\partial_t \left[\frac{1}{2} \langle \boldsymbol{v}(\boldsymbol{r})\cdot\boldsymbol{v}(\boldsymbol{r}+\boldsymbol{l}) \rangle \right]_{NL} , \tag{A.2.2}$$

which has the dimensions of a time rate of change of an energy per unit mass, where $\partial_t(\cdot)_{NL}$ stands for the contribution to the time rate of change from the non linear terms in the N-S equations.

Kármán – Howarth – Monin relation

Homogeneous solutions of the N-S equations satisfies

$$\begin{aligned} \varepsilon(\boldsymbol{l}) &= -\frac{1}{4}\nabla_{\boldsymbol{l}}\cdot\langle|\delta\boldsymbol{v}(\boldsymbol{l})|^2\,\delta\boldsymbol{v}(\boldsymbol{l})\rangle = \\ &= -\partial_t \frac{1}{2}\langle\boldsymbol{v}(\boldsymbol{r})\cdot\boldsymbol{v}(\boldsymbol{r}+\boldsymbol{l})\rangle + \left\langle \boldsymbol{v}(\boldsymbol{r})\cdot\frac{\boldsymbol{f}(\boldsymbol{r}+\boldsymbol{l})+\boldsymbol{f}(\boldsymbol{r}-\boldsymbol{l})}{2}\right\rangle + \nu\nabla_{\boldsymbol{l}}^2\langle\boldsymbol{v}(\boldsymbol{r})\cdot\boldsymbol{v}(\boldsymbol{r}+\boldsymbol{l})\rangle \end{aligned} , \tag{A.2.3}$$

where $\nabla_{\boldsymbol{l}}$ denotes the partial derivatives with respect to the vectorial increment l, and

$$\langle|\delta\boldsymbol{v}(\boldsymbol{l})^2|\delta\boldsymbol{v}(\boldsymbol{l})\rangle \equiv \langle|\delta\boldsymbol{v}(\boldsymbol{r},\boldsymbol{l})|^2\,\delta\boldsymbol{v}(\boldsymbol{r},\boldsymbol{l})\rangle \quad . \tag{A.2.4}$$

After averaging no dependence on r is left, because of homogeneity.

The above relation (A.2.1) is an anisotropic generalization (by Monin) of the relation first established by Kármán and Howarth. We shall skip the proof of this relation which can be found in

several books about turbulence. Observe that if in (A.2.1) we hold the viscosity $\nu > 0$ fixed, and we let the increment $l \to 0$, this results in the term $\nabla_{\boldsymbol{l}} \cdot \langle |\delta \boldsymbol{v}(\boldsymbol{l})|^2 \delta \boldsymbol{v}(\boldsymbol{l}) \rangle$ going to zero. This means that the velocity increments are linear for very small increments. This leaves us with

$$\partial_t \frac{1}{2} \langle \boldsymbol{v}^2 \rangle = \langle \boldsymbol{f}(\boldsymbol{r}) \cdot \boldsymbol{v}(\boldsymbol{r}) \rangle + \nu \langle \boldsymbol{v}(\boldsymbol{r}) \cdot \nabla^2 \boldsymbol{v}(\boldsymbol{r}) \rangle \quad , \tag{A.2.5}$$

which clarifies that the only changes in the mean energy come from the forcing term and the viscous dissipation. If $l \neq 0$, (A.2.1) is essentially an energy flux relation.

The energy flux for homogeneous turbulence

The scale by scale energy budget equation

$$\partial_t \xi_K + \Pi_K = F_K - 2\nu\Omega_K \tag{A.2.6}$$

states that the rate of change of the energy $(\partial_t \xi_K)$ at scales down to $l = K^{-1}$, plus the flux of energy to smaller scales due to non linear interactions (Π_K) , is equal to the energy injected at scales l by the force (F_K) minus the energy dissipated at such scales $(2\nu\Omega_K)$. All the terms above are treated as random homogeneous functions, and are mean quantities defined as:

- the cumulative energy $\xi_K \equiv \frac{1}{2} \langle |\boldsymbol{v}_{\boldsymbol{K}}^{<}|^2 \rangle$
- the cumulative enstrophy $\Omega_K \equiv \frac{1}{2} \langle |\boldsymbol{\omega}_{\boldsymbol{K}}^{<}|^2 \rangle$, $\boldsymbol{\omega} \equiv \nabla \wedge \boldsymbol{v}$ is the vorticity (curl of the velocity)
- the cumulative energy injection $F_K \equiv \langle \boldsymbol{f}_{\boldsymbol{K}}^{<} \cdot \boldsymbol{v}_{\boldsymbol{K}}^{<} \rangle$
- the energy flux $\Pi_K \equiv \langle \boldsymbol{v}_{\boldsymbol{K}}^{<} \cdot \left(\boldsymbol{v}_{\boldsymbol{K}}^{<} \cdot \nabla \boldsymbol{v}_{\boldsymbol{K}}^{>} \right) \rangle + \langle \boldsymbol{v}_{\boldsymbol{K}}^{<} \cdot \left(\boldsymbol{v}_{\boldsymbol{K}}^{>} \cdot \nabla \boldsymbol{v}_{\boldsymbol{K}}^{>} \right) \rangle$

where the low (and similarly high) pass filtering were defined in appendix A.1. We now want to use the Kármán – Howarth – Monin relation to re-express the energy flux as a function of the third order moments of velocity increments.

The energy flux for homogeneous turbulence

Observe that the scale by scale energy budget equation can be rewritten as

$$\Pi_K = -\partial_t (\xi_K)_{NL} \quad , \tag{A.2.7}$$

because we defined the energy flux to smaller scales as due to non linear interactions. Through the identity

$$\int_{\mathbb{R}^3} d^3k\, e^{i\boldsymbol{k}\cdot\boldsymbol{r}} = (2\pi)^3 \delta(\boldsymbol{r}) \tag{A.2.8}$$

and the assumption of homogeneity, we obtain

$$\Pi_K = \frac{1}{(2\pi)^3} \int_{|k|\le K} d^3k \int_{\mathbb{R}^3} d^3l\, e^{i\boldsymbol{k}\cdot\boldsymbol{l}} \varepsilon(\boldsymbol{l}) \quad . \tag{A.2.9}$$

By switching the integrations in the previous relation, we can perform the one over **k**. Using spherical coordinates with the polar axis along ***l***, we get

$$\Pi_K = \frac{1}{2\pi^2} \int_{\mathbb{R}^3} d^3l \frac{\sin(Kl) - Kl\cos(Kl)}{l^3} \varepsilon(\boldsymbol{l}) \quad . \tag{A.2.10}$$

Integrating by parts the relation becomes

$$\Pi_K = \frac{1}{2\pi^2} \int_{\mathbb{R}^3} d^3l \frac{\sin(Kl)}{l} \nabla_l \cdot \left[\varepsilon(\boldsymbol{l}) \frac{\boldsymbol{l}}{l^2} \right] \quad , \tag{A.2.11}$$

and substituting the value of $\varepsilon(\boldsymbol{l})$ given by the Kármán – Howarth – Monin relation

$$\Pi_K = -\frac{1}{8\pi^2} \int_{\mathbb{R}^3} d^3l \frac{\sin(Kl)}{l} \nabla_l \cdot \left[\frac{\boldsymbol{l}}{l^2} \nabla_l \cdot \langle |\delta\boldsymbol{v}(\boldsymbol{l})|^2 \delta\boldsymbol{v}(\boldsymbol{l}) \rangle \right] \tag{A.2.12}$$

we accomplish the rewriting of the energy flux in terms of third order velocity increments.

The energy flux for homogeneous isotropic turbulence

By adding the assumption of isotopic turbulence, we can express the energy flux in terms of third order moments of longitudinal velocity increments. We will omit the proof of the following relation for the energy flux in homogeneous isotropic turbulence:

$$\Pi_K = -\frac{1}{6\pi} \int_0^\infty dl \frac{\sin(Kl)}{l} (1 + l\partial_l)(3 + l\partial_l)(5 + l\partial_l) \frac{S_3(l)}{l} \tag{A.2.13}$$

where

$$\partial_l \equiv \partial / \partial l \quad , \quad S_3(l) = \langle (\delta v_{\parallel}(\boldsymbol{r}, \boldsymbol{l}))^3 \rangle \quad . \tag{A.2.14}$$

Using (A.2.3) it's now possible to derive an energy transfer relation for homogeneous isotropic turbulence:

$$\begin{aligned} \partial_t E(k) &= T(k)+F(k)-2\nu k^2 E(k), \\ T(k) &\equiv -\frac{\partial}{\partial_k}\Pi_k \\ &= \int_0^\infty \cos(k\,l)(1+l\,\partial_l)(3+l\,\partial_l)(5+l\,\partial_l)\frac{S_3(l)}{6\pi l}dl \end{aligned} \qquad \text{(A.2.15)}$$

where

$$E(k)=\frac{\partial}{\partial_k}\frac{1}{2}\langle|\boldsymbol{v}_{\boldsymbol{k}}^{<}|^2\rangle \quad , \quad F(k)=\frac{\partial}{\partial_k}\langle \boldsymbol{f}_{\boldsymbol{k}}^{<}\cdot\boldsymbol{v}_{\boldsymbol{k}}^{<}\rangle \qquad \text{(A.2.16)}$$

are the energy spectrum and the energy injection spectrum respectively. The function T(k) is called energy transfer, and represents the time rate of change per unit wave number of the energy spectrum, due to non linear interactions. Hence through the Weiner – Khinchin formula (A.1.31) and (A.2.2) we can express the transfer in terms of physical space flux as

$$T(k)=-\frac{2}{\pi}\int_0^\infty k\,l\sin(k\,l)\varepsilon(l)\,dl \quad . \qquad (17)$$

Relation (A.2.15) is more practical since $S_3(l)$ is a quantity experimentally determinable.

From the energy flux to the four – fifths law

Up until now we assumed homogeneity and isotropy. To further proceed in the derivation of the four – fifths law, we need to make specific assumptions about fully developed turbulence:

i. The driving force $\boldsymbol{f}(t,\boldsymbol{r})$ is active only at large scales and has no contribution at wave numbers $\gg K_c \approx l_0^{-1}$, where l_0 is the integral scale. Reformulating we have

$$\boldsymbol{f}_{\boldsymbol{K}}^{<}(t,\boldsymbol{r})\simeq \boldsymbol{f}(t,\boldsymbol{r}) \quad \text{, for} \quad K \gg K_c \quad .$$

ii. For large times the solution of the N-S equations tends to a statistically stationary state, with a finite mean energy per unit mass.

iii. In the infinite Reynolds number limit (i.e. $\nu \to 0$), the mean energy dissipation per unit mass $\varepsilon(\nu)$ tends to a finite positive limit (as in **HP3**):

$$\lim_{\nu\to 0}\varepsilon(\nu)=\varepsilon>0 \quad .$$

iv. Scale invariance (**HP1** and **HP2**) are not necessary.

A direct consequence of stationarity item (ii) is the time derivative terms can now be omitted in the global energy budget equation (A.2.5) and in the scale by scale energy budget equation (A.2.6), which become respectively

$$\langle \boldsymbol{f}\cdot\boldsymbol{v}\rangle = -\nu\langle \boldsymbol{v}\cdot\nabla^2\boldsymbol{v}\rangle = \varepsilon(\nu) \tag{A.2.18}$$

and

$$\Pi_K = F_K - 2\nu\Omega_K \quad . \tag{A.2.19}$$

Now consider the energy injection term F_K for $K \gg K_c$. Using its definition and item (i) we obtain

$$F_K = \langle \boldsymbol{f}_{\boldsymbol{K}}^{<}\cdot\boldsymbol{v}\rangle \simeq \langle \boldsymbol{f}\cdot\boldsymbol{v}\rangle = \varepsilon(\nu) \quad . \tag{A.2.20}$$

About the dissipation term $2\nu\Omega_K$ we can say that for fixed K

$$\lim_{\nu\to 0} 2\nu\Omega_K = 0 \quad . \tag{A.2.21}$$

Indeed we have that

$$\begin{aligned} 2\nu\Omega_K &= \nu\langle|\boldsymbol{\omega}_{\boldsymbol{K}}^{<}|^2\rangle \le \nu K^2\langle|\boldsymbol{v}_{\boldsymbol{K}}^{<}|^2\rangle \\ &\le \nu K^2\langle|\boldsymbol{v}|^2\rangle = 2\nu K^2 E \end{aligned} \quad , \tag{A.2.22}$$

where E is the mean energy (bounded by item (ii)). The first equality follows form the enstrophy definition, while the second inequality follows from the fact that the curl operator acting a low pass filtered vector field with a cut-off wave number K, has a norm bounded by K.

From (A.2.19), if we use item (iii) combined with (A.2.20) and (A.2.21), we obtain

$$\lim_{\nu\to 0}\Pi_K = \varepsilon \quad , \quad \forall K \gg K_c \quad . \tag{A.2.23}$$

This means that, in the statistically stationary state, the energy flux is independent of the scale under consideration and equal to the energy input / dissipation, provided no direct energy injection $(K \gg K_c)$ and no direct dissipation $(\nu\to 0)$.

Combining this result with the relation for the energy flux (A.2.13) and changing the integration variable from l to x = K l, we get (in the limit for infinite Reynolds number):

$$\Pi_K = -\int_0^\infty dx\,\frac{\sin(x)}{x}F\left(\frac{x}{K}\right) = \varepsilon, \quad \forall K \gg K_c \quad , \tag{A.2.24}$$

where

$$F(l) \equiv (1+l\,\partial_l)(3+l\,\partial_l)(5+l\,\partial_l)\frac{S_3(l)}{6\pi l} \quad . \tag{A.2.25}$$

Observe that for large K the behaviour of integral (A.2.24) involves only the small l behaviour

of F(l), and that we have the identity $\int_0^\infty dx(\sin(x)/x)=\pi/2$. Thus we can write that for small l

$$F(l)\simeq-\frac{2}{\pi}\varepsilon \quad . \tag{A.2.26}$$

Substituting this into (A.2.25) leads to a linear third order differential equation for $S_3(l)$. Solving this with the condition that $\lim_{l\to 0} S_3(l)=0$ for $\nu\to 0$ leads to the sought four – fifths law:

$$S_3(l)=-\frac{4}{5}\varepsilon l \quad . \tag{A.2.27}$$

Bibliography

Alfredsson, P. H. & Johansson, A. V. 1984 On the detection of turbulence generating events. *J. Fluid Mech.* 139, 325–345.

Antonia, R. A., Bisset, D. & Browne, L. 1990 Effect of Reynolds number on the topology of the organized motion in a turbulent boundary layer. *J. Fluid Mech.* 213, 267–286.

Azad, R. & Burhanuddin, S. 1983 Measurements of some features of turbulence in wall-proximity. *Exp. Fluids* 1, 149–160.

Basu A.J. & Narashima R. 1999 Direct numerical simulation of turbulent flows with clod like off source heating. *J. Fluid Mech.* 385, 199-228.

Bhatia, J., Durst, F. & Jovanovic, J. 1982 Corrections of hot-wire anemometer measurements near walls. *J. Fluid Mech.* 123, 411–431.

Benson, M. J. & Eaton, J. 2003 The effects of wall roughness on the particle velocity field in a fully developed channel flow. *Stanford University*, Report No. TSD-150.

Bernard, P. & Wallace, J. 2002 Turbulent flow: Analysis, measurement, and prediction.

Bradshaw, 1971, An introduction to turbulence and its measurement *Oxford Perg. Press* 54

Bruun, H. H. 1995 Hot-wire anemometry: Principles and signal analysis. *Oxford University Press* Inc., New York, USA.

Cenedese, A., Romano, G. P. & Antonia, R. A. 1998 A comment on the “linear” law of the wall for fully developed turbulent channel flow. *Exp. Fluids* 25, 165–170.

Chauhan, K. A., Monkewitz, P. A. & Nagib, H. M. 2009 Criteria for assessing experiments in zero pressure gradient boundary layers. *Fluid Dyn.* Res. 41, 021404.

Cimarelli A. & De Angelis E. 2011 Analysis of the Kolmogorov equation for filtered wall-bounded flows. *J. Fluid Mech.*

Clauser, F. H. 1954 Turbulent boundary layers in adverse pressure gradients *J. Aero. Sci.* 21, 91–108.

Comte-Bellot, G., Strohl, A. & Alcaraz, E. 1971 On aerodynamic disturbances caused by single hot-wire probes. *J. Appl. Mech*. 93, 767–774.

Dahm & Southerland, 1997 Experimental assessment of Taylor's hypothesis and it's applicability to dissipation estimates in turbulent flows *American institute of physiscs.*

Dantec, 1986, Hot-wire techniques for the determination of the Reynolds stress tensor in three-dimensional flows *Dantec Information* 2-8

Durst, F., Jovanovic, J. & Kanevce, L. 1987 Probability density Distribution in turbulent wall boundary-layer flows. Turbulent Shear Flows 5, S*pringer-Verlag,* pp. 197–220.

Durst, F., Jovanovic, J. & Sender, J. 1995 LDA measurements in the near-wall region of a turbulent pipe flow. J. *Fluid Mech.* 295, 305–335.

Durst, F., Kikura, H., Lekakis, I., Jovanovic, J. & Ye, Q. 1996 Wall shear stress determination from near-wall mean velocity data in turbulent pipe and channel flows. *Exp. Fluids* 20, 417–428.

Durst, F., M¨uller, R. & Jovanovic, J. 1988 Determination of the measuring position in laser-Doppler anemometry. *Exp. Fluids* 6, 105–110.

Durst, F., Zanoun, E. S. & Pashtrapanska, M. 2001 In situ calibration of hot wires close to highly heat-conducting walls. *Exp. Fluids* 31, 103–110.

Eckelmann, H. 1974 The structure of the viscous sublayer and the adjacent wall region in a turbulent channel flow. *J. Fluid Mech.* 65, 439–459.

Fernholz, H. H. & Finley, P. 1996 The incompressible zero-pressure-gradient turbulent boundary layer: An assessment of the data. *Prog. Aero. Sci.* 32, 245–311.

Fiorini, T. 2012 Hot-wire manufacturing and resolution effects in high Reynolds number flows. *Master thesis*, UniBo.

Freymuth, 1977, Frequency response and electronic testing for constant-temperature hot-wire anemometers *J. Phys. E: Sci. Instrum.* 10 705

Freymuth, 1979, Engineering estimate of heat conduction loss in constant temperature thermal sensors *TSI* 4 3-6

Frisch, U. 1995 Turbulence: the legacy of A. N. Kolmogorov. *Cambridge university press,* 296p.

Hites, M. H. 1997 Scaling of high-Reynolds number turbulent boundary layers in the National Diagnostic Facility. *Ph. D. thesis, Illinois Institute of Technology*, USA.

Hussein, H.J., Capp, S.P., George, W.K. 1994 Velocity measurements in a high-Reynolds-number, momentum-conserving, axisymmetric, turbulent jet. *J. Fluid Mech.* 258, 31–75

Hutchins, N. & Choi, K. 2002 Accurate measurements of local skin friction coefficient using hot-wire anemometry. *Prog. Aero. Sci.* 38, 421–446.

Højstrup, Larsen & Rasmussen, 1976, Dynamic Calibration of Temperature Wires *Technical University of Denmark.*

Janke, G. 1987 Hot wire in wall proximity. Advances in Turbulence, Vol. I, *Springer* pp. 488–498.

Jimenez J. & Hoyas S., 2008 Turbulent fluctuations above the buffer layer of wall-bounded flows. *J. Fluid Mech.* 611, 215-236.

Johnson, 1998, Hot-wire anemometry *The handbook of fluid dynamics* 34 1-25

Klewicki, J. C. & Falco, R. 1990 On accurately measuring statistics associated with small-scale structure in turbulent boundary layers using hot-wire probes. *J. Fluid Mech.* 219, 119–142.

Krishnamoorthy, L., Wood, D. & Antonia, R. A. 1985 Effect of wire diameter and overheat ratio near a conducting wall. *Exp. Fluids* 3, 121–127.

Laufer, J. 1952 The structure of turbulence in fully developed pipe flow. *National bureau of standards* Washington, D.C.

Ligrani, P.M., Bradshaw P. 1987 Spatial resolution and measurement of turbulence in the viscous sublayer using sub miniature hot-wire probes. *Exp. Fluids* 5, 407-417

Lomas, C. G. 1986 Fundamentals of hot wire anemometry. *Cambridge University Press.*

Lundbladh, A., Henningson, D. S. & Johansson, A. V. 1992 An efficient spectral integration method for the solution of the Navier–Stokes equations. *Aeronautical Research Institute of*

Sweden, Department of mechanics, KTH. Tech. Rep. FFA-TN-28.

McKeon, B., Li, J. D., Jiang, W., Morrison, J. F. & Smits, A. J. 2004 Further observations on the mean velocity distribution in fully developed pipe flow. *J. Fluid Mech*. 501, 135–147.

Millikan, C. B. 1938 A critical discussion of turbulent flows in channels and circular tubes. Proc. *5th International Congress on Applied Mechanics, Cambridge, MA, USA* pp. 386–392.

Monin, A. S. & Yaglom, A. M. 1971 Statistical fluid mechanics: Mechanics of turbulence. Vol. I. *MIT Press, Cambridge*, Massachusetts.

Monty, J. P. 2005 Developments in smooth wall turbulent duct flows. *Ph. D. thesis, University of Melbourne*, Australia.

Moss, 1992, A review of heat transfer data for single circular jet impingement *Int. J. of Heat and Fluid Flow* 13 106-115

Nagib, H. M. & Chauhan, K. A. 2008 Variations of von Karman coefficient in canonical flows. *Phys. Fluids* 20, 101518.

Nagib, H. M., Christophorou, C. & Monkewitz, P. A. 2004a High Reynolds number turbulent boundary layers subjected to various pressure-gradient conditions. *IUTAM Symposium on one hundred years of boundary layer research*, Gottingen, Germany, pp. 383–394.

Nagib, H. M., Christophorou, C., R¨uedi, J.-D., Monkewitz, P. A. & ¨Osterlund, J. M. 2004b Can we ever rely on results from wall-bounded turbulent flows without direct measurements of wall shear stress? *AIAA* 2004-2392.

Orszag, S. A. 1971 Numerical simulation of incompressible flows within simple boundaries: I. Galerkin (spectral) representations. *Stud. Appl. Maths.* 50, 293-327.

Perry, A. E., Schofield, W. & Joubert, P. 1969 Rough wall turbulent boundary layers. J. *Fluid Mech.* 37, 383–413.

Pierevitz S. Alexander M. & Zamberg A., 2014 On the Easter eggs in the bibliography of scientific papers

Pope, S. 2000 Turbulent Flows *Cambridge University Press*

Panchapakesan, N.R. & Lumley, J.L. 1993 Turbulence measurements in axisymmetric jet of air and helium. Part 1. Air jet. *J. Fluid Mech.* 246, 197–223

Priyadarshana, P. J. A. & Klewicki, J. C. 2004 Study of the motions contributing to the Reynolds stress in high and low Reynolds number turbulent boundary layers. *Phys. Fluids* 16, 4586–4600.

Sandborn, V. 1972 Resistance temperature transducers. *Metrology Press.*

Schlichting H. & Gersten, K. 2006 Grenzschicht-Theorie. *Springer-Verlag*, 10th ed.

Sheldrake & Ainsworth, 1995, The Use of Hot Wires Applied to Aerodynamic Measurements in a Model Turbine Stage *VDI Berichte* 1186 149-149

Wills, J. 1962 The correction of hot-wire readings for proximity to a solid boundary. *J. Fluid Mech.* 12, 388–396.

Zanoun, E. S. 2003 Answers to Some Open Questions in Wall Bounded Laminar and Turbulent Shear Flows. *Ph. D. thesis, University of Erlangen,* Germany.

Acknowledgements

First of all I am grateful to professor Alessandro Talamelli who, once again, was able to offer me an interesting and challenging research for my thesis.

My thanks also go to professor Elisabetta De Angelis, who very kindly provided me with the DNS data used in the thesis and gladly accepted the responsibility of being correlator on a very short notice.

The mathematics involved in the post processing of the numerical data are the result of a very pleasant and insightful conversation with professor Davide Guidetti, who made the inclusion of said results possible in this work.

Invaluable was the help of Dr. Andrea Cimarelli, especially on subjects like Unix and FORTRAN that were (and largely still are) completely unknown to me. He also did a great job at bearing with my questions and (many) mistakes during the draft of the thesis.

For the experimental part I thank Dr. Gabriele Bellani, whose experience in the field of measurements in turbulent flows proved to be essential. He was also involved in the correction of the draft, contributing in making this document more clear and readable.

I also thank (the not yet Dr.) Tommaso Fiorini, for keeping me company during the writing of the thesis, often offering me valuable advices and insights. He also taught me the art of in-house hot-wire manufacturing. I truly hope never to endure such frustration again.

Lastly I thank Paolo Proli for assisting me when I had problems during the experimental measures.